

ELECTRIC FIELD CONTROL OF INTERFACIAL SPINS IN
FERROELECTRIC/FERROMAGNETIC JUNCTIONS

by

CANHAN SEN

Submitted to the Graduate School of Engineering and Natural Sciences
in partial fulfilment of the requirements for the degree of
Doctor of Philosophy

Sabanci University

July 2018

© Copyright by Canhan Sen, 2018

ELECTRIC FIELD CONTROL OF INTERFACIAL SPINS IN FERROELECTRIC/FERROMAGNETIC INTERFACE

Canhan Sen

Philosophy of Doctorate

Materials Science and Nanoengineering
Sabanci University

Thesis Supervisor: Doc. Dr. I. Burc Misirlioglu

2018

Keywords: Ferroelectrics, Ferromagnets, Tunnelling Magnetoresistance (TMR), Spin-dependent screening, Electrostatics,

Abstract

Electric field control of magnetization allows further miniaturization of integrated circuits for binary bit processing and data storage as it eliminates the need for bulky sophisticated systems to induce magnetic fields. Magnetoelectric coupling inherent to the bulk of multiferroic films or control of spin orientation in magnetic layers via piezoelectric strain in dual component composites have been two approaches standing out. Another magnetoelectric effect is spin-dependent screening that occurs at dielectric/ferromagnet interfaces which is of great importance for spin selective tunnel junctions. Here, we analyze the spin-dependent screening of ferroelectric polarization in a film interfacing ferromagnetic electrodes using the continuity equations in continuum media. The competition between the electrostatic and the magnetochemical potential in the FM electrodes gives rise to a reduction in the net magnetic moment near the interface due to spin mixing, extending to a distance comparable to the Thomas-Fermi screening length. Our continuum media treatment shows that the local spin population in spin subbands near the interfaces can dramatically deviate from bulk, which is in qualitative agreement with recent first principles results. We compute the tunneling currents for majority and minority spins using the Wentzel-Kramers-Brillouin approximation as a function of ferroelectric polarization. We find that the spin polarization tends to disappear for increasing values of ferroelectric polarization in direct connection with the increase in subband spin population for minority spins at the interface.

FERROELEKTRİK/FERROMANYETİK ARAYÜZEYLERDE ARAYÜZEY SPİNLERİNİN ELEKTRİK ALAN İLE KONTROLÜ

Canhan Sen

MAT, Doktora Tezi, 2018

Tez Danışmanı: Doç. Dr. I. Burç Mısırlıoğlu

Anahtar Kelimeler: Ferroelektrikler, Ferromagnetler, Tünelleme magnetodirenç (TMD), Spin-bağımlı perdeleme, Elektrostatik

Özet

Manyetizasyonun elektrik alan ile kontrolü; veri işleme ve depolamada kullanılmakta olan manyetik alan indükleyen büyük ve karmaşık sistemlerin yerine daha küçük boyutlu entegre devrelerin kullanılmasına imkan sağlamaktadır. Multiferroik filmlerin doğasın bulunan magnetoelektrik eşleşme ve iki bileşenli kompozitlerde gözlemlenen manyetik tabakaların piezoelektrik gerinme kaynaklı spin yöneliminin kontrolü; iki ana yöntem olarak öne çıkmaktadır. Başka bir manyetoelektrik etki ise spin tercihli tünel jonksiyonları için önem taşımakta olan dielektrik/ferromanyetik arayüzeyler arasında meydana gelen spin bağımlı perdelemedir. Bu çalışmada,ferroelektrik polarizasyonun ferromanyetik elektrotlarla biraraya getirilmiş olma ferroelektrik ince filmin polarizasyonunun süreklilik denklemleri ile sürekli bir ortamda spin bağımlı perdeleme etkisi analiz edilmiştir. Ferromanyetik elektrotlarda elektrostatik ve magnetokimyasal potansiyel arasındaki rekabet; Thomas-Fermi perdeleme mesafesi bağılı olarak arayüzeyde net manyetik momentin düşüşüne sebep olmaktadır. Sürekli ortam yaklaşımı arayüzey yakınlarındaki spin alt bantlarında lokal spin dağılımının katı haldeki özelliklerinden dikkate değer şekilde düşüş göstermektedir. Elde edilen sonuçlar, ilk-prensip yaklaşımı ile yapılan çalışmalarla da uyum göstermektedir. Çoğunluk ve azınlık spinler tünelleme akımları, ferroelektrik polarizasyonun bir fonksiyonu olarak Wentzel-Kramers-Brillouin yaklaşımı ile hesaplanmıştır. Artan ferroelektrik polarizasyon kuvveti ile arayüzeydeki azınlık spin alt bantlarındanın popülasyonun artışı doğru orantılı olup, spin polarizasyonu zayıflama eğilimi göstermektedir.

Acknowledgements

Saying thank you is a difficult task, since it contains the risk of misjudgment, vagueness. If somebody feels I am wrong, forgetful or too proud of myself in this acknowledgment, please accept my apologies.

I would hereby like to extend my gratitude towards all those persons because of whom I was able to accomplish the quality of scientific work evident in this thesis.

I would like to express my sincere gratitude to Assoc. Prof. Dr. I. Burç Mısırlıoğlu for accepting me as his Ph.D. student, not only supervising this thesis but changed also my viewpoint to whole my life. During my Ph.D. era, his enthusiasm and guidance for science and his endless support is a milestone in my life. The experiences I have gained during these years have been of utmost value.

I am deeply indebted to Berk Alkan, as we have been working as a mentor-protégé, member of the same company, and he has become an older brother of my family.

My special appreciation goes to Onur Ozensoy, Dr. A. Umut Soyler and Talat Tamer Alpak for providing me encouragement and moral support.

I am forever grateful to those, who have educated me during my academic career. This school showed me also the possibility of the transformation of a man to different person. Assoc. Prof. Dr. Fevzi Çakmak Cebeci, Prof. Dr. Mehmet Ali Gülgün, Prof. Dr. Clevea Ow-Yang, Assoc. Prof. Dr. Gozde Ince, Prof. Dr. Melih Papila, Prof. Dr. Mehmet Yıldız have the direct and indirect efforts on me to come to this day. They deserve more than a simple “thanks”.

Special credit is also due to Turgay Gönül for his contribution to develop my laboratory and survival skills.

I owe special acknowledgements to the many talented colleagues who I have had the pleasure working with Omid Mohammad Moradi, Efe Armagan, Oguzhan Oguz, Deniz Koken, Farzin Javanshour, L068 team (Mustafa Baysal, Melike Mercan Yildizhan, Güliz Inan Akmehmet, Hasan Kurt, Sirous Khabbazabkenar), Burçin Gül, Leila Haghihi Poudeh, Ipek Bilge, Lab Safety Team (Tuğçe Akkaş, Merve Senem Seven, Anastasia

Zakhariouta), Kaan Bilge, Ali Tufani, Yelda Yorulmaz, Tas family, our new group members Can Akaoglu and Wael Ali Saeed Aldulaimi at Sabancı University.

Last but not least, I would like to thank my family for their endless support on my unpredictable life journey. Whenever I mislead my myself, they have always been there to raise and straighten me.

Table of Contents

Acknowledgements.....	viii
Table of Contents.....	x
List of Tables	xi
List of Figures	xii
List of Symbols and Abbreviations	xviii
Preface	1
1 Introduction and Basic Concepts	3
1.1 Origins of Magnetism and Magnetic Data Storage Technology	5
1.1.1 Origins of Ferromagnetism.....	5
1.1.2 Magnetic Tunnel Junctions (MTJ).....	7
1.2 Origins of Ferroelectricity and Ferroelectric Data Storage Technology	10
1.2.1 Ferroelectric Tunnel Junctions.....	13
1.2.2 Resistive Switching in Metal/Ferroelectric/Semiconductor Junctions	33
1.3 Multiferroic Heterojunctions and Tunnel Junctions (MFTJ).....	40
1.3.1 Magnetoelectric Coupling.....	43
1.3.2 Multiferroic Tunnel Junctions (MFTJ).....	55
2 Results and Discussion	67
2.1 FM/FE/FM with FE having homogenous polarization.....	68
2.2 FM/FE/FM with FE having polarization obtained from equation of state ...	78
3 Conclusions.....	81
4 Future Work	82
References.....	84

List of Tables

Table 1.1 Performance of the current and in development memory devices [16-22]	4
Table 1.2: Material parameters and thermodynamic coefficients for BTO and STO used in the calculations[102].....	33
Table 1.3 Review of experimental results of tunneling resistance with FTJ	39
Table 1.4 Review of experimental results of tunneling resistance with MFTJ	56
Table 1.5 Band parameters for FE and FM	63

List of Figures

Figure 1.1 Analog to digital transformation of stored data on the world [7].....	3
Figure 1.2 Magnetization mechanism in terms of change in density of states[25]	6
Figure 1.3 The GMR effect in Fe/Cr superlattice (Reprinted from Ref. [26])	8
Figure 1.4 Room temperature TMR values of different insulating layers. [40]	9
Figure 1.5 Ideal hysteretic behavior of the ferroelectric polarization in an applied field	11
Figure 1.6 a) Free energy-polarization diagram of first-order phase transition at condition of $T > T_c$, $T = T_c$, and $T = T_0 < T_c$, b) and c) Spontaneous polarization and susceptibility upon temperature variation, d) Free energy-polarization diagram of second-order phase transition at condition of $T > T_0$, $T = T_c$, and $T = T < T_0$, e) and f) Spontaneous polarization and susceptibility upon temperature variation.[46]	12
Figure 1.7 Schematic of the origins of ferroelectric tunnel junction (FTJ) [77]	14
Figure 1.8 The domain width a in a ferroelectric capacitor versus the passive layer thickness d for different separations between the electrode plates [86].	16
Figure 1.9 Analyzed superlattices in the context of this work with three repeating units: a)repeating bilayer unit b), c) symmetrical unit	17
Figure 1.10 Stability map of the superlattices in the temperature (T)-layer thickness (l) plane: (a) of the superlattice consisting of bilayer units 1:critical thickness, 2:single domain-multi domain stability limit curve, 3,4: speculated variants for line of SD-MD first order phase transition (dashed curves). (b) The same for the superlattice consisting of symmetrical units with 5: critical thickness and 6: single-multi domain stability limit curve,7,8 is analog of 3,4. In (b), the bilayer case (solid black curve) is given for comparison [91].	18
Figure 1.11 Local changes in polarization along the film thickness, blue line shows the positive extrapolation length and red one shows the negative extrapolation length [92].	19

Figure 1.12 The diagram is divided into two main groups where the left side exhibits charge screening, allowing the ferroelectric state preserved uniformly in the sample where the right-hand side of the diagram illustrates conservation of ferroelectric state through the domain formation or rotation of polarization vector. Otherwise, the polarization is suppressed [100].	20
Figure 1.13 Phase diagrams of single-domain BaTiO ₃ (a) and PbTiO ₃ (b) epitaxial thin films grown on cubic substrates under compressive and tensile stresses.[102]	21
Figure 1.14 Sketch of tunneling process through a insulator layer between two metallic electrodes.	22
Figure 1.15 Simmons (a) and Brinkman(b) simplified model for tunneling	24
Figure 1.16 a-d) Resistive switching is shown in electronic level. e) I-V curve for resistive switching junctions. It shows resistance changes where the voltage is applied to the junction, current flow increases up to limit to set the area which is called LRS, when voltage is swept through the system, junction first goes “RESET, then HRS state.	34
Figure 1.17 Unipolar and bipolar resistive switching [118]	34
Figure 1.18 Computational flat-band results obtained from thermodynamic theory for a) BT and BST 5050 under 0 V bias and b) when under 0.5 V bias. Notice how the CB of BT “submerges” into the Fermi level (EF) under 0.5 V for this composition (under positive bias). The shaded regions indicate the locations of free electron accumulation. The green arrow in (a) and (b) indicates the direction of polarization. BST 5050 is only slightly influenced by the positive bias with lower conduction currents expected than that of in BT as also observed in experiments. Also note that the energy scales are different in (a) and (b) due the amount of band bending being different in both plots.	35
Figure 1.19 (a) Plot indicates the switching in high and low resistance states. (1) and (4) correspond to high-resistance and low resistance states respectively during the positive up-sweep and down-sweep. Switching from “up polarization” to “down polarization” occurs at (2). Almost no hysteresis occurs during (5) and (6) as polarization direction in the negative bias is fixed according to our thermodynamic calculation results. b) I-V quasi-static measurements in BT and BST 5050 films. Notice the hystereses in the positive bias regime of the BT. The up arrow indicates the jump in conductivity at the	

bias when polarization switches and starts pointing towards the NSTO interface while applying positive bias to top electrode. The arrow pointing down near zero bias indicates diminishing current while approaching zero bias after the max positive bias was already applied. (c) Schematic to demonstrate the direction of polarizations deduced from the experiments and thermodynamic calculations. Black arrow simply the polarization direction during the triangular bias-sweep (blue arrows). The vertical blue dashed lines denote the bias values where switching occurs during the sweep. Switching from “down polarization” to “up polarization” occurs at 2 as indicated in (a). 37

Figure 1.20 a) Classification of insulating oxides in the context of magnetic and electrical properties [164] and b) interaction in between stress, electric field, and magnetic field give rise to several coupling effects.[165] 41

Figure 1.21 Strain mediated magnetoelectric coupling in composite systems composed ferroelectric and magnetic layers a) direct ME effect b) converse ME effect 45

Figure 1.22 a) Temperature dependent magnetization change upon phase transition of BaTiO₃ b) Phase-dependent E-H_c diagram for rhombohedral, orthorhombic and tetragonal phases, respectively [184]. 46

Figure 1.23 a) Diffraction data of domain switching in BTO sample b) Magnetization change under applied electric field c) Magnetoelectric coupling variation under applied electric field via domain structure of BTO[183] 47

Figure 1.24 Spin configuration of FM-AFM heterostructure of an exchange biased hysteresis loop upon magnetization 49

Figure 1.25 a) SrRuO₃/SrTiO₃/SrRuO₃ heterostructure under external static and high frequency electric field [198] b) Average electron density with respect to free-standing 2.1 nm-thick Fe film under external electric field (E=0.1 V/nm). Dashed blue line represents minority spin electrons where red solid line represents majority spins. 50

Figure 1.26 a) Sketch of SRO-BTO heterostructure[199] with respect to different polarization directions b) Change in spin density of Ru atoms according to polarization direction c) non-spin polarized and d) spin-polarized local density of states (DOS) of Ru 3d orbitals which are responsible of itinerant magnetization in SRO layer. Solid blue lines represent the condition of polarization direction towards to SRO surface where red dotted

lines represent the condition of polarization away from SRO surface. Grey shaded area symbolizes the bulk DOS of Ru 3d. 51

Figure 1.27 a) Magnetization of LSMO with respect to temperature under charge depletion accumulation states induced by PZT ferroelectric layer [203]. Inset graph shows M-H loop at 100 K b) Magnetolectric hysteresis curve at 100 K, magnetic response is modulated via applied electric field through PZT. c) Magnetism control different cases where orange area symbolizes depletion and blue area symbolizes accumulation states of ferroelectric layer , and it is clearly seen that electric field modulate at zero magnetic field d) Magnetization upon depletion/accumulation states of LSMO/PZT heterostructure [205] e) and f) shows the magnetization-electric field hysteresis change magnetolectric coupling coefficient under different temperature conditions..... 52

Figure 1.28 a) Schematic of the effect of depletion and accumulation states spin configurations for LSMO in polarization direction change of PZT interface, showing the changes in the Mn and O orbital states and the expected changes in the magnetic moment per layer. The Mn d orbitals are shown orange and grey, and the p orbitals are shown around the oxygen atoms (red) [208] b) Distance dependent magnetization vs. n SLD result for STO/LSMO and STO LSMO/PZT stack is shown. c) Suppressed magnetization at the STO/LSMO interface is shown for both samples, whereas the LSMO/PZT/LSMO sample shows enhanced and diminished magnetization. Comparison with the LSMO/LAO/LSMO sample, which shows lower magnetization at the LSMO/LAO interface, confirms the field effect as the primary role for enhanced magnetization in LSMO in PZT/LSMO heterostructures [209]..... 54

Figure 1.29 Spin-selective tunneling in FM-I-FM stack. a) Magnetization of electrodes are parallel to each other b) Magnetization of electrodes are anti-parallel to each other. 57

Figure 1.30 Tunneling magnetoresistance depending on up and down spin alignment (or parallel and antiparallel alignment) of the layers..... 58

Figure 1.31 The schematic of the FM/FE/FM stack used to compute the spin dependent screening process. The single dashed line on the RHS FM electrode denotes the Fermi level of the stack. The arrow on the LHS FM electrode indicates the shift of the

electrostatic potential on this electrode depending on the sign of applied bias V (upper dashed line is negative bias, lower dashed line is positive bias for electrons). 59

Figure 1.32 The schematic for (a) the spin subband DOS, (b) shift of spin subband DOS near the interface with respect to the bulk and (c) resulting spatial spin distribution near the interface for majority (white arrow) and minority (red arrow) spins..... 60

Figure 2.1 Average carrier population density at the RHS FE/FM interface induced by homogeneous P_z for (a) $P_z = 0.1 \text{ C/m}^2$, (b) $P_z = 0.2 \text{ C/m}^2$ at 0V bias, (c) $P_z = 0.2 \text{ C/m}^2$ at 0.5V bias, (d) $P_z = 0.3 \text{ C/m}^2$ at 0V bias and (e) $P_z = 0.3 \text{ C/m}^2$ at 0.5V bias. Notice the minority spin accumulation for increasing P_z as well as bias. For the case of $P_z = 0.1 \text{ C/m}^2$ no plot when under bias is given as there is no considerable change in minority spin population at the interface. 70

Figure 2.2 Average subband LDOS at the RHS FE/FM interface induced by homogeneous P_z for (a) $P_z = 0.1 \text{ C/m}^2$, (b) $P_z = 0.2 \text{ C/m}^2$ at 0V bias, (c) $P_z = 0.2 \text{ C/m}^2$ at 0.5V bias, (d) $P_z = 0.3 \text{ C/m}^2$ at 0V bias and (e) $P_z = 0.3 \text{ C/m}^2$ at 0.5V bias. Notice the minority subband LDOS increasing at the interfaces for increasing P_z as well as bias 72

Figure 2.3 a) Atomic structure of Fe-4 layer of BaTiO_3 structure. b) Orbital-resolved DOS for interfacial atoms in a 4 layer of BaTiO_3 (a) Ti $3d$, (b) Fe $3d$, and (c) O $2p$. Majority- and minority-spin DOS are shown in the upper and lower panels, respectively. The solid and dashed curves correspond to the DOS of atoms at the top and bottom interfaces, respectively. The shaded plots are the DOS of atoms in the central monolayer of (b) Fe or (a),(c) TiO_2 which can be regarded as bulk[248]..... 73

Figure 2.4 Average population density (positive vertical axis) at the RHS FE/FM interface and the subband LDOS (given in the negative vertical axis) at the LHS FM/FE interface as a function of P_z . The blue arrow denotes indicates that almost fully spin polarized tunnelling will occur from RHS FE/FM interface states to subband LDOS of the LHS FM/FE interface states. Beyond values of P_z around 0.15 C/m^2 loss of spin polarization is expected as minority spin population starts to build up on the RHS FE/FM interface along with an increase in the minority subband LDOS on the LHS FM/FE interface as indicated by the shorter red arrow. 74

Figure 2.5 Total charge density across the trilayer indicating the exposed positive ionic sites on the LHS FM/FE interface and the carrier accumulation near the RHS FE/FM interface for 2 different P_z values. Stronger P_z causes a deeper penetration of the electric field to the RHS FM electrode increasing the effective barrier width to tunnelling for carriers on the LHS FE/FM interface. 76

Figure 2.6 Average potential barrier height for minority (down) and majority (up) spins as a function of P_z for 0V bias and 0.5V bias. The potential barrier for both type of carriers is reduced by the application of bias as expected. The sudden change in the barrier heights correspond to the regime when minority spin carriers participate in the screening of P_z 77

Figure 2.7 Tunnelling currents for minority and majority spins calculated using the WKB approximation for various homogeneous values of P_z (non-equilibrium, imposed P_z). As P_z gets stronger, mixed spin currents occur. For low P_z values (such as $P_z = 0.1 \text{ C/m}^2$ here) we find the current to be completely spin polarized and the down spin polarized currents are almost absent that cannot be plotted in the vertical log axis..... 78

Figure 2.8 Tunneling currents for minority and majority spins calculated using the WKB approximation for values of P_z obtained from equations of state for 2 different misfit strains, (b) the P_z profiles across the thickness of the FE and (c) the profile of the barrier obtained by superimposing the solution of \emptyset on the conduction band profiles of the stack. The shaded area on the LHS of the FM/FE interface denotes the region of carrier depletion, increasing effective barrier thickness..... 80

List of Symbols and Abbreviations

ME	: Magnetoelectric coupling
WKB	: Wentzel-Kramers-Brillouin
GMR	: Giant Magnetoresistance
MTJ	: Magnetic tunnel junction
TMR	: Tunneling magnetoresistance
FE	: Ferroelectric
FM	: Ferromagnet
AFM	: Antiferromagnet
BT	: Barium titanate
BST	: Barium strontium titanate
LSMO	: Lanthanum strontium manganite
STO	: Strontium titanate
SRO	: Strontium ruthenate
NSTO	: Niobium doped strontium titanate
BFO	: Bismuth ferrite
PZT	: Lead zirconium titanate
LAO	: Lanthanum aluminate
FTJ	: Ferroelectric Tunnel Junction
TER	: Tunneling electroresistance
SD	: Single domain
MD	: Multidomain

DRO : Destructive readout

NDRO : Non-destructive readout

CB : Conduction band

VB : Valence band

DMS : Diluted Magnetic semiconductor

DFT : Density functional theory

MFTJ : Multiferroic tunnel junction

DOS : Density of states

LDOS : Local density of states

LAS : Local available states

$g(E)$: Density of states

H : Magnetic field

χ : Magnetic susceptibility

μ : Magnetochemical potential

k_{TF} : Thomas-Fermi screening length

\hbar : Planck's constant

λ : Extrapolation length

T_c : Curie temperature

T_N : Neel temperature

μ_B : Bohr magneton

E_g : Energy gap

- D : Electric displacement vector
- HRS : High resistance state
- LRS : LRS resistance state
- ϵ_0 : Permittivity of free space (vacuum)
- ϵ_r : Relative permittivity
- ϵ_b : Relative background permittivity
- ρ : Spatial total charge density
- n^- : Donor population density
- p^+ : Acceptor population density
- N_D^+ : Ionized donor density
- LHS : Left hand side (Ferromagnetic/Ferroelectric interface)
- RHS : Right hand side (Ferroelectric/Ferromagnetic interface)
- P_x : In-plane polarization
- P_z : Out-of-plane polarization

“the ability to reduce everything to simple fundamental laws does not imply the ability to start from those laws and reconstruct the universe.”

P.W. Anderson (1972)[1]

Preface

The main focus of this thesis is to elucidate on the electric field control of magnetization and spin polarized tunneling behavior of artificial multiferroic devices composed of ferroelectric/ferromagnetic bilayers. In this work, we aim to understand the effect of spin dependent screening of polarization charges at a ferroelectric/ferromagnet junction from the perspective of electrostatic and thermodynamic relations in continuum media. Changes in carrier density at a metal surface in contact with a ferroelectric is well known since the first studies on metal/ferroelectric/metal capacitors. The electric field can penetrate into the metallic electrode depending on the amplitude of ferroelectric polarization and form what is called a “dead layer”. Thus, the screening of polarization by carriers does not occur right at the interface but at some distance from the interface on the electrode side. If the metal electrode is replaced with a ferromagnetic one, the screening process becomes spin dependent due to the existence of subbands of majority and minority spins that is determined by the strength of the exchange interaction. Electrostatic effects thus compete with exchange field that align spins in the magnetic electrodes, resulting in variation of screening of charges at the interfaces with respect to a conventional diamagnetic metal. Our results are expected to provide an intuitive understanding of results in studies focusing on use of ferroelectric layers to control spin degree of freedom in pin-selective tunnel junctions and magnetoresistance-based stacks.

Chapter 1 provides a historical and conceptual development of memory devices. Additionally, the basic concepts are covered to comprehend magnetic and multiferroic tunnel junctions are constituted in historical order. This review also supplies better perspective for conceptual understanding for performed activity in this thesis. This rather comprehensive introduction is helpful to analyze performed calculations within the theoretical basis of this thesis within the scope of thermodynamics, electrostatics and magnetism. Most prominent works on multiferroicity and electric field control of magnetism focus on experimental results and breakthroughs in this area, however, among these, there are only a few which explicitly and intuitively describe the spin dependent screening phenomena. This chapter also will also make the theoretical results themselves more lucid to those who are not familiar with the concepts in the following chapters.

The numerical approach with which the results were obtained is the focus of Chapter 2 and 3. These chapters describe the numerical calculations to understand the physics at the ferroelectric/ferromagnetic interfaces from a continuum perspective. As opposed to widespread belief, spin distribution of ferromagnetic layers may be weakened by electrostatic charge screening of ferroelectric dipoles. Understanding how magnetochemical potential and electrostatic charge screening impact the magnetoresistance of TMR stacks is a major the motivation of the thesis.

Last chapter of the thesis is about the future projection for spin dependent tunneling and tunneling magnetoresistance work and additional works with different approach.

1 Introduction and Basic Concepts

When the time of the invention of solid-state devices by Bardeen, Brattain, and Shockley [2, 3], microelectronic era has started and another giant leap was supplied by integrated circuitry [4, 5]. Today, von Neuman architecture for computers is still active where data storage unit is a memory and the data must be transmitted to central processing unit (CPU) to perform logic transactions [6]. Transistors led to computers and implicitly digitalization of the knowledge and information. Figure 1 also shows the produced data increase and transformation of data storage from analog to digital in last three decades. In addition to diagram given below, telecommunication, personal electronic devices, general and technical purpose computing and all other data transactions show the importance of data storage and processing capabilities [7]. According to the report [8], amount of data produced only in 2013 is equal to 90% (4.4 zettabytes) of data which has been generated in the entire civilization history. This value is expected to be 10 times bigger in 2020.

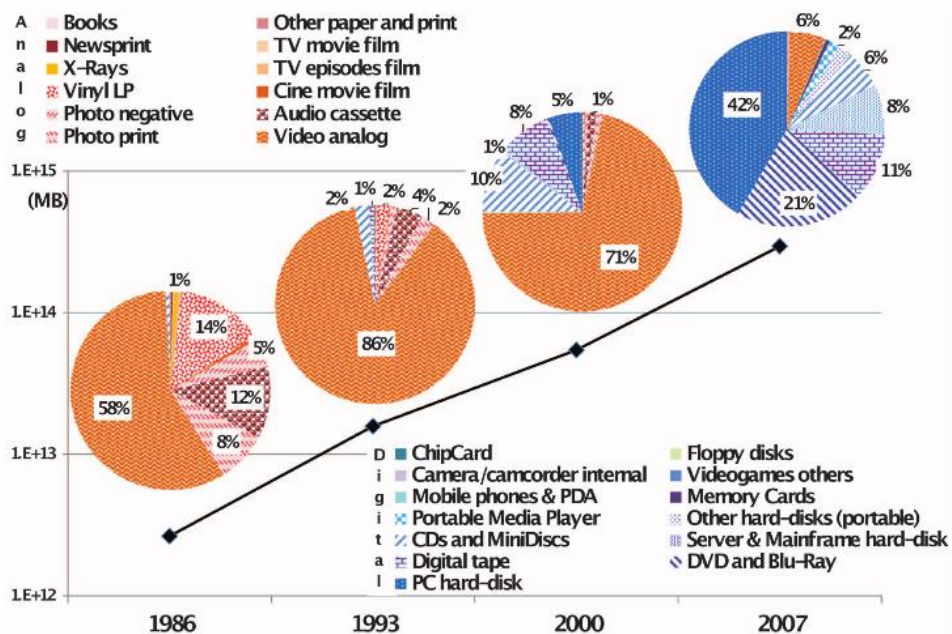


Figure 1.1 Analog to digital transformation of stored data on the world [7]

The empirical approximation on the progress of the transistors perceived by Gordon E. Moore known as “ Moore’s Law” [9, 10]; number of components and performance of integrated circuitry should have been doubled by a year and then it was revised as “two years”. Nowadays, Moore’s Law technologically has started to become obsolete [11] due

to physical limits such as scaling limits such as Heisenberg's uncertainty principle [12, 13] and heat dissipation capabilities [14] against deluge of data flow of 21st century. Therefore, new paradigm on non-volatile memory research is expected to stabilize effect, predicament in computation rate and data storage [15].

Table 1.1 shows performance of the current and in-development memory devices. In this manner, besides high performance, magnetic random-access memories (MRAM) and ferroelectric random-access memories (FeRAM) are extensive candidates for conventional non-volatile devices. Even, MRAM devices are matured and commercialized, power consumption and relatively low recording density problems are important problematic to overcome. Moreover, FeRAM devices have quite low power consumption and high recording capacity, in contrast, main restrictions appear as destructive readout process, complex production line, and scalability limit.

In next generation devices, miniaturization of devices will pave the way of tunneling effects on research and development of non-volatile memory devices.

Table 1.1 Performance of the current and in development memory devices [16-22]

	In – production					In – development	
	FeRAM	MRAM	NOR Flash	DRAM	SRAM	<i>STT- RAM</i>	MeRAM
Cell size (F ²)	40-20	25	8	6-10	>30	6-30	4-8
Read time (ns)	20-80	3-20	10	30	1	1-20	1-20
Write time (ns)	50/50	3-20	1000	20	1	1-20	1-20
Endurance(cycles)	10 ¹²	>10 ¹⁵	10 ⁶ -10 ⁷	>10 ¹⁶	>10 ¹⁶	>10 ¹⁶	>10 ¹⁶
Non-volatility	Yes	Yes	Yes	No	No	Yes	Yes
Energy/bit (fJ)	10	7000	10 ⁶	1000	100	100	<1
Data retention	10 years	20 years	10 years	<<second	0	10 years	10 years
FeRAM: Ferroelectric random-access memory			SRAM: Static random-access memory				
MRAM: Magnetic random-access memory			STT-RAM: Spin torque transfer random access memory				
DRAM: Dynamic random-access memory			MeRAM: Magnetoelectric random access memory				

1.1 Origins of Magnetism and Magnetic Data Storage Technology

1.1.1 Origins of Ferromagnetism

Spins of electrons and their orbital motion in the atoms carry the magnetic properties of materials. Properties of magnetism are determined by electronic arrangement and crystal structure of the material. The spin-ordering mechanisms of magnetic materials due to diversity in atomic arrangement and exchange interactions of atoms leads to the following types of magnetism: diamagnetism, ferromagnetism, antiferromagnetism, ferrimagnetism, and paramagnetism.

Pauli principle [23] which asserts the condition that the perturbation of the wave function in spatial coordinates by symmetry of the spin variant and electrostatic interaction between electrons are mediate altered.

Moreover, Hund's rules [24] which proclaim the quantum numbers for ground states of atoms adopt ferromagnetism: spontaneous ordering of magnetic moments that are resulted in non-zero orbital momentum and electron spin in the absence magnetic field.

d shell electrons of *3d* metals, where located in the outermost shell of the atom, are carriers orbiting around atoms itinerantly, whereas *f* shell electrons of *4f* rare-earth elements, placed relatively closer to the core, are localized at discrete atoms. Consequently, the magnetic moment of *4f* elements is individually localized for every atom but collective behavior of nearly free electrons of *3d* metals form band structure. Thus, a limited number of elements such as *3d* transition metals (Co, Ni, Fe, Mn) and *4f* rare-earth elements (Gd, Tb, Dy, etc.) as well as *5f* elements present ferromagnetism among all elements in the periodic table.

Namely, wave vectors of free electrons which occupy up to highest energy state called Fermi energy, E_f , with available quantized energy levels, called density of states $g(E)$, and according to Pauli exclusion principle, each standing wave or stationary state resided in by two electrons with up and down spins. When a magnetic field H , with the same direction of + spins is applied, density of states of + and - spins will be reconfigured by reversing spin according to the alignment and Fermi level of the compound will be

equalized in between + and – spin electrons. Hence, (-) spin electrons will move to (+) spin band level by the phenomena called *exchange interaction*. + spin direction will be lowered by an amount that follows:

$$E_H = 2\mu_B H \quad \text{Equation 1.1}$$

where μ_B is Bohr magneton. Number of electrons, Δn , reflected as area change in density of states in between + and - spins in Fig. 1.2.

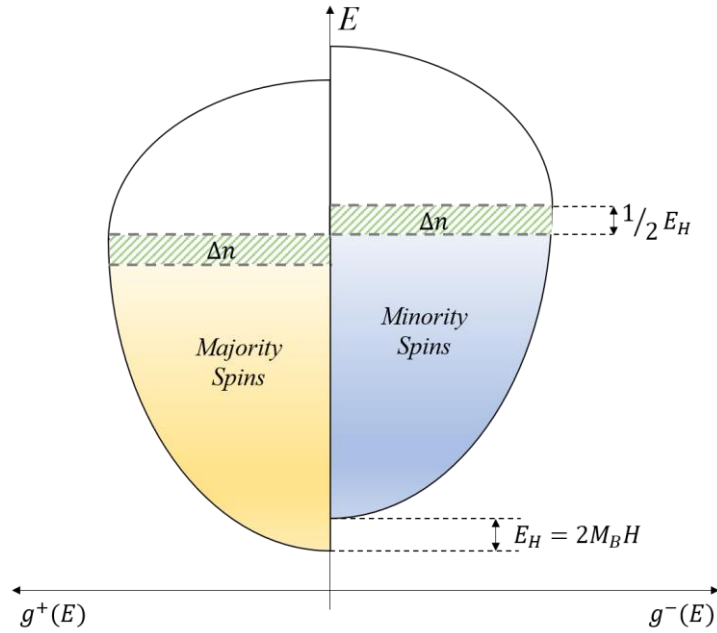


Figure 1.2 Magnetization mechanism in terms of change in density of states[25]

$$\Delta n = g(E_f) \cdot \frac{E_H}{2} = g(E_f)\mu_B H \quad \text{Equation 1.2}$$

$$\Delta I = 2\mu_B \Delta n = 2g(E_f)\mu_B^2 H \quad \text{Equation 1.3}$$

This transfer generates additional magnetization, ΔI in the system (Eq. 1.3) whereupon the susceptibility which is correlated to *Pauli paramagnetism* is given as

$$\chi_p = 2g(E_f)\mu_B^2 \quad \text{Equation 1.4}$$

Equation 1.4 presents that susceptibility χ is temperature-independent term while the Fermi level is strongly correlated to temperature as the result of *Fermi-Dirac distribution*

(Eq. 1.5). Thermal excitation affects the probability to find an electron in a state where energy level E , which is above the Fermi level.

$$f = \frac{1}{\exp\left(\frac{E-E_f}{kT}\right)+1} \quad \text{Equation 1.5}$$

It is clearly seen that the susceptibility is function of density of states at the Fermi energy level. Thermal variance in the compound slightly deviates the Fermi level (Eq. 1.6)

$$N = \int_0^{\infty} f(E)g(E)dE \quad \text{Equation 1.6}$$

Band splitting in ferromagnets as previously mentioned + and – spin electron distribution is stronger than paramagnets due to exchange field values H_m by a range of 10^2 - 10^3 [25]. Distribution and extent of magnetization is written as

$$N_+ = \int_{-\infty}^{+\infty} g(E)f(Ef + \mu_B H_m)dE \quad \text{Equation 1.7}$$

$$N_- = \int_{-\infty}^{+\infty} g(E)f(Ef - \mu_B H_m)dE \quad \text{Equation 1.8}$$

$$I = \mu_B(N_+ - N_-) \quad \text{Equation 1.9}$$

By definition, ferromagnets have spontaneous magnetization where Eq. 1.7&1.8 is satisfied and determined by density of states at/close to Fermi level which contains the electrons mainly contributes to ferromagnetic behavior.

1.1.2 Magnetic Tunnel Junctions (MTJ)

Methods of data storage such as hard disk and magnetic bands are still concerned with magnetism due to the high data storing capacity and their low-cost-action. Charge-driven-semiconductor-device memories, which are critical elements for microcontrollers, battery-supplied personal electronics, are utilized to store data permanently or temporarily, could operate relatively faster and could be smaller than magnetic devices. An ideal non-volatile solid-state memory would combine the best properties of two phenomenal trend: high speed and high-storage capacity.

Remarkable development in magnetism in industrial, experimental, and theoretical research has occurred in the fourth quarter of the 20th century. One might expect that

novelties in magnetism-oriented research will diminish due to that all physical and theoretical understanding and that its limits have been already projected until now.

Nevertheless, spin-selective conduction, suggested by Mott, and discovery of “Giant Magnetoresistive” (GMR) behavior between Fe/Cr multilayer by Baibich et. al. [26] and Binasch et. al. [27] separately, which led Albert Fert and Peter Grünberg to Nobel Physics Prize in 2007, are accepted as birth of “spintronic” science. GMR effect has found prominent ground in the field of sensor technology dominantly hard drive heads, while “Tunnelling Magnetoresistance” (TMR) behavior proposed by Julierre, realization by other groups [28-31] has become the future of non-volatile random access memories starting from Datta-Das spin transistor [32] to Magnetic Tunnel Junctions (MTJ), MeRAM, STT-RAM and many other designs [33].

Origin of GMR effect arise from the electron scattering in spin-selective transport between FM-M-FM junctions (Fig.1.3). The parallel magnetization direction of ferromagnetic layers under magnetic field, spin-dependent scattering of the electrons converges to minimum. This state taken as “low-resistance” state whereas the opposite magnetization directions of the ferromagnetic electrodes results in “high resistance” state (maximum spin-scattering).

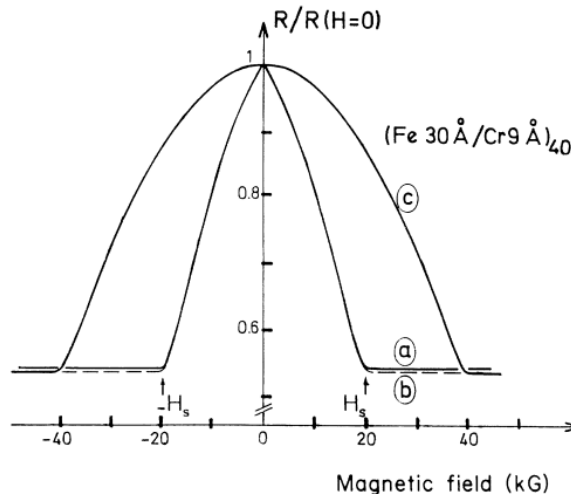


Figure 1.3 The GMR effect in Fe/Cr superlattice (**Reprinted from Ref. [26]**)

Difference between TMR and GMR effect stem from structural difference where TMR is observed in FM-DE-FM which is observed in magnetic tunnel junctions (MTJ). In addition to this, in conventional FM/DE/FM TMR stacks, one can obtain spin polarized tunnelling currents that are determined by the spin states of electrons in the FM electrodes.

TMR junctions consist of two FMs separated by a thin layer of dielectric, which direction of magnetic spins generate high and low resistance as ON/OFF by spin-selective scattering. In the case of TMR principal process conducted by quantum mechanical tunneling apart from GMR effect. The spin polarization and magnitude of currents across a TMR stack depends on the relative orientation of the magnetism in the FM electrodes and a bias simply controls the electrical barrier to spin tunneling via the polarization of the dielectric.

These approaches triggered further works in the magnetic tunnel junction in next decades as seen Fig. 2.13. Integration of crystalline MgO barrier in MTJ has increased the TMR values dramatically. %220 TMR value for Fe/MgO/Fe junction was reported by Parkin et. al.[34], right after, Yuasa et al. reported 88% for fully epitaxial Fe(001)/MgO/Fe(001) stack[35]. %604 TMR value was reported via using metallic ferromagnets in CoFeB/MgO/CoFeB stack at room temperature[36]. Apart from ferromagnetic metallic electrodes; manganites has started to be the focus of novel material group as “half-metallic ferromagnetic oxide” in 1996 by Lu et. al. [37] and Sun et. al. [38]. However, these efforts have only reached TMR value of % 83 at 4.2 K. Additional work of Sun et. al. were reported a TMR value increased to 400 % where spin polarization is 81 % [39].

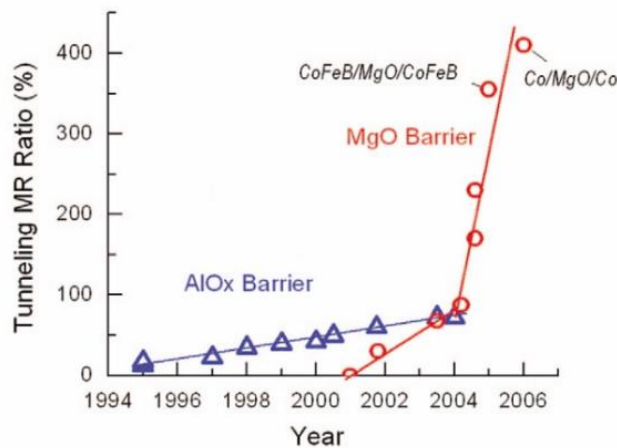


Figure 1.4 Room temperature TMR values of different insulating layers. [40]

Another work constitutes LSMO/STO/LSMO stack reporting %450 TMR value at 4.2 K was published by Viret et. al.[41]. Subsequently, Sun. et. al.[42] and Bowen et. al.[43] reported dramatic increase in TMR value of %1850 which corresponds to 95 % spin polarization for LSMO/STO/LSMO stack.

1.2 Origins of Ferroelectricity and Ferroelectric Data Storage Technology

Perovskite ferroelectrics are the large group of compounds with general formula of pseudo-cubic ABO_3 where A is monovalent, divalent, or trivalent cation and B is penta, tetra or trivalent cation, respectively. Ferroelectricity could be defined as materials with reversible spontaneous polarization under zero electric field. The concept of FeRAM arose from the remnant polarization of the ferroelectrics corresponding to binary elements “1” and “0” as recording media. FeRAM devices are distinguished in the basis of readout techniques: Destructive readout (DRO) and non-destructive readout (NDRO)[44].

The source of polarization in this group of materials originates from asymmetric arrangement of an ion in a non-centrosymmetric unit cell, which produces an electric dipole moment.

Dipole moment could simply be written as

$$p = qd \quad \text{Equation 1.10}$$

where q is net charge and d , vector distance directed from the negative to the positive charge. Summation of medium consisting of N number of polarized unit cell results in polarization density where

$$P = Nqd \quad \text{Equation 1.11}$$

Net charge in a volume governed by integration of polarization charge density over unit volume:

$$Q = \int \rho_p dV \quad \text{Equation 1.12}$$

where ρ_p is polarization charge and Poisson equation gives relation between charge density and polarization density P .

Randomly distributed domains ($P=0$) are started to form towards electric field direction (1). Total polarization gradually increases up to saturation point (P_s) (2). Further increase in the electric field results in dielectric charging and additional polarization increase (3). When the electric field returns to zero, polarization reaches remanence value (P_r).

Coercive field ($-E_c$) is a limit point that polarization state switch suddenly. The hysteresis loop is closed by polarization saturation (6) at specific electric field.

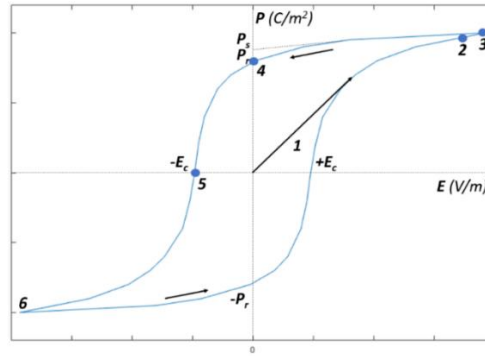


Figure 1.5 Ideal hysteretic behavior of the ferroelectric polarization in an applied field

Observation of hysteresis and spontaneous polarization behavior on Rochelle salt has led to the discovery of ferroelectric phenomena by Valasek [45]. The theory of ferroelectricity was matured by Landau's phenomenological theory based on Landau's theory of second-order phase transition. Electric field can switch polarization direction where the relative energy change in $-\vec{E} \cdot \vec{P}$ was modified by these coupled terms. The order parameter in the Landau theory could be postulated as having the same transformation characteristics with the polarization vector \vec{P} and the Gibbs free energy density G is expressed in the Landau-Ginzburg polynomial expansion

$$G = F - EP = F_0 + \frac{\alpha}{2}P^2 + \frac{\beta}{2}P^4 + \frac{\gamma}{2}P^6 - EP \quad \text{Equation 1.13}$$

where F_0 relates to the free energy of the paraelectric phase under zero electric field, E is the electric field, and α , β , γ are temperature and pressure-dependent expansion coefficients. Free energy density minima where $\frac{\partial F}{\partial P} = 0$ and $\frac{\partial^2 F}{\partial P^2} = 0$ account for equilibrium conditions where

$$\frac{\partial F}{\partial P} = P(\alpha + \beta P^2 + \gamma P^4) = 0 \quad \text{Equation 1.14}$$

$$\frac{\partial^2 F}{\partial P^2} = (\alpha + 3\beta P^2 + 5\gamma P^4) > 0 \quad \text{Equation 1.15}$$

One might distinguish the phase transition of ferroelectrics as first (e.g. BaTiO₃ and other perovskites) and second order (e.g. triglycine sulfate (TGS)) in the context of crystal structure

undergoing into new one via sudden or continuous change. Fig. 1.6 shows explicitly the phase transition kinetics upon cooling from T_c to ferroelectric phase. Above the Curie temperature (shown as $(T \gg T_c)$) higher symmetry paraelectric phase is highly stable where $P=0$ at $\alpha > 0$. Metastable ferroelectric phase ($\pm P_s \neq 0$) starts to nucleate along with paraelectric phase simultaneously while the temperature is just above the T_c (shown as $(T > T_c)$). Paraelectric and ferroelectric phases coexist at $(T = T_c)$ condition. At a temperature below the Curie temperature (shown as $(T_c > T > T_0)$), non-centrosymmetric ferroelectric phase starts to govern and also mitigated paraelectric phase is also observed. Spontaneous polarization arises remarkably due to discontinuity. Below the Curie-Weiss temperature (T_0), stable ferroelectric phase dictates the whole crystal (shown as $T < T_0$). Taking into consideration free energy for first order phase transformation with coefficients $\alpha = 1/\epsilon_0 C (T - T_0)$, $\beta < 0$ and $\gamma \geq 0$, polarization is given as

$$P_s^2 = \frac{|\beta| + \sqrt{\beta^2 - 4C^{-1}(T - T_c)\gamma}}{2\gamma} \quad \text{Equation 1.16}$$

For second-order phase transition, free energy is expanded up to fourth order and $\beta > 0$. With this assumption, polarization corresponds to either zero or

$$P_s^2 = -\frac{(T - T_c)}{\beta C} \quad \text{Equation 1.17}$$

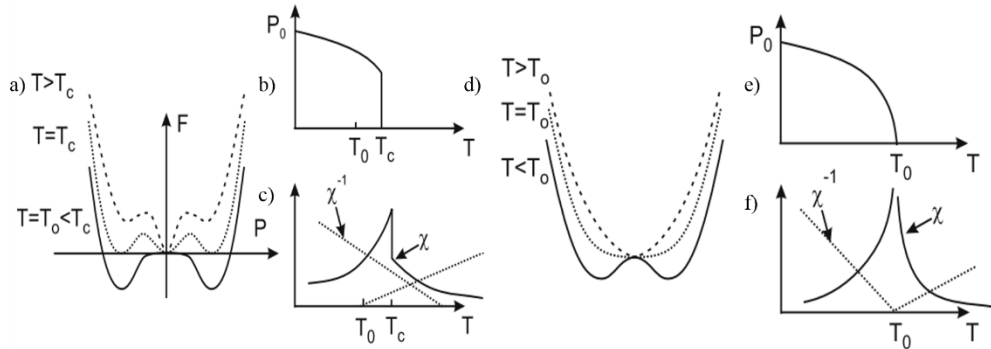


Figure 1.6 a) Free energy-polarization diagram of first-order phase transition at condition of $T > T_c$, $T = T_c$, and $T = T_0 < T_c$, b) and c) Spontaneous polarization and susceptibility upon temperature variation, d) Free energy-polarization diagram of second-order phase transition at condition of $T > T_0$, $T = T_c$, and $T = T < T_0$, e) and f) Spontaneous polarization and susceptibility upon temperature variation.[46]

In second order phase transition phenomena, phase transition and Curie-Weiss temperature values are nearly same, but the crucial point is the order parameter where is taken 0.5. Spontaneous polarization value is directly proportional to $(T - T_c)^\beta$. Polarization value goes to zero (stable minima) while the temperature is equal to phase transition temperature. Systematic temperature drop shifts the polarization minima to finite values. In brief, continuous variation in polarization, entropy, specific heat-jump and inversely proportional susceptibility indicates the second order phase transition characteristics.

1.2.1 Ferroelectric Tunnel Junctions

The tunnel junctions with a dielectric layer sandwiched between two metals is very well studied and understood and will not be given consideration here. Replacing the dielectric with a ferroelectric layer has a dramatic impact on the barrier the electrons see during tunneling. The concept of FTJ relies on thin ferroelectric being the barrier layer instead of insulating layers where Esaki et al. laid the first foundations for FTJs [47]. This way, a new novel device architecture in the name of “polar switch” via current-voltage characteristics of ferroelectrics upon electric field, unlike other barrier elements.

Polarization-reversal of FE layer upon electric field, hence the polarization charges at the interface, controls ON/OFF states of the junction. Technological and theoretical development in last two decades enabled the growth of epitaxial FE layers down to atomic layer scale which is critical condition for the tunneling phenomenon. As result, experimental realization of this phenomenon has had to wait until 2003[48].

Most of the experimental works of FTJ includes BaTiO₃, PbTiO₃, and PbZr_xTi_{1-x}O₃ as the barrier layer, besides LSMO and SRO are grown as bottom electrode due to low lattice mismatch which stabilizes the out-of-plane polarizability of the barrier [49-66]. Top electrode is either metal or another conductive oxide layer. Replacement of metal electrode with semiconductor layer due to the higher screening length, hence the change in penetration of electric field inside electrode surface was reported by Wen et. al[67]. Pt/BaTiO₃/Nb: SrTiO₃ stack reached 10⁴ TER value due to charge accumulation/depletion at the semiconductor surface. Several other ultrathin ferroelectric layer including stacks has the effect of tunneling/tunnel junction and memristor behavior[60] with tunability of the resistance of junction. Moreover, latter studies have

clearly shown that the ferroelectric state could be preserved down to few atomic layers [68-72]. The driving force behind such a pursuit was that the FE polarization can dramatically alter the on/off ratios of currents depending on the direction of remnant dipoles as they can easily be switched under a few volts of bias. FE TJs sandwiched between metal and semiconductor electrodes have already been proven to generate on/off ratios reaching 10^3 - 10^5 [55, 63, 67, 73-76]

Resistive switching-based approach of Contreras et. al. proved that the origin of resistance switching occurs via ferroelectric polarization reversal. In Fig. 1.7, the elements that affect the electron transport through the ferroelectric barrier are given as[77]:

- Strain arises from piezoelectric behavior of ferroelectric layer under applied electric field where the charge transport characteristics strongly correlated to the barrier thickness and attenuation constant.
- Partially screened ferroelectric bound charges where arises electrostatic potential.
- Opposite polarization states govern tunneling probability through atomic orbital hybridization.

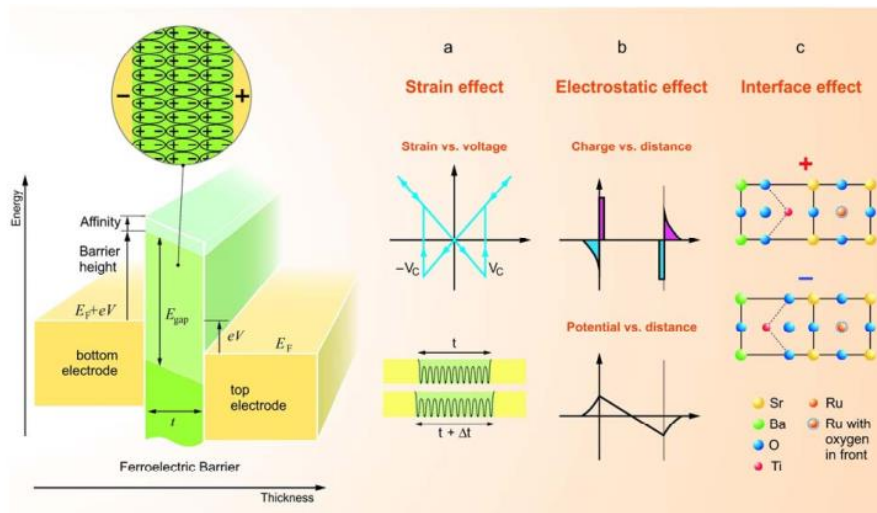


Figure 1.7 Schematic of the origins of ferroelectric tunnel junction (FTJ) [77]

Additional evidences of resistive switching mechanism of ferroelectric for differing thicknesses was reported underlying the ferroelectricity and the electron tunneling [78, 79]. As it is mentioned in Fig. 1.7, tunnel resistance is the function of potential height in the barrier where incomplete charge screening of polarization originated charges controlled via ferroelectric polarization reversal [80]. However, potential height is not

the only element on tunnel resistance but also modulation of potential width via ferroelectric layer juxtaposed with two metallic layers of dissimilar screening lengths plays significant role on enhancement of TER.

Ferroelectrics as wide bandgap semiconductor are subjected to Schottky characteristics between film and electrode interface, band parameters and other electronic properties of electrodes are decisive rather than the size effect [81-84]. From electrostatics approach to the problem starts from uncompensated charges come into play as electrostatic potential at the FE/electrode interface. The formation of passive layer (dead layer) due to uncompensated charges at the ferroelectric/electrode interface principally affects the screening length, hence the domain formation.

Thomas-Fermi screening length is function of electronic density of states at the Fermi level. The Thomas-Fermi theory delivers an approximation where the non-interaction electron gas under given external potential as function of local charge density[85] in which Thomas-Fermi wavevector:

$$k_0^2 = 4\pi e^2 \frac{\partial n}{\partial \mu} \quad \text{Equation 1.18}$$

where μ chemical potential at Fermi level of the given solid, n is electron concentration, e is the elementary charge.

$$k_0^2 = 4\pi e^2 n / (k_B T) \quad \text{Equation 1.19}$$

$1/k_0$ corresponds to Debye length. If we translate Thomas-Fermi screening vector into atomic units:

$$k_{TF}^2 = 4 \left(\frac{3n}{\pi} \right) \quad \text{Equation 1.20}$$

where $k_0^2 = k_{TF}^2 (m_e / \hbar)$. The Thomas-Fermi screening length for metals in the order 0.5-1.0 Å whereas, the Debye length for a semiconductor is nanometer level. Penetration of the electric field into the electrode creates passive layers inside.

Appearance of the dead layers constitutes depolarizing field in the ferroelectric layer. Dissipation of the field is provided by the transformation of domain structure from single domain to multidomain state. Domain and domain wall formation is the material reaction

to reduce energy imbalance originates from depolarizing field and energy cost of the domain wall formation. Depolarizing field is also result of spatial polarization instability of the film due to surface effects.

It could be assumed that the single domain state could achieved when the thickness of the passive layer d is zero. Bratkovsky et. al. [86] has also proposed universal mechanism to propose direct relation between passive layer thickness d and dielectric constant of the passive layer ϵ_g :

$$\frac{dP}{dE} \propto \frac{\epsilon_g}{d} \quad \text{Equation 1.21}$$

Fig. 1.8 shows the domain width a in ferroelectric capacitor versus passive layer thickness d for different lengths of separation. W also shows the domain wall thickness. Inset of Fig.1.8 demonstrate that the ferroelectric capacitor under bias U . Sharp (exponential) wide domain transition could be clearly seen where the passive layer thickness goes to zero. The growth of a passive layer at electrode surface results in domain split in FE layer. These findings also is explanatory for the coercive field decrease in FE.

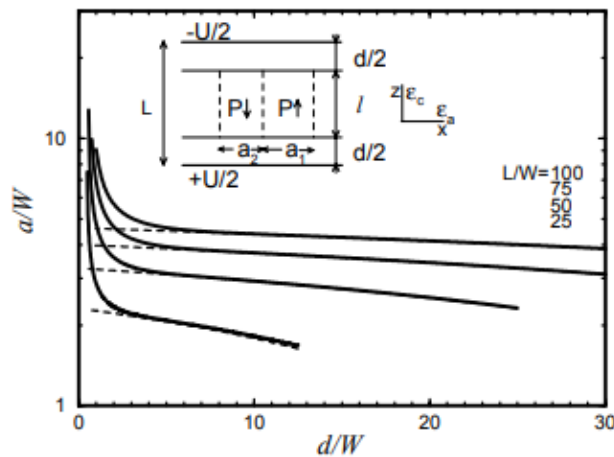


Figure 1.8 The domain width a in a ferroelectric capacitor versus the passive layer thickness d for different separations between the electrode plates [86].

Another important findings on single domain stability is investigated by numerical analysis of Misirlioglu et.al. [87] in a superlattice. Variation of dielectric constant between the paraelectric SrTiO_3 layer which has larger dielectric constant and ferroelectric layer BaTiO_3 . Expected transition trend might arise as:

- a. Domain period of the structure is larger than the ferroelectric layer thickness (non-Kittel regime). This condition previously proposed for thin films [88] and also and ferroelectric-paraelectric superlattices[89]
- b. Quasi-Kittel regime where it was demonstrated as [90] narrow domain period proportional to $l_f^{1/3}$ (l_f is the thickness of ferroelectric layer).

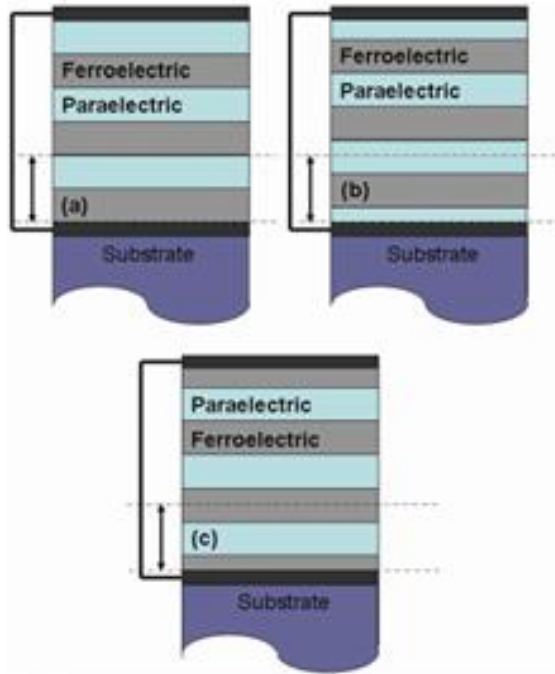


Figure 1.9 Analyzed superlattices in the context of this work with three repeating units: a) repeating bilayer unit b), c) symmetrical unit.

Single domain and multidomain states are indicated in Fig.1.10 upon stability regions of ferroelectric and paraelectric state. Figure 1.9b illustrates the case of “near the electrode for the previously given two types of superlattices. This analysis also supports the results given in the work of Bratkovsky et. al. [86]. Near the electrode region, stability diagram drastically changes. Continuity problem arises when the stability line of SD-MD boundary in the ferroelectric phase is crossed, continuity starts to disappear. Finite amplitude of inhomogeneous polarization distribution (MD state) is observed at the point where the stability disappears. The stability loss arises somewhere inside the region, below the paraelectric-MD transition. When the free energies of two phases is equalized, thermodynamic temperature of the first order transition could exist at lower temperature.

Single domain state becomes energetically favorable equilibrium state by decreasing temperature.

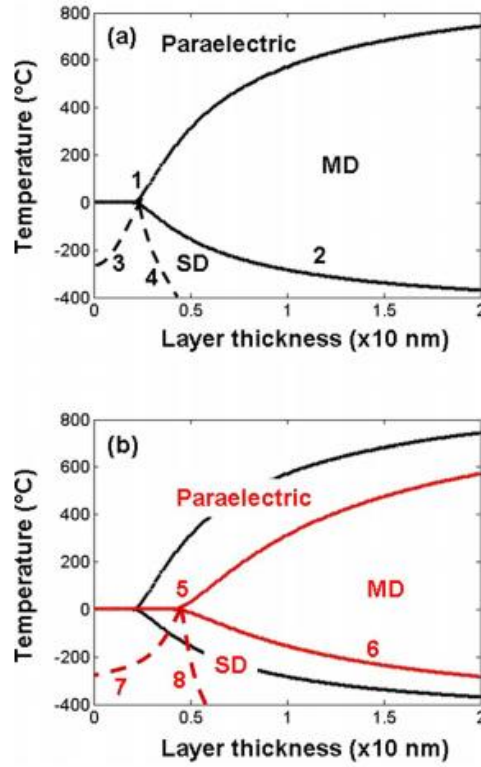


Figure 1.10 Stability map of the superlattices in the temperature (T)-layer thickness (l) plane: (a) of the superlattice consisting of bilayer units 1:critical thickness, 2:single domain-multi domain stability limit curve, 3,4: speculated variants for line of SD-MD first order phase transition (dashed curves). (b) The same for the superlattice consisting of symmetrical units with 5: critical thickness and 6: single-multi domain stability limit curve,7,8 is analog of 3,4. In (b), the bilayer case (solid black curve) is given for comparison [91].

Inhomogeneous Landau-Devonshire theory describes and takes in consideration the polarization in proximity of the surface. The free energy description given by Kretschmer and Binder where

$$F_{film} = F_{bulk} + F_{surface} \quad \text{Equation 1.22}$$

introduces a new term “*extrapolation length* (λ)” which is a measure of subsurface layer coupling. Local polarization values in the vicinity of the surface vary over a distance proportional to correlation length ξ of polarization instability [92]. Sign of the λ is positive

in general, however, it could be negative where the correlation length value is smaller than extrapolation length [93]. Several works have focused on the correlation length and extrapolation length on ferroelectric properties in terms of depolarizing field [94-96]. Numerically evaluated critical thickness values for PbTiO_3 and $\text{Pb}_{0.5}\text{Zr}_{0.5}\text{TiO}_3$ at 0 K are 4 and 8 nm respectively [97]. Fig.1.11 shows the relation between extrapolation length and polarization along the thickness of the film.

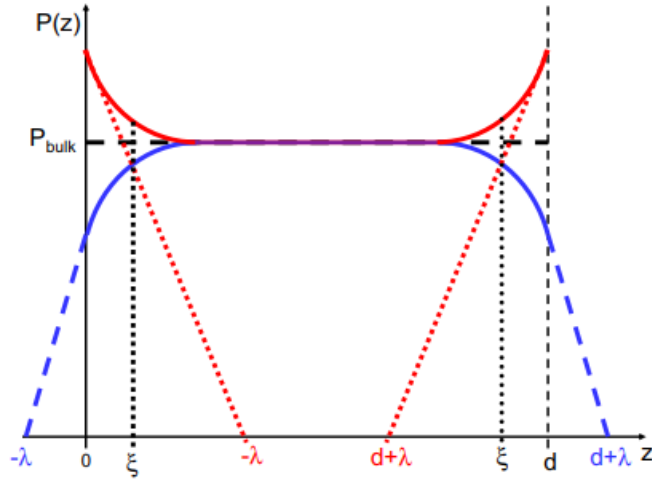


Figure 1.11 Local changes in polarization along the film thickness, blue line shows the positive extrapolation length and red one shows the negative extrapolation length [92].

Figure 1.12 indicates several mechanisms taking part to compensate in depolarizing field in thin films structures. Apart from atmospheric adsorption contribution, size limitation, in other words paraelectric-ferroelectric thickness limit is related to several phenomena such as characteristics of the electrode-film interface mediately boundary conditions, strain, domain formation [86, 98, 99].

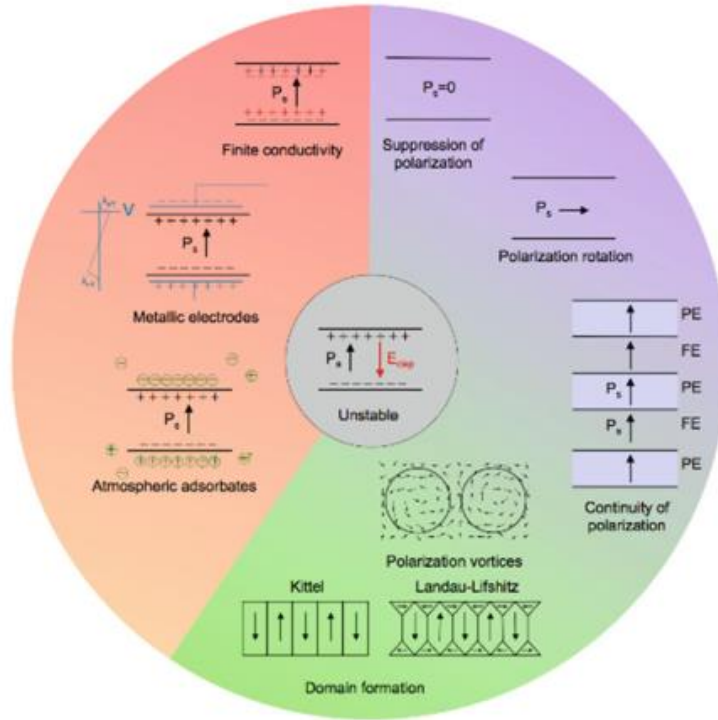


Figure 1.12 The diagram is divided into two main groups where the left side exhibits charge screening, allowing the ferroelectric state preserved uniformly in the sample where the right-hand side of the diagram illustrates conservation of ferroelectric state through the domain formation or rotation of polarization vector. Otherwise, the polarization is suppressed [100].

Another prominent parameter is the substrate-film and film-film interactions. Mechanical stresses arise from lattice mismatch and growth conditions of the thin film on the substrate. Additionally, these so-called misfit strains are also observed in thin film interlayers in multilayer stacks that can impact the transition characteristics.

Lattice parameters are deformed by substrate-induced strain and more likely differ from the bulk values of the material. A misfit strain S_m is introduced into theoretical calculations apart from the current polarization state of the film to define the substrate as external factor on the ferroelectricity. Mostly used cubic substrates such as MgO, SrTiO₃, LaAlO₃ constitutes strain which is defined as

$$S_m = \frac{b-a_0}{b} \quad \text{Equation 1.23}$$

where b is the substrate lattice parameter and a_0 is the equivalent cubic cell constant of the free-standing film [101]. When the critical thickness is exceeded, misfit dislocations emerge in the film and effective lattice parameter is modulated as b^* :

$$S_m = \frac{b^* - a_0}{b^*} \quad \text{Equation 1.24}$$

Thermodynamic calculations have shown that S_m is strongly effective on polarization direction and its magnitude [102]. In brief, ferroelectric thin film grown on tensile stress applying substrate which means $S_m > 0$, form a ferroelectric phase with in-plane polarization direction, whereas, compressive strain ($S_m < 0$) has the capability to stabilize out-of-plane oriented ferroelectric phase and enhanced polarization. Hence, the ferroelectric-paraelectric phase transition temperature also deviates from bulk value (Fig.1.13) [94, 95, 103].

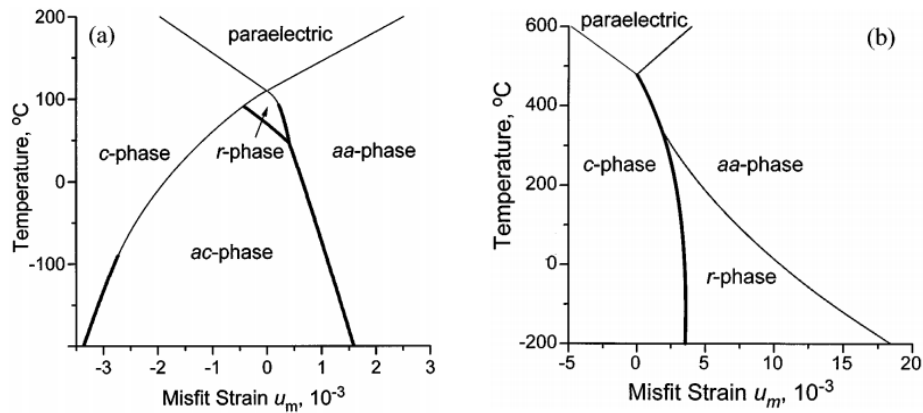


Figure 1.13 Phase diagrams of single-domain BaTiO₃ (a) and PbTiO₃(b) epitaxial thin films grown on cubic substrates under compressive and tensile stresses.[102]

Recently, total free energy expansion of ferroelectric thin film has several internal factors which contribute to the entire system and several works has shown that existence of the ferroelectricity is down to few monolayers. The micrometer scale has reached nanometer level over time significantly due to improvement in theoretical predictions about ferroelectric by understanding the mechanical and electrical boundary conditions and the analytical experimental techniques.

FTJs, unlike regular dielectrics, can display rather arbitrary potential barrier shapes owing to the penetration of the ferroelectric polarization into the electrodes. Such an outcome often necessitates the treatment of arbitrary potential barriers that can be incorporated into the estimation of tunneling currents through FTJs via the WKB treatment.

WKB approximation is a method for derivation of tunnel currents in tunneling junctions by treating barriers with complicated shape without extreme variation. Conductor layers at each side of the insulator layer has discrete energy levels, which is called Fermi level, (E_{f_1}, E_{f_2}) at absolute zero level. This band model proposed for a system that has different barrier heights of different metals as ϕ_1 and ϕ_2 . W_1 and W_2 represent the work functions of the metal where is energy minima to eject an electron from the material at 0 K. E_g and χ are energy gap and electron affinity of the barrier respectively. If a bias voltage is applied across the barrier, Fermi levels of M_1 and M_2 will shift.

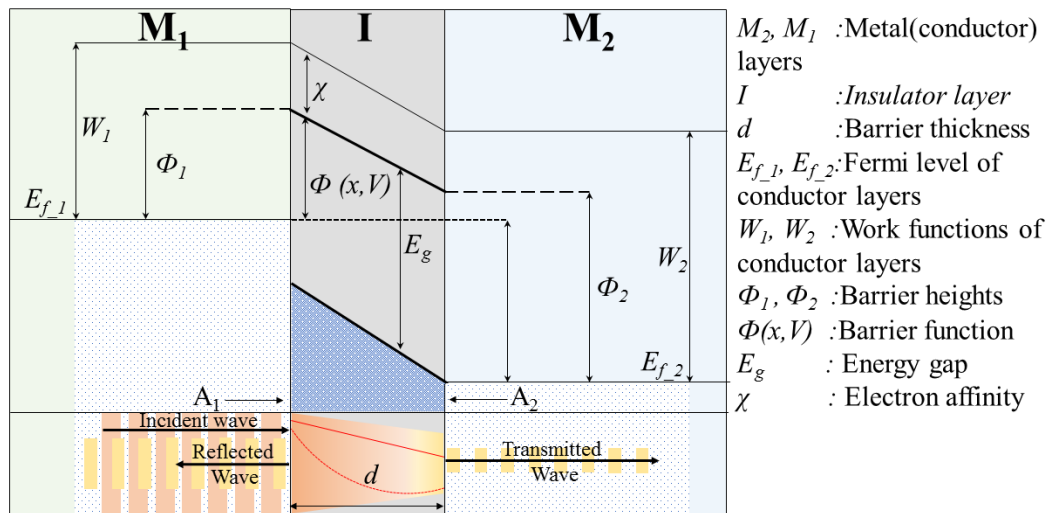


Figure 1.14 Sketch of tunneling process through a insulator layer between two metallic electrodes.

When the electrons are taken as wave function, there is a probability function of finding an electron of M_1 electrode behind the insulator barrier at M_2 . In other words, tunneling phenomena is the movement of an electron which occupies an available state at M_1 to unoccupied available state of M_2 . This occurrence is also net current of electron tunneling.

Wavefunction for electrons in tunnel junctions derived through Schrodinger equation [104]:

$$\left(\frac{p^2}{2m} + V\right)\psi = E\psi \quad \text{Equation 1.25}$$

Exponential decrease in the wave function of M_1 electrons through the barrier, however, it might outspread significantly beyond the barrier to M_2 electrode. Tunneling process may be divided in two main sections: Transmitted and reflected particles. Schrodinger equation solution for constant potential is in simple plane wave form:

$$\psi(x) = Ae^{\pm ikx} \quad \text{Equation 1.26}$$

$$k = \frac{2\pi}{\lambda} = \sqrt{\frac{2m(E-U)}{\hbar^2}} \quad \text{Equation 1.27}$$

If potential varies with position, x , Schrodinger's equation could be written in general form:

$$\psi(x) = Ae^{i\phi(x)} \quad \text{Equation 1.28}$$

where $\phi(x) = \pm kx$. $E > U$ and $E < U$ cases could be defined as:

$$\begin{cases} k(x) = \sqrt{\frac{2m(E-U)}{\hbar^2}}, & E > U(x) \\ k(x) = -i\sqrt{\frac{2m(E-U)}{\hbar^2}} = -i\kappa(x), & E < U(x) \end{cases} \quad \text{Equation 1.29}$$

To imply these phenomena in real-life events are given in barrier potential and energy of the incident particle. Solution of time-dependent Schrödinger's equation in one dimension is the following:

$$-\frac{\hbar^2}{2m} \frac{d^2\psi(x)}{dx^2} + U(x)\psi(x) = E\psi(x) \quad \text{Equation 1.30}$$

$$\Psi(x, t) = \psi(x) \exp\left(-i\frac{E}{\hbar}t\right) \quad \text{Equation 1.31}$$

where E is total energy of the particle, $U(x)$ the potential energy function and $\psi(x)$ is the spatial part of the full wavefunction. m is the mass of an electron and \hbar is the reduced

Planck's constant. Substitution of potential to the general solution results in the differential equation below:

$$i \frac{\partial^2 \phi}{\partial x^2} - \left(\frac{\partial \phi}{\partial x} \right)^2 + k^2(x) = 0 \quad \text{Equation 1.32}$$

Assumption of WKB approximation is starting from the idea that the variation in potential values in space is relatively slow. 0th order approximation:

$$\frac{\partial^2 \phi}{\partial x^2} = 0, \quad \frac{\partial \phi_0}{\partial x} = \pm k(x) \rightarrow \phi_0 = \pm \int k(x) dx + C_0 \quad \text{Equation 1.33}$$

$$\Psi(x) = \exp[\pm i \int k(x) dx + C_0] \quad \text{Equation 1.34}$$

and 1st order approximation:

$$\Psi(x) = \exp \left[\pm i \int \sqrt{k^2(x) \pm i \frac{\partial k}{\partial x}} dx + C_1 \right] \quad \text{Equation 1.35}$$

The shape of the potential has significant role on WKB approximation since:

$$U(x) \rightarrow k(x) \rightarrow \phi(x) \rightarrow \Psi(x) = \exp \left[\int \sqrt{k^2(x) \pm i \frac{\partial k}{\partial x}} dx + C_1 \right] \quad \text{Equation 1.36}$$

Among the several approximations, Simmons and Brinkman tunnel barrier models become prominent with simplified approach. Even if Simmons model [105, 106] disregards the data obtained from asymmetric barrier by taking the average of the barrier $\left(\frac{\phi_1 + \phi_2}{2} \right)$ (Fig. 1.15a), whereas Brinkman model [107] takes in consideration the asymmetric barrier by $\phi = \phi_2 - \phi_1$ (Fig. 1.15b).

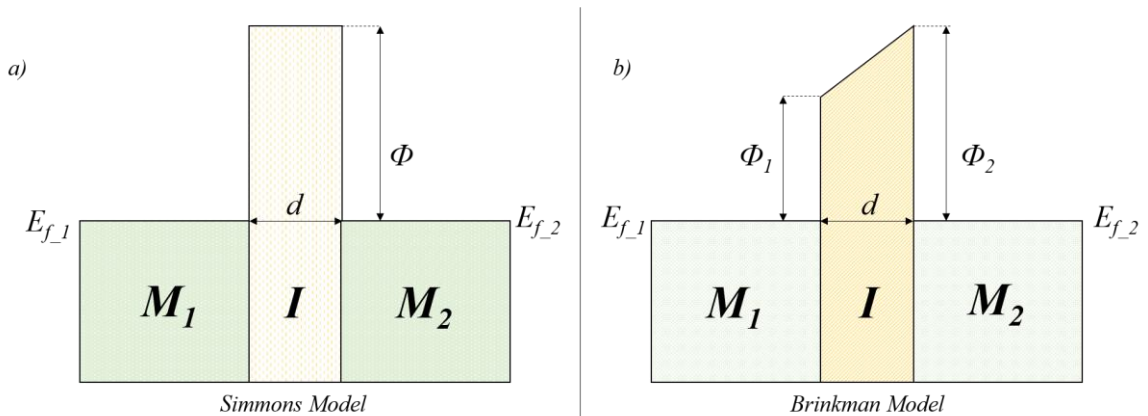


Figure 1.15 Simmons (a) and Brinkman(b) simplified model for tunneling

For the $\phi \gg eV$, and $\frac{\Delta\phi}{\phi} < 1$ condition, Brinkman model proposed the approximation:

$$j = \sim 3.16 \cdot 10^{10} \frac{\sqrt{\phi}}{d} \exp(-1.025 d\sqrt{\phi}) \dots$$

$$\left[V - 0.0213 \frac{d \cdot \Delta\phi}{\phi^{3/2}} V^2 + 0.0109 \frac{d^2}{\phi} V^3 \right] \quad \text{Equation 1.37}$$

These approximation is more accurate for thicker than 10 nm barriers. Rectangular barrier is quite limited condition where the symmetric interfaces surrounding the barrier. This approximation is given as:

$$j = \sim 3.16 \cdot 10^{10} \frac{\sqrt{\Phi}}{d} \exp(-1.025 d\sqrt{\Phi})$$

$$\left[V + 0.0109 \frac{d^2}{\Phi} V^3 - 0.032 \frac{d}{\Phi^{3/2}} V^3 \right] \quad \text{Equation 1.38}$$

Tunneling through asymmetric barrier with thickness $d=2a$ is taken as one-dimensional and the boundary conditions are defined as:

$$\phi = \begin{cases} 0 & x < -a; \\ U_0 - a < x < a; \\ -U_1 & x > a; \end{cases} \quad \text{Equation 1.39}$$

Hence, the Schrodinger equations could be transformed into the form:

$$\begin{cases} -\frac{\hbar^2}{2m} \frac{d\psi(x)}{dx^2} = E\psi_1(x) & x < -a; \\ -\frac{\hbar^2}{2m} \frac{d\psi(x)}{dx^2} = (E - U_0)\psi_2(x) & -a < x < a; \\ -\frac{\hbar^2}{2m} \frac{d\psi(x)}{dx^2} = (E - U_1)\psi_3(x) & x > a; \end{cases} \quad \text{Equation 1.40}$$

and the these transformed equations are solved in the form:

$$\begin{cases} \psi_1(x) = Ae^{ik_1x} + Be^{-ik_1x} & x < -a; \\ \psi_2(x) = Ce^{ik_2x} + De^{-ik_2x} & -a < x < a; \\ \psi_3(x) = Fe^{ik_3x} + Ge^{-ik_3x} & x > a; \end{cases} \quad \text{Equation 1.41}$$

where A, B, C, D, F, G are arbitrary constants and $k_1 = \frac{\sqrt{2mE}}{\hbar}$, $k_2 = \frac{\sqrt{2m(E-U_0)}}{\hbar}$ and $k_3 = \frac{\sqrt{2m(U_1+E)}}{\hbar}$ inside the barrier. When the quantized particle has lower energy than potential

barrier ($E < U_0$), k_2 becomes imaginary and $\kappa = \frac{\sqrt{2m(U_0-E)}}{\hbar}$ becomes valid. Ae^{ik_1x} , Ce^{ik_2x} and Fe^{ik_3x} represent the waves travelling in the positive direction of x , while Be^{-ik_1x} , De^{-ik_2x} , and Ge^{-ik_3x} represent the negative direction for x axis. Following solution taking into account the approximation above is:

$$\begin{cases} \psi_1(x) = Ae^{ik_1x} + Be^{-ik_1x} & x < -a; \\ \psi_2(x) = Ce^{ik_2x} + De^{-ik_2x} & -a < x < a; \\ \psi_3(x) = Fe^{ik_3x} + Ge^{-ik_3x} & x > a; \end{cases} \quad \text{Equation 1.42}$$

At the boundaries where $\psi(x)$ and its first derivative is continuous; the wavefunctions match and in the $x = -a$ condition:

$$Ae^{-ik_1a} + Be^{ik_1a} = Ce^{-\kappa a} + De^{\kappa a} \quad \text{Equation 1.43}$$

$$ik_1(Ae^{-ik_1a} - Be^{ik_1a}) = \kappa(Ce^{-\kappa a} - De^{\kappa a}) \quad \text{Equation 1.44}$$

For $x = a$ boundary condition;

$$Ce^{\kappa a} + De^{-\kappa a} = \beta'e^{ik_3a} + \beta e^{-ik_3a} \quad \text{Equation 1.45}$$

$$\kappa Ce^{-\kappa a} - \kappa De^{\kappa a} = ik_3(Fe^{ik_3a} + Ge^{-ik_3a}) \quad \text{Equation 1.46}$$

When the Eq.1.43 and 1.44 is multiplied by ik_1 and κ related with Eq.1.47 and Eq.1.48 respectively., dependencies of A and B on C and D could be seen:

$$2ik_1Ae^{-ik_1a} = Ce^{-\kappa a}(ik_1 + \kappa) + De^{\kappa a}(ik_1 - \kappa) \quad \text{Equation 1.47}$$

$$2ik_1Be^{-ik_1a} = Ce^{-\kappa a}(ik_1 - \kappa) + De^{\kappa a}(ik_1 + \kappa) \quad \text{Equation 1.48}$$

$$2\kappa Ce^{\kappa a} = Fe^{ik_3a}(\kappa + ik_3) + Ge^{-ik_3a}(\kappa - ik_3) \quad \text{Equation 1.49}$$

$$2\kappa De^{-\kappa a} = Fe^{ik_3a}(\kappa - ik_3) + Ge^{-ik_3a}(\kappa + ik_3) \quad \text{Equation 1.50}$$

Relation between $A - G$ and B is determined by transfer matrix method.:

$$\begin{pmatrix} A \\ B \end{pmatrix} = M \begin{pmatrix} C \\ D \end{pmatrix} = \begin{pmatrix} M_{11} & M_{12} \\ M_{21} & M_{22} \end{pmatrix} \begin{pmatrix} C \\ D \end{pmatrix} \quad \text{Equation 1.51}$$

where

$$M_{11} = \frac{1}{4} \left[i \left(\frac{\kappa}{k_1} + \frac{k_3}{\kappa} \right) (e^{2\kappa a} - e^{-2\kappa a}) + \left(1 + \frac{k_3}{k_1} \right) (e^{2\kappa a} + e^{-2\kappa a}) \right] \dots$$

$$e^{-i(k_1+k_3)a} = M_{22}^* \quad \text{Equation 1.52}$$

$$M_{12} = \frac{1}{4} \left[i \left(\frac{\kappa}{k_1} + \frac{k_3}{\kappa} \right) (e^{2\kappa\alpha} - e^{-2\kappa\alpha}) + \left(1 - \frac{k_3}{k_1} \right) (e^{2\kappa\alpha} + e^{-2\kappa\alpha}) \right] \dots$$

$$e^{i(k_1-k_3)\alpha} = M_{21}^* \quad \text{Equation 1.53}$$

Hyperbolic functions are injected into Eq.1.52 and 1.53 as $\frac{\sinh(2\kappa\alpha) = (e^{2\kappa\alpha} - e^{-2\kappa\alpha})}{2}$ and $\cosh(2\kappa\alpha) = \frac{(e^{2\kappa\alpha} + e^{-2\kappa\alpha})}{2}$:

$$M_{11} = \frac{1}{2} \left[i \left(\frac{\kappa}{k_1} + \frac{k_3}{\kappa} \right) \sinh(2\kappa\alpha) + \left(1 + \frac{k_3}{k_1} \right) \cosh(2\kappa\alpha) \right] e^{-i(k_1+k_3)\alpha} \quad \text{Equation 1.54}$$

$$M_{12} = \frac{1}{2} \left[i \left(\frac{\kappa}{k_1} + \frac{k_3}{\kappa} \right) \sinh(2\kappa\alpha) + \left(1 - \frac{k_3}{k_1} \right) \cosh(2\kappa\alpha) \right] e^{-i(k_1-k_3)\alpha} \quad \text{Equation 1.55}$$

The transmission and reflection coefficients of the tunneling is the following:

$$T = \frac{|G|^2}{|A|^2} = \frac{4 \frac{k_3}{k_1}}{\left(\frac{\kappa}{k_1} + \frac{k_3}{\kappa} \right)^2 \sinh^2(2\kappa\alpha) + \left(1 - \frac{k_3}{k_1} \right)^2 \cosh^2(2\kappa\alpha) + 4 \frac{k_3}{k_1}} \quad \text{Equation 1.56}$$

$$R = \frac{|B|^2}{|A|^2} = \frac{\left(\frac{\kappa}{k_1} + \frac{k_3}{\kappa} \right)^2 \sinh^2(2\kappa\alpha) + \left(1 - \frac{k_3}{k_1} \right)^2 \cosh^2(2\kappa\alpha)}{\left(\frac{\kappa}{k_1} + \frac{k_3}{\kappa} \right)^2 \sinh^2(2\kappa\alpha) + \left(1 - \frac{k_3}{k_1} \right)^2 \cosh^2(2\kappa\alpha) + 4 \frac{k_3}{k_1}} \quad \text{Equation 1.57}$$

For high and relative width barriers ($2\kappa\alpha \gg 1$), transmission coefficient is demeaned to:

$$T \propto \exp(-2\kappa\alpha) \propto \exp\left(-2 \frac{\sqrt{2m(U_0-E)}}{\hbar} a\right) \quad \text{Equation 1.58}$$

Eq.1.58 also indicates that the transmission shows logarithmic decrease with the barrier thickness and mass of the particles. Tunneling currents are determined by the barrier height and therefore the electrostatic potential has to be found using the Maxwell equations. In a ferroelectric sandwiched between metallic electrodes, the Maxwell equation:

$$\nabla \cdot D = \rho \quad \text{Equation 1.59}$$

has to be satisfied at every point under any given boundary condition. Here ρ is the charge density and \vec{D} is the dielectric displacement vector. Eq. 1.59 holds inside the FM and for an ideal, insulating FE, $\rho = 0$ and thus $\nabla \cdot D = 0$ in the ferroelectric. Due to the symmetry

of the stack along the plane, we reduce the problem into 2 dimensions as shown in Fig. 1.29. We can thus write \vec{D} as

$$\vec{D} = [D_x \hat{x} + D_z \hat{z}] \quad \text{Equation 1.60}$$

where

$$D_x = \varepsilon_0 \varepsilon_b E_x + P_x \text{ and } D_z = \varepsilon_0 \varepsilon_b E_z + P_z \quad \text{Equation 1.61}$$

in the FE layer with x and z denoting the in-plane and out-of-plane components respectively and,

$$D_x = \varepsilon_0 \varepsilon_r E_x \text{ and } D_z = \varepsilon_0 \varepsilon_r E_z \quad \text{Equation 1.62}$$

in the FM electrodes having a lattice dielectric constant of ε_r taken as 10. In Eqs. 1.61-1.62, ε_0 is the permittivity of the vacuum and ε_b is the background dielectric constant of the FE (10 in this work [108, 109]), E_x and E_z are respectively the x - and z - components of the electric field vector \vec{E} that can be determined from $E_x = -\frac{\partial \phi}{\partial x}$ and $E_z = -\frac{\partial \phi}{\partial z}$ with ϕ being the electrostatic scalar potential, P_x and P_z are the FE polarization components along x - and z -axes respectively. Eq. 1.59 and Eq. 1.60 is discretized below:

$$\frac{dD_x}{dx} + \frac{dD_z}{dz} = \rho \quad \text{Equation 1.63}$$

$$\frac{\partial}{\partial x} \left(-\varepsilon_0 \varepsilon_r \frac{\partial \phi}{\partial x} + P_x \right) + \frac{\partial}{\partial z} \left(-\varepsilon_0 \varepsilon_r \frac{\partial \phi}{\partial z} + P_z \right) \quad \text{Equation 1.64}$$

$$\varepsilon_0 \left(\frac{\partial \varepsilon_r}{\partial x} \frac{\partial \phi}{\partial x} + \varepsilon_r \frac{\partial^2 \phi}{\partial x^2} - \frac{\partial P_x}{\partial x} \right) - \varepsilon_0 \left(\frac{\partial \varepsilon_r}{\partial z} \frac{\partial \phi}{\partial z} + \varepsilon_r \frac{\partial^2 \phi}{\partial z^2} - \frac{\partial P_z}{\partial z} \right) = \rho \quad \text{Equation 1.65}$$

$$\frac{\partial \varepsilon_r}{\partial x} \frac{\partial \phi}{\partial x} + \varepsilon_r \frac{\partial^2 \phi}{\partial x^2} + \frac{\partial \varepsilon_r}{\partial z} \frac{\partial \phi}{\partial z} + \varepsilon_r \frac{\partial^2 \phi}{\partial z^2} = \frac{\rho}{\varepsilon_0} \frac{\partial P_x}{\partial x \varepsilon_0} + \frac{\partial P_z}{\partial z \varepsilon_0} \quad \text{Equation 1.66}$$

$$\varepsilon_r \left(\frac{\partial^2 \phi}{\partial x^2} + \frac{\partial^2 \phi}{\partial z^2} \right) = -\frac{\rho}{\varepsilon_0} + \frac{\partial P_z}{\partial z \varepsilon_0} + \frac{\partial P_x}{\partial x \varepsilon_0} - \frac{\partial \varepsilon_r}{\partial x} \frac{\partial \phi}{\partial x} - \frac{\partial \varepsilon_r}{\partial z} \frac{\partial \phi}{\partial z} \quad \text{Equation 1.67}$$

$$\left(\frac{\partial^2 \phi}{\partial x^2} + \frac{\partial^2 \phi}{\partial z^2} \right) = -\frac{\rho}{\varepsilon_0 \varepsilon_r} + \frac{1}{\varepsilon_0 \varepsilon_r} \left(\frac{\partial P_x}{\partial x} + \frac{\partial P_z}{\partial z} \right) - \frac{1}{\varepsilon_r} \left(\frac{\partial \varepsilon_r}{\partial x} \frac{\partial \phi}{\partial x} \right) - \frac{1}{\varepsilon_r} \left(\frac{\partial \varepsilon_r}{\partial z} \frac{\partial \phi}{\partial z} \right) \quad \text{Equation 1.68}$$

$$\left(\frac{\partial^2 \phi}{\partial x^2} + \frac{\partial^2 \phi}{\partial z^2} \right) - \frac{1}{\varepsilon_0 \varepsilon_r} \left(\frac{\partial P_x}{\partial x} + \frac{\partial P_z}{\partial z} \right) + \frac{1}{\varepsilon_r} \left(\frac{\partial \varepsilon_r}{\partial x} \frac{\partial \phi}{\partial x} \right) + \frac{1}{\varepsilon_r} \left(\frac{\partial \varepsilon_r}{\partial z} \frac{\partial \phi}{\partial z} \right) = -\frac{\rho}{\varepsilon_0 \varepsilon_r} \quad \text{Equation 1.69}$$

To find potential value from the set of equations, Eq.1.69 is organized as given below:

$$\begin{aligned} & \frac{\phi(i+1,j)-2\phi(i,j)+\phi(i-1,j)}{\partial x^2} + \frac{\phi(i,j+1)-2\phi(i,j)+\phi(i,j-1)}{\partial z^2} - \frac{1}{\varepsilon_0 \varepsilon_r(i,j)} \left[\left(\frac{P_{x(i+1,j)} - P_{x(i-1,j)}}{\partial x} \right) + \right. \\ & \left. \left(\frac{P_{z(i,j+1)} - P_{z(i,j-1)}}{\partial z} \right) \right] + \frac{1}{\varepsilon_r(i,j)} \left[\left(\frac{\varepsilon_r(i+1,j) - \varepsilon_r(i-1,j)}{\partial x} \right) \left(\frac{\phi(i+1,j) - \phi(i-1,j)}{\partial x} \right) + \right. \\ & \left. \left(\frac{\varepsilon_r(i,j+1) - \varepsilon_r(i,j-1)}{\partial z} \right) \left(\frac{\phi(i,j+1) - \phi(i,j-1)}{\partial z} \right) \right] = - \frac{\rho}{\varepsilon_0 \varepsilon_r(i,j)} \end{aligned} \quad \text{Equation 1.70}$$

$$\begin{aligned} \phi(i,j) = & \left(-\frac{\partial x^2}{4} \right) \left[-\frac{\rho}{\varepsilon_0 \varepsilon_r(i,j)} + \frac{1}{\varepsilon_0 \varepsilon_r(i,j)} \left[\left(\frac{P_{x(i+1,j)} - P_{x(i-1,j)}}{\partial x} \right) + \left(\frac{P_{z(i,j+1)} - P_{z(i,j-1)}}{\partial z} \right) \right] - \right. \\ & \left. \frac{1}{\varepsilon_r(i,j)} \left[\left(\frac{\varepsilon_r(i+1,j) - \varepsilon_r(i-1,j)}{\partial x} \right) \left(\frac{\phi(i+1,j) - \phi(i-1,j)}{\partial x} \right) + \left(\frac{\varepsilon_r(i,j+1) - \varepsilon_r(i,j-1)}{\partial z} \right) \left(\frac{\phi(i,j+1) - \phi(i,j-1)}{\partial z} \right) \right] + \right. \\ & \left. \frac{1}{4} \left(\frac{\phi(i+1,j) + \phi(i-1,j)}{\partial x^2} + \frac{\phi(i,j+1) + \phi(i,j-1)}{\partial z^2} \right) \right] \end{aligned} \quad \text{Equation 1.71}$$

Here, relaxation or (iterative finite difference) approach connected to the variational method to the problem brings robustness and monotonic approach to solution.

Electrostatic potential as given above, $E_x = -\frac{\partial \phi}{\partial x}$ and $E_z = -\frac{\partial \phi}{\partial z}$. The Gauss's Law determines the electric field where the equation turns into Laplace's equation:

$$\frac{\partial^2 \phi}{\partial x^2} + \frac{\partial^2 \phi}{\partial z^2} = \nabla^2 \phi = 0 \quad \text{Equation 1.72}$$

where it means that the concavity of $\phi(x,z)$ function move upwards along the given direction, this expansion is compensated by opposite direction concavity. As known, numerical solution of Laplace equation in two-dimension electrostatic potential utilizes non-zero dx and dz second derivatives. Symmetric evaluation of the function starts with the first derivative where:

$$\frac{\partial \phi}{\partial x} \approx \frac{\phi(x+\frac{1}{2}\partial x) - \phi(x-\frac{1}{2}\partial x)}{\partial x} \quad \text{Equation 1.73}$$

$$\frac{\partial \phi}{\partial z} \approx \frac{\phi(x+\frac{1}{2}\partial z) - \phi(x-\frac{1}{2}\partial z)}{\partial z} \quad \text{Equation 1.74}$$

$$\frac{\partial^2 \phi}{\partial x^2} \approx \frac{\phi(x+\partial x) - \phi(x-\partial x) - 2\phi(x)}{\partial x^2} \quad \text{Equation 1.75}$$

$$\frac{\partial^2 \phi}{\partial z^2} \approx \frac{\phi(z+\partial z) - \phi(z-\partial z) - 2\phi(z)}{\partial z^2} \quad \text{Equation 1.76}$$

By plugging the both results evaluated as square and cross form from Eq.1.71 and Eq. 1.72 in the $\phi(x, z)$:

$$\phi_{cross}(x, z) = \frac{\phi(x+\partial x, z) + \phi(x-\partial x, z) + \phi(x, z+\partial z) + \phi(x, z-\partial z)}{4} \quad \text{Equation 1.77}$$

$$\phi_{square}(x, z) = \frac{\phi(x+\partial x, z+\partial z) + \phi(x-\partial x, z-\partial z) + \phi(x-\partial x, z+\partial z) + \phi(x+\partial x, z-\partial z)}{4} \quad \text{Equation 1.78}$$

In any point, using Eq.1.63, average potential of the adjacent sites is obtained.

Averaging of the electrostatic scalar potential could be inadequate to comprehend, so that, instead averaging values at the cross points of the given integers, square of the given integers substituted by particular weighted Taylor expansion where[110] :

$$f(x)_{average} = \frac{4}{5} \phi_{cross}(x, z) + \frac{1}{5} \phi_{square}(x, z) \quad \text{Equation 1.79}$$

ρ is the spatial total charge density and consists of electrons and ionized ions that donate these electrons in the electrode:

$$\rho = q(-n^- + p^+ + N_D^+) \quad \text{Equation 1.80}$$

1.2.1.1 Homogeneous polarization approximation

In the course of the work, we noticed that there are additional complications that arises from possible inhomogeneities in the ferroelectric polarization of the tunnel junction. To be able to provide an overall view of the connection between the magnetoelectric coupling occurring due to spin dependent screening and polarization strength, we first assume a linear connection between the electric field and a uniaxial polarization inside the ferroelectric layer via

$$D_z = \epsilon_o \epsilon_b E_z + P_z \text{ and } \text{div} D_z = 0 \quad \text{Equation 1.81}$$

where we assign the polarization any value between -0.3 and 0.3 C/m² that are well within the range of the zero field calculated values for homogeneously strained thin FE films between electrodes. Note that these values might or might not correspond to equilibrium (hence we call is “imposed” or “non-equilibrium” polarization) and a homogeneous profile of polarization across the film thickness is supposed. Despite this, the relevant

depolarizing field effects and their connection with the spin dependent screening under any bias value can be calculated: one only needs to solve the electric field, E_z everywhere inside the FM electrodes and FE. This assumption is valid for the bias duration being much less than polarization relaxation of the FE. Inside the FM electrodes, Eqs. 1.59 and 1.62 hold. To demonstrate a TJ with a linear dielectric, one only needs to drop the P_z term in Eq. 1.62 and replace ϵ_b with ϵ_r , namely the relative dielectric constant of the dielectric. We skip the case of a dielectric TJ as this is well understood since 1990s where a relatively weak dependence on the dielectric constant of the TJ is expected. On the other hand, the reported bias dependence of the TMR behavior of dielectric TJs are somewhat parallel with that of a FE TJ as we shall show here with the difference that the latter has much greater on/off current ratios.

1.2.1.2 Polarization obtained from thermodynamic equation of state

While the electric field is connected to the dielectric properties of the electrodes and FE via Eqs. 1.59 (for $\rho = 0$) and 1.61., Landau-Ginzburg Eqs. of state for polarization also have to be solved in the FE layer:

$$2\alpha_3^m P_z + 4\alpha_{13}^m P_z P_x^2 + 4\alpha_{33}^m P_z^3 + 6\alpha_{111} P_z^5 + \alpha_{112} (4P_z P_x^4 + 8P_z^3 P_x^2) + 2\alpha_{123} P_z P_x^4 - G \left(\frac{\partial^2 P_z}{\partial z^2} + \frac{\partial^2 P_z}{\partial x^2} \right) = -\frac{\partial \phi}{\partial z} \quad \text{Equation 1.82}$$

$$2\alpha_1^m P_x + 2(2\alpha_{11}^m + \alpha_{12}^m) P_x^3 + 2\alpha_{13}^m P_x P_z^2 + 6\alpha_{111} P_x^5 + 2\alpha_{112} [3P_x^5 + 3P_x^3 P_z^2 + P_x P_z^4] + 2\alpha_{123} P_x^3 P_z^2 - G \left(\frac{\partial^2 P_x}{\partial z^2} + \frac{\partial^2 P_x}{\partial x^2} \right) = -\frac{\partial \phi}{\partial x} \quad \text{Equation 1.83}$$

and simultaneously satisfy Eq. 1 when $\rho = 0$. To avoid any a priori assumptions on the direction of FE polarization, we considered an in-plane component of polarization, P_x in addition to the out-of-plane component due to size effects and possibility of domain formation in the TJ. We, however, find a single domain uniaxial state that has been demonstrated in experiments focusing on tunnelling resistance. Note that thermodynamic stabilization of a single domain state in ultrathin FE layers can be expected due to the energy cost of the domain wall formation in such structures that was even reported in ferroelectric/paraelectric superlattices [89, 90, 111]. Hence, for sufficient compressive strains ($> -1\%$ or more here), one can safely eliminate the component P_x in Eqs. 1.82 and

1.83 and solve it only for P_z in the limit of uniaxial FE polarization. In Eqs. 1.82 and 1.83 α_3^m , α_{13}^m , α_{33}^m , α_1^m , α_{11}^m , α_{12}^m , are the renormalized phenomenological thermodynamic coefficients [102] in SI units with α_1^m and α_3^m being $\alpha_1^m = \alpha(T - T_c) - u_{ij}^M(Q_{11} + Q_{12})/(S_{11} + S_{12})$ and $\alpha_3^m = \alpha(T - T_c) - 2u_{ij}^M Q_{12}/(S_{11} + S_{12})$ due to renormalization with misfit strain where $\alpha = (2\varepsilon_0 C)^{-1}$, α_{12}^m and α_{33}^m contain the clamping effect of the film, while α_{111} , α_{112} , α_{123} are the dielectric stiffness coefficients in the bulk, u_{ij}^M is the misfit strain tensor for a cubic structure and is taken here either as -1.25% or -1.5% (negative here meaning compression) that keeps the FE polarization along the normal of the stack plane. The two different misfit values produce different polarization amplitudes allowing us to study the effect of this parameter on spin polarization of the tunneling currents. In Eqs. 1.82 and 1.83, G is the gradient energy coefficient and is assumed to be isotropic for convenience. All the phenomenological coefficients used in the thermodynamic calculations are for BT and are compiled from Ref. [102]. The polarization boundary conditions at the LHS and RHS interfaces are important as previously discussed [112, 113] and can be expressed as

$$\left[P_z + \lambda \frac{dP_z}{dz} \right]_{z=\frac{FM}{FE} \frac{FE}{FM}} = 0, \quad \left[P_x + \lambda \frac{dP_x}{dz} \right]_{z=\frac{FM}{FE} \frac{FE}{FM}} = 0 \quad \text{Equation 1.84}$$

with z indicating the coordinates for left FM/FE and right FE/FM interfaces, λ is the extrapolation length determining the extent of the change of polarization along the film normal at the interface and is a parameter implying how polarization terminates at the interfaces (taken as 3 nm here based on previous reports [114]).

Table 1.2:Material parameters and thermodynamic coefficients for BTO and STO used in the calculations[102]

Parameters	SrTiO ₃	BaTiO ₃
Lattice parameter (nm)	0.3904	0.4004
T_C (°C)	-250	130
C (10^5 °C)	8×10^5	1.5×10^5
α_{11} ($N m^6/C^4$)	6.8×10^9	$3.6 \times (T-175) \times 10^8$
α_{12} ($N m^6/C^4$)	2.74×10^9	-0.0345×10^8
α_{111} ($N m^{10}/C^6$)	0	6.6×10^9
α_{112} ($N m^{10}/C^6$)	0	18.14×10^8
α_{123} ($N m^{10}/C^6$)	0	-7.45×10^9
S_{11} ($10^{-12} N/m^2$)	5.546	8.3
S_{12} ($10^{-12} N/m^2$)	-1.562	-2.7
S_{44} ($10^{-12} N/m^2$)	9.24	9.24
Q_{11} (m^4/C^2)	0.0457	0.11
Q_{12} (m^4/C^2)	-0.0135	-0.043
Q_{44} (m^4/C^2)	0.00975	5.165×10^{-2}
g ($10^{-10} J m^3/C^2$)	6	6
N_V, N_C	$10^{25}, 10^{25}$	$10^{25}, 10^{25}$
E_V, E_C, E_D (eV)	-7.1, -3.9, -4.0	-6.72, -4.0, -4.1

1.2.2 Resistive Switching in Metal/Ferroelectric/Semiconductor Junctions

The destructive read-out (DRO) FeRAM devices utilizes ferroelectric layer as capacitor incorporating into complementary metal-oxide-semiconductor transistor. CMOS transistor isolates each memory cell, to distinguish individually as bits. Data storage is read as charge where the polarization direction of the ferroelectric in the capacitor. When the data is read DRO, polarization state is changed from positive to negative remnant polarization or vice versa. Every data reading process must restore the polarization state whereas in the non-destructive (NDRO) architecture; ferroelectric layers work as gate material in the transistor, thus no additional capacitor elements is added to the circuitry. Data is read through the surface conductivity of the silicon which is controlled by the remnant polarization of the ferroelectric layer. Differing from the DRO FeRAM devices, readout process does not create fatigue problems in NDRO devices.

Due to its simple structure, low switching voltage (RRAM) stands out due to its simple structure, low switching voltage, fast switching speed, stability and CMOS compatibility, resistive switching memory became prominent candidate among various emerging

memory technologies[115, 116]. Resistive switching is an physical phenomena where the resistance changes of the material under external electric field. One of the featured property of this process is that the resistive switching is reversible and repeatability.

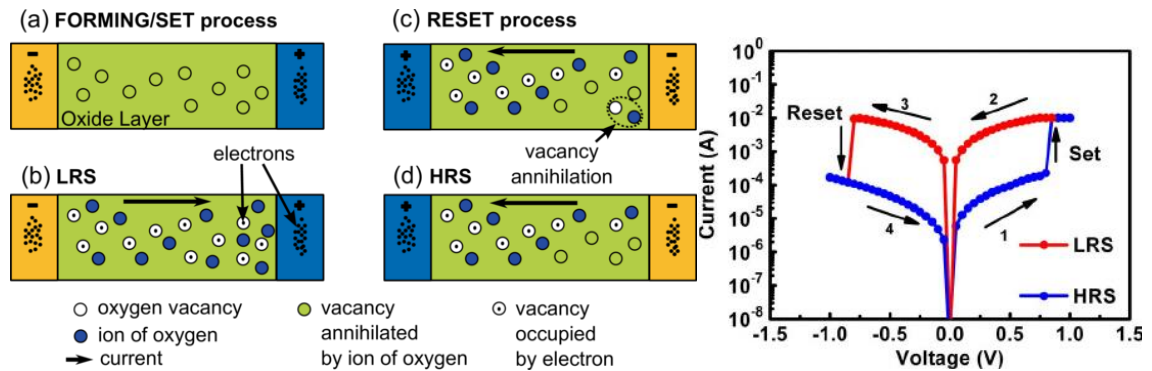


Figure 1.16 a-d) Resistive switching is shown in electronic level. e) I-V curve for resistive switching junctions. It shows resistance changes where the voltage is applied to the junction, current flow increases up to limit to set the area which is called LRS, when voltage is swept through the system, junction first goes “RESET, then HRS state.

Resistive switching memory devices consist of electrode/oxide/electrode. Switching from high resistance state (HRS) to low resistance state (LRS) is known as “SET” (1). Reversing the resistance state from low to high is called as “RESET” (3). Switching modes could be generalized into two switching modes: unipolar and bipolar. In unipolar mode; switching occurs at same polarity (SET/RESET), whereas in bipolar switching, SET can be observed in one polarity and RESET in the other (Fig.1.16)

Unipolar mode is acquired with noble metals such as Pt, Ru as both electrode sides. If the system is composed of oxides, charge traps and oxygen vacancy migration activated through the external electric field.

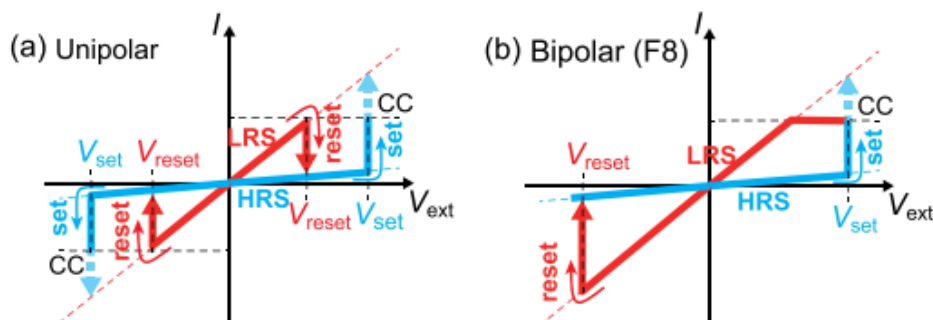


Figure 1.17 Unipolar and bipolar resistive switching [117]

We also reported results on the variation of Schottky effect in sol-gel processed $\text{Ba}_{1-x}\text{Sr}_x\text{TiO}_3$ films (BST, $x = 0, 0.5$) grown on 0.5% Nb doped SrTiO_3 semiconductor substrates with top Pt electrodes (NSTO/BST/Pt) [118]. I-V measurements has also showed magnitude of the leakage and hystereses depending on the Sr concentration in BaTiO_3 films. It was also emphasized on the current-voltage (I-V) characteristics of our samples in the context of thermodynamic theory of ferroelectrics coupled with equations of semiconductors. Our calculations give rise to unambiguously determine the electronic character of the defects and related band bending effects in BT and BST samples. Amplitude of the ferroelectric polarization, which is a function of strontium content in BT, has a strong impact on leakage currents in forward bias while this effect is much weaker under negative bias. In the case of polarization pointing away from NSTO semiconducting substrate, carriers are being depleted at the NSTO interface which increases the resistance through the stack (Fig. 1.18). Such condition also generates larger energy gap between the Fermi level and the conduction bands of the films, thus reducing the bulk conduction through the film as well Leakage currents in thicker ferroelectric films also shows significant symptoms of NDRO depending on the polarization direction.

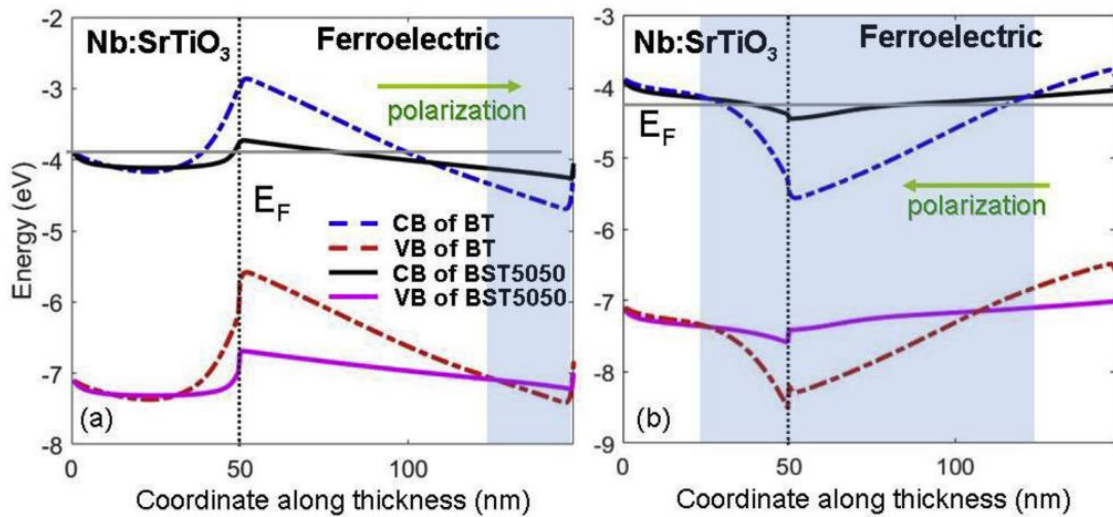


Figure 1.18 Computational flat-band results obtained from thermodynamic theory for a) BT and BST 5050 under 0 V bias and b) when under 0.5 V bias. Notice how the CB of BT “submerges” into the Fermi level (E_F) under 0.5 V for this composition (under positive bias). The shaded regions indicate the locations of free electron accumulation. The green arrow in (a) and (b) indicates the direction of polarization. BST 5050 is only slightly influenced by the positive bias with lower conduction currents expected than that

of in BT as also observed in experiments. Also note that the energy scales are different in (a) and (b) due the amount of band bending being different in both plots.

(CB: Conduction band, VB: Valence band.)

High quality sol-gel grown BT and $\text{Ba}_{0.5}\text{Sr}_{0.5}\text{TiO}_3$ thin film samples is discussed the switchable Schottky effect that is accompanied by resistive switching using experimental and theoretical methods. Analysis of the experimental data in light of the thermodynamic simulations where the FE films are treated as wide bandgap semiconductors explain the asymmetry in the I-V curves and the current hystereses observed under positive bias that is a function of Sr composition. Thermodynamic calculations show that the conductivity of the films under the positive bias will be bulk limited and a strong function of the “polarization strength”, that is determined here mostly by the Sr content of the film. In addition to the experimental work mentioned above, under positive bias, various leakage measures for BT and BST films is also approved by thermodynamic theory approximation. The depth of charge depleted and accumulated regions in NSTO substrates directly correlated to the ferroelectric polarization strength. Moreover, hysteresis in I-V plots reveals that the effect of the stronger polarization of BT than in BST50.

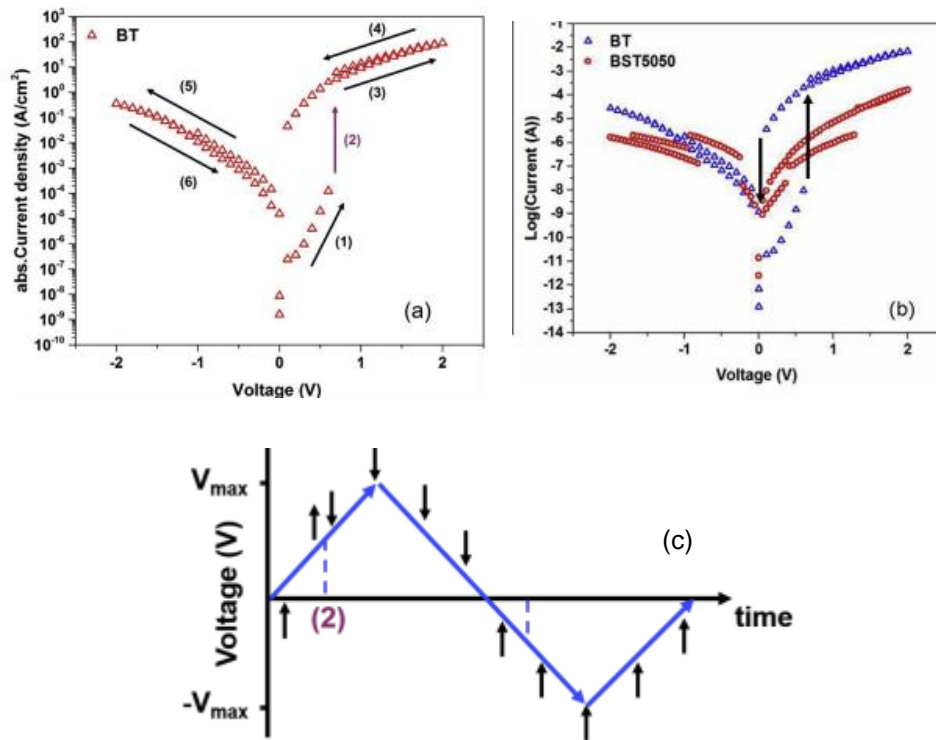


Figure 1.19 (a) Plot indicates the switching in high and low resistance states. (1) and (4) correspond to high-resistance and low resistance states respectively during the positive up-sweep and down-sweep. Switching from “up polarization” to “down polarization” occurs at (2). Almost no hysteresis occurs during (5) and (6) as polarization direction in the negative bias is fixed according to our thermodynamic calculation results. b) I-V quasi-static measurements in BT and BST 5050 films. Notice the hystereses in the positive bias regime of the BT. The up arrow indicates the jump in conductivity at the bias when polarization switches and starts pointing towards the NSTO interface while applying positive bias to top electrode. The arrow pointing down near zero bias indicates diminishing current while approaching zero bias after the max positive bias was already applied. (c) Schematic to demonstrate the direction of polarizations deduced from the experiments and thermodynamic calculations. Black arrow simply the polarization direction during the triangular bias-sweep (blue arrows). The vertical blue dashed lines denote the bias values where switching occurs during the sweep. Switching from “down polarization” to “up polarization” occurs at 2 as indicated in (a).

As polarization pointing away from NSTO surface (negative bias), space-charge region in NSTO is depleted where the leakage values are apparently low. Polarization strength also controls the conduction where the band-bending and carrier concentration in the

conduction band of FE films and bulk conduction. When the direction of ferroelectric polarization pointing towards the NSTO, and away from Pt electrode (positive bias), NSTO is in accumulation state, bulk conductivity inside the film occurs when the conduction band of the films enter into the Fermi level. Finite penetration length of the electric field into electrode layers. Mechanism lying behind electric field penetration from FE layer is a prominent explanation for leakage, resistive switching and the hysteresis in I-V curves. Dynamic and quasi-static I-V measurements are supported the thermodynamic simulations. Ferroelectric phase stability directly affected by the defect sites such as inhomogeneities and local conductive areas in the thin films. The impact of local microstructural properties on the results was not directly related to the finding where the characteristics of interface of film/electrode was referred to electronic interactions. Our results also indicated that the resistive switching is not limited in tunnel junctions but also observed in thicker films.

Table 1.3 shows various experimental works with differing proposed mechanism. In thicker films (>8 nm) where the quantum tunneling rapidly decays, bulk conductivity starts to dictate the system as long as the function of polarization direction based uncompensated charges at the FE/electrode interface exist.

Ferroelectric tunneling has been functionalized by replacing metal electrodes with ferromagnetic ones which transforms the junction into “composite multiferroic”[119, 120]. Previously mentioned, composite multiferroics have higher magnetoelectric coupling values than single-element multiferroics.

Table 1.3 Review of experimental results of tunneling resistance with FTJ

Substrate	Bottom Electrode	FE barrier/Thickness(nm)	Top electrode/ ϕ (μm)	OFF/ON	Specifications	Year	Ref.
STO	LSMO	PZT/9	Cu/0.22	>1500	Thermoionic injection	2011	[59]
NDGO	LSMO	BT/1.6	Co/5	1000	Memristor/oxygen vacancies	2012	[60]
NDGO	LSMO	BT/2	Co/0.35	>300	Memristor/FE domains correlation	2012	[62]
STO	LSMO	PZT/1.2-1.6	Co/0.22	300	FE domains	2012	[63]
NDGO	LSMO	BT/2	Co/0.50	>100	Fast: 10 ns	2012	[61]
DyScO ₃	SRO	BT	Ag/0.02	>100	Small: 20 nm	2012	[58]
STO	LSMO	BT/3	La _{0.5} Ca _{0.5} MnO ₃ /15	100@5 K	Metal/Insulator phase transition	2013	[52]
	SrTiO ₃ : Nb	BT/3.4	Pt/30	>10000	Barrier width modulation/SC electrode	2013	[67]
MgO	Pt	BT/3	Cr/0.80	30	Transport/potential profile	2013	[121]
YAIO ₃	Ca _{0.96} Ce _{0.04} MnO ₃	T-BFO/4.5	Co/0.18	>10000	FE domains/transport correlation	2013	[73]
STO	LSMO	BT/2.4	Graphene/10	>4000	Graphene top electrode	2014	[122]
YAIO ₃	Ca _{0.96} Ce _{0.04} MnO ₃	BFO/4.6	Co/100	4x10 ³	Highest cycle values	2014	[74]
STO	LSMO	BTO-2.0,2.6	Ru/0.13-2.3	20	Top electrode size/resistance correlation	2015	[123]
STO	LSMO	BTO-2-4	Pt/16.9	300		2015	[124]
LaAlO ₃	LaNiO ₃	T-BFO/10 u.c.	-	500	Highest TER values	2016	[76]
n-Si	SiO _x	Hf _{0.5} Zr _{0.5} O ₃	TiN	-	New type of material use	2016	[125]
STO	SRO/20	BTO/STO/4	(Ti/Au)/500	2000	Composite barrier	2017	[75]
STO	LSMO	BTO/4.4	LSMO	-	Tunneling through head-to-head domains	2017	[126]
n-Si	TiN	f _{0.5} Zr _{0.5} O ₂	Pt/300	1000	Integration to CMOS devices	2017	[127]

STO: SrTiO₃, BT: BaTiO₃, NDGO: NdGaO₃, LSMO: La_{2/3}Sr_{1/3}MnO₃, L6S4MO: La_{0.6}Sr_{0.4}MnO₃, BFO: BiFeO₃, LSAT: (LaAlO₃)_{0.3}(Sr₂TaAlO₆)_{0.7}, PZT: PbZr_{0.2}Ti_{0.8}O₃

1.3 Multiferroic Heterojunctions and Tunnel Junctions (MFTJ)

The interplay between magnetic and electric field was first observed by Roentgen [128] where a dielectric moving body under the influence of electric field has indicated magnetization.

Debye also pronounced “magnetoelectric” term in 1926 [129] and years after, generalized theory of continuous phase transitions of Landau which testifies that the ferroelectric order could occur under symmetry breaking operations via spin structure, in other words, coupling between electric polarization and magnetic order in time asymmetric media proposed by L. D. Landau and E. Lifshitz [130, 131]. Works of Dzyaloshinskii on magnetic symmetry showed that magnetoelectric effect could be experienced on antiferromagnetic Cr_2O_3 [132], which were followed by electric field induced magnetization and magnetic field induced electric polarization experiments [133, 134].

Ferroic [135, 136] term was first pronounced by Aizu but later on, correlatively refers for the crystals which have equivalent transition under proper external forces such as stress, magnetic or electric field. Under these external forces, domain structure of these crystals response as spontaneous deformation, magnetization, and polarization, respectively.

In fact, single phase multiferroics are known as a material that has more than one ferroic parameter as mentioned, ferroelectricity, ferromagnetism or ferroelasticity (Fig.1.20). In contrast, the magnetoelectric coupling may emerge from magnetic-electric field interaction of the material or mediately several combined order parameters such as magnetostriction or piezoelectricity as a product of strain.

Mechanism of ferroelectricity is contradictory with the magnetic order in materials where d shells must be half-filled whereas d shell of ferroelectrics is empty or full-filled where covalent bonding formation arise [137, 138]. A number of studies about multiferroics has been conducted in consideration of these inferences between the late 1950s to 1980s [139-141]. However; these efforts had only shown the scarcity of single phase magnetoelectric multiferroics. $\text{Ni}_3\text{B}_7\text{O}_{13}\text{I}$ was the first multiferroic compound which ferromagnetic and ferroelectric behavior was observed simultaneously [142]. Experimental and theoretical on new perovskite type compounds such as Tb based TbMnO_3 , TbMn_2O_5 [143, 144],

YMnO₃ [145] and Ni₃V₂O₈ [146] paved the way for ‘renaissance’ of the magnetoelectric multiferroics [147].

Nonetheless, several magnetoelectric multiferroic research pointed out that most of the compounds are active below room temperature which limits their utilization in device application. Discovery of the multiferroic BiFeO₃ and its growth as epitaxial thin films made this material the first single-phase multiferroic with one of the highest Curie (1100 K), Neel (650 K) temperatures [148]. Magnetoelectric response of BiFeO₃ is above average of previous multiferroic materials [148, 149]. Many groups have been spending much effort to shed light on the structure and theoretical understanding [150-159], experimental techniques [160-162], and future of BiFeO₃ but, magnetoelectric and ferroelectric responses of BiFeO₃ are inadequate for attributed spin-controlled or spintronic device and applications.

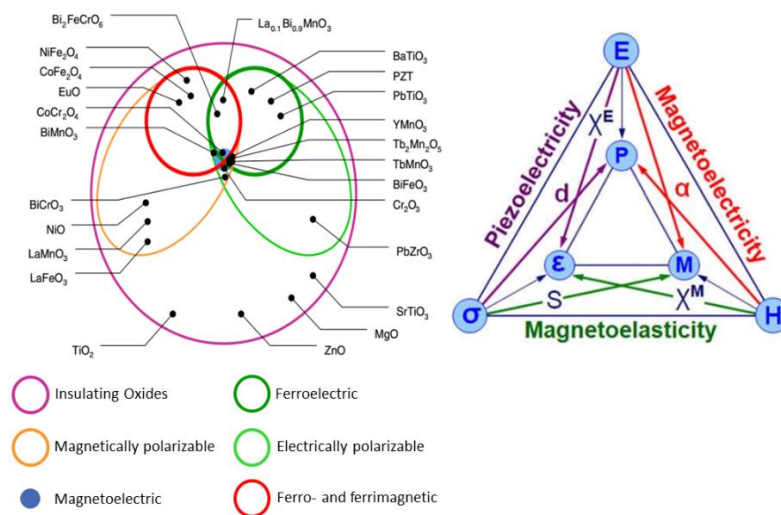


Figure 1.20 a) Classification of insulating oxides in the context of magnetic and electrical properties [163] and b) interaction in between stress, electric field, and magnetic field give rise to several coupling effects.[164]

Single-phase magnetoelectric multiferroics were categorized [165] as mainly Type I and Type II which are:

Type I Multiferroics: These elements of multiferroics are old members of ferroelectrics family. Critical transition temperatures of these materials are above room temperature and differ from each other which occurrence of both orders simultaneously beclouded,

therefore coupling between magnetic and ferroelectric order appears moderately weak. Type I multiferroics are parsed in three subclasses by ferroelectric ordering and mechanism:

- a. **Ferroelectricity due to lone pairs:** Cation located with differing valency at A site of this class (Bi^{3+} , Pb^{3+} , etc.) has 6s orbital electrons which are not bonded. They are called “lone pair”. These electrons are a source of ferroelectricity due to the capability to polarize the crystal. Another cation located at B site (Fe^{3+} , Mn^{3+} , Ni^{2+} , etc.) is a source of magnetism where d-shell of these transition metals are partially filled. Major examples of this subclass are BiFeO_3 , PbVO_3 , BiMnO_3 .
- b. **Ferroelectricity due to charge ordering:** Charge ordering occurs in $\text{Pr}_{0.5}\text{Ca}_{0.5}\text{MnO}_3$ [166-168], TbMn_2O_5 [143, 144] and RNiO_3 [169, 170] due to the variation in valence states of transition metal cations of given compositions. Inequivalent charge and bonding leads to ferroelectricity in this group of materials.
- c. **Geometric Ferroelectricity:** Imposed ferroelectricity is observed in manganite perovskites such as YMnO_3 due to the tilting in MnO_5 promotes closer packing and oxygen ions tilted to Y ions or displacement of Y ion. Hence, unequal charge distribution is concluded as dipole generation.

Type-II multiferroics: Magnetic multiferroics: Here, existence of ferroelectricity emerges due to magnetic ordering of the multiferroic compound which differs from Type-I multiferroics. Type II multiferroics can develop moderately low electric polarization under magnetic field. This group is divided into:

- a. **Spiral type-II multiferroics:** TbMnO_3 , $\text{Ni}_3\text{V}_2\text{O}_6$, and MnWO_4 are well-known members of this group where the ferroelectric order induced by spin-orbit coupling. Sinusoidal spin flop rotation through the spiral-shaped propagation provoke non-zero electric polarization lies perpendicular to the propagation of wave vector.
- b. **Collinear magnetic structures:** Ferroelectricity arises under magnetic moment alignment along the axis, by exchange striction, since intermediate oxygen distances due to different valences of transition metal and metal-oxygen bond

angles forms exchange striction. Magnetic ordering form inversion symmetry breaking behavior. Well-known example of collinear magnetic structure is $\text{Ca}_3\text{CoMnO}_6$ [171, 172].

1.3.1 Magnetolectric Coupling

Magnetolectric coupling term involves material polarization under magnetic field or magnetization under an electric field. L.D. Landau laid the theoretical foundations of magnetolectric coupling effect[130] in the context of free energy, F of a system where is represented as homogenous and stress-free under the external electric field, E and magnetic field, H which is

$$\begin{aligned} -F(E, H) = & \frac{1}{2} \epsilon_0 \epsilon_{ij} E_i E_j + \frac{1}{2} \mu_0 \mu_{ij} H_i H_j + \alpha_{ij} E_i H_j \\ & + \frac{\beta_{ijk}}{2} E_i H_j H_k + \frac{\gamma_{ijk}}{2} H_i E_j E_k + \dots \end{aligned} \quad \text{Equation 1.85}$$

where ϵ_0 is permittivity of vacuum and μ_0 is permeability of vacuum. ϵ_{ij} and μ_{ij} are relative dielectric constant and magnetic susceptibility, respectively. α_{ij} tensor corresponds to first order magnetolectric coupling coefficient where the electric polarization induced by a magnetic field or vice versa. β_{ijk} and γ_{ijk} tensors are quadratic magnetolectric coupling coefficients. H_i, H_j, H_k are denoted as components of applied magnetic field and applied electric field whose components are denoted as E_i, E_j, E_k . Derivative of the free energy with respect to electric field results in polarization, P ($\mu\text{C}/\text{cm}^2$)

$$P_i = -\frac{\partial F}{\partial E_i} \quad \text{Equation 1.86}$$

$$P_i = \alpha_{ij} H_j + \frac{\beta_{ijk}}{2} H_j H_k + \dots \quad \text{Equation 1.87}$$

A derivative of the free energy with respect to magnetic field results in magnetization, M (μ_B per formula unit (f.u.))

$$M_i = -\frac{\partial F}{\partial H_i} \quad \text{Equation 1.88}$$

$$\mu_0 M_i = \alpha_{ji} E_j + \frac{\gamma_{ijk}}{2} E_j E_k + \dots \quad \text{Equation 1.89}$$

Derivations are given above (Eq. 1.85-1.89) show the correlation and interaction between multiferroic, ferroelectric and ferromagnetic materials. Ferroic material responses to E and H indicate hysteretic behavior. By considering substantial depolarizing and demagnetizing field effect for ferroelectric and ferromagnetic materials respectively, coupling constants are function of temperature.

In the single phase multiferroics, magnetoelectric coupling coefficient, α_{ij} strongly coupled to dielectric constant and magnetic susceptibility[173]:

$$\alpha_{ij}^2 \leq \epsilon_0 \mu_0 \epsilon_{ii} \mu_{jj} \quad \text{Equation 1.90}$$

This equation (Eq.1.90) derived from Eq. 1.89 where first three terms are compelled to greater than zero value. One should notice that ϵ_{ij} and μ_{ij} are limiting factor on phase stability where drastic increase of the coupling value inclines more stable phase. New ϵ_{ij} , μ_{ij} and α_{ij} are assigned to the system according to the transformed phase. On the other hand, high order coupling constants β_{ijk} and γ_{ijk} have no restriction and in some cases linear term $\alpha_{ij}H_j$ could be dominated by $\beta_{ijk}H_jH_k$.

Non-zero α_{ij} values could be only obtained non-centrosymmetric and time-asymmetric materials. Symmetry elements are vital to elicit magnetoelectric behavior. One can simply be mistaken by presupposition of that all linear magnetoelectric term, $\alpha_{ij}E_iH_j$ containing magnetoelectric materials must be multiferroic. The reverse case is also true: All multiferroics does not have to be magnetoelectric. Linear magnetoelectric effect of BiFeO₃ converges to zero and only quadratic effect is active[174], or symmetry restraint on hexagonal REMnO₃ restricts linear magnetoelectric effect[175]. These materials are ferroelectric and have antiferromagnetic Mn³⁺ ion alignment at below Neel temperature.

Magnetoelectric responses of single phase multiferroics are inadequate for attributed spin-controlled or spintronic device and applications. This restriction led pursuit of enhancing magnetoelectric coupling via composite materials. Eq. 1.89 as limiting factor is boosted via two different optimized ferroelectric-ferromagnetic layers.

Magnetoelectric coupling in composite materials materialize in various interfacial mechanisms:

- a. Strain-mediated magnetoelectric coupling

b. Charge-mediated magnetoelectric coupling

c. Exchange bias mediated coupling

1.3.1.1 Strain-Mediated Magnetoelectric Coupling

Strain mediated coupling is product of magnetostrictive effect for magnetic medium and piezoelectric effect for piezoelectric media. Simply direct and converse magnetoelectric effect pronounced as follows[176]:

$$\text{Direct magnetoelectric effect } (\alpha_H) = \frac{\text{Magnetic}}{\text{Mechanical}} \times \frac{\text{Mechanical}}{\text{Electric}} \quad \text{Equation 1.91}$$

$$\text{Converse magnetoelectric effect } (\alpha_E) = \frac{\text{Electric}}{\text{Mechanical}} \times \frac{\text{Mechanical}}{\text{Magnetic}} \quad \text{Equation 1.92}$$

From Eq. 1.91 and 1.92 one can single out that large magnetoelectric coupling values could be reached by juxtaposing high electrostrictive and magnetostrictive materials. External electric field applied ferroelectric material with high electrostriction will alter its shape and transfer the strain to the high inverse magnetostrictive ferromagnetic surface which will change its magnetic anisotropy (Fig. 1.21). FeGaB/Pb(Zn_{1/3}Nb_{2/3})O₃-0.06 PbTiO₃(PZN-0.06PT)[177], Ni/(011)-PMN-0.32PT[178], Terfenol-D/PZT[179], Fe₃O₄/PZN-PT[180], CoFe₂O₄/BiFeO₃[181], LCMO /PMN-PT[182] are numerous demonstrated strain mediated magnetoelectric coupled FE-FM interfaces in the literature.

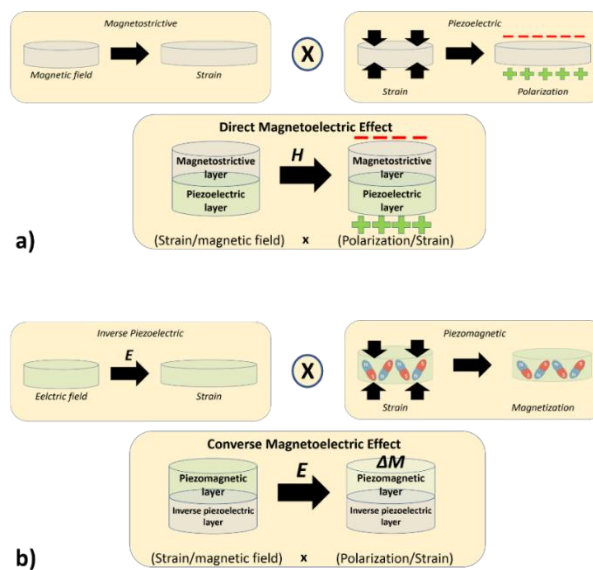


Figure 1.21 Strain mediated magnetoelectric coupling in composite systems composed ferroelectric and magnetic layers **a)** direct ME effect **b)** converse ME effect

As seen in the figure (Fig. 1.22a) structural phase transitions of BaTiO₃ substrate influences coercivity of Fe due to lattice distortions at the interface. The highest change (%24) in the coercivity responses were obtained at orthorhombic-rhombohedral phase transition. This hysteretic effect under electric field (Fig 1.22b-d) related to complex domain switching behavior of orthorhombic and rhombohedral phases of BaTiO₃ unlikely tetragonal phase of BaTiO₃ is an attempt to control magnetization orientation thermally.

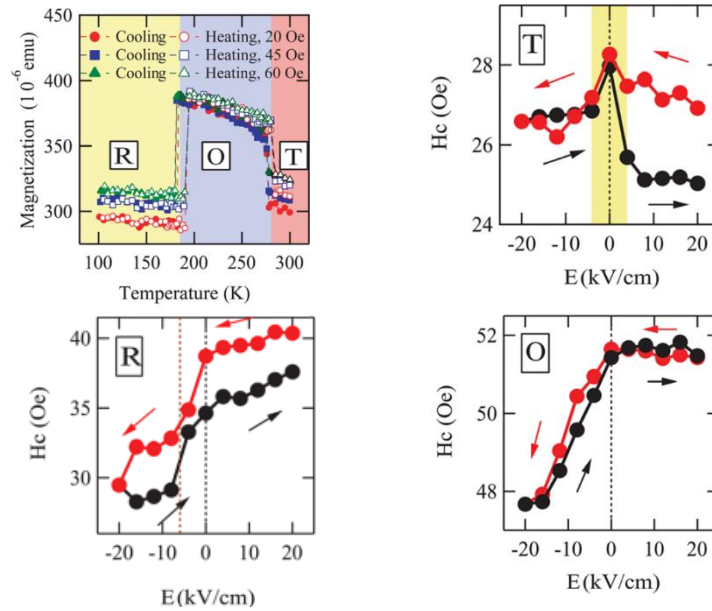


Figure 1.22 a) Temperature dependent magnetization change upon phase transition of BaTiO₃ b) Phase-dependent E-H_c diagram for rhombohedral, orthorhombic and tetragonal phases, respectively [183].

Reported relevant example is 40-nm-thick-LSMO-BTO substrate stack [182]. BTO non-centrosymmetric phase at room temperature exhibiting in-plane (a-domain) and out-of-plane (c-domain) domain structure under zero electric field. Under external electric field, in-plane domains switch to the c-domain orientation (Fig.1.23a).

Generated local stress due to domain switching exerts strain coupling at the interface of the sample and magnetic fluctuation is observed at the LSMO surface (Fig 1.23b-c). Another important result of this work; magnetoelectric coupling value of this heterostructure values, $2.3 \times 10^{-7} \text{ s m}^{-1}$ which is greater than all single phase multiferroic materials.

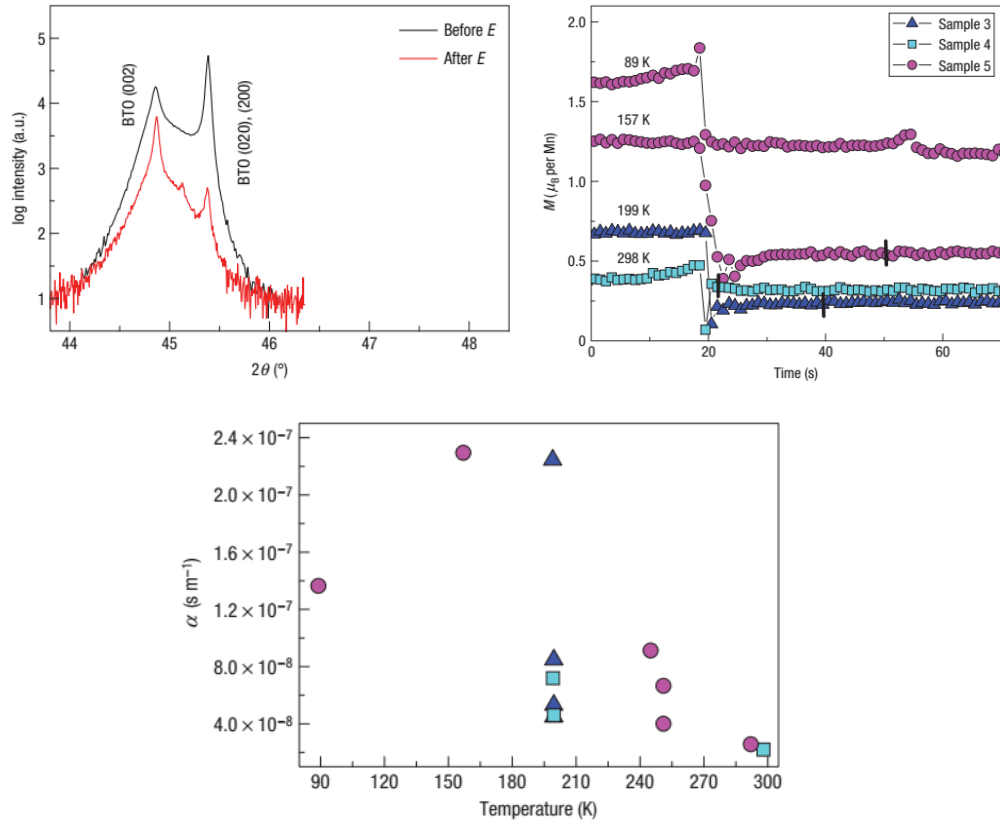


Figure 1.23 a) Diffraction data of domain switching in BTO sample b) Magnetization change under applied electric field c) Magnetoelectric coupling variation under applied electric field via domain structure of BTO[182]

FeRh/BTO interface is another example of strain induced magnetolectric coupling[184]. Lattice distortions on FeRh are strongly effective on phase transitions[185], where orthorhombic-rhombohedral phase transitions of BTO incline ferromagnetic-antiferromagnetic phase transition upon large strain on Ga doped FeRh [186] and there are additional supporting results of electric field control of FeRh/BTO interface via strain transfer [187, 188]. a to c domain switching of ferroelectric layer resulted in AFM phase of FeRh due to compressive strain and the highest inverse ME coupling coefficient $1.6 \times 10^{-5} \text{ s m}^{-1}$.

1.3.1.2 Exchange Bias Mediated Coupling

Exchange bias emerges from exchange anisotropy between a stack of ferromagnetic (FM) -uncompensated FM layer of antiferromagnetic (AFM) interfaces via cooling regime of cooling from Curie temperature (T_C) of ferromagnet to below Neel temperature (T_N) of

antiferromagnet. Exchange bias field (H_{EB}) arises from interfacial energy difference of two opposite orientations at FM layers (Eq.1.93).

$$H_{EB} = \frac{\Delta\sigma}{2M_{FM}t_{FM}} = \frac{2J_{ex}}{a^2} \quad \text{Equation 1.93}$$

where $\Delta\sigma$, interfacial energy difference between two oppositely oriented FM layers, M_{FM} , magnetization of the ferromagnet, t_{FM} , thickness of the ferromagnet, a is the lattice parameter and J_{ex} is exchange coupling across the interface. Magnetic hysteresis shifts unidirectional anisotropy induced directional exchange energy at zero field. In other words, compensated AFM interface has no exchange field as a result of $\Delta\sigma = 0$ condition[189].

Another proposed mechanism asserts exchange field for compensated surfaces, where AFM domain size and roughness results in non-zero exchange field under compensated charge condition, which

$$\Delta\sigma = \frac{4zJ_{ex}}{\pi aL} \quad \text{Equation 1.94}$$

$$H_{EB} = \frac{2zJ_{ex}}{\pi M_{FM}t_{FM}aL} \quad \text{Equation 1.95}$$

where L is the size of the AFM domains, and z is the order of unity[190]. In the presence of electric field while cooling, uncompensated FM spins of AFM layer, which are located next to FM layer, align accordingly to FM spin orientation via exchange coupling. When the opposite field is applied, rotation change is observed, AFM spin configuration remains constant. FM spins stand stable and ferromagnetic configuration owing to microscopic torque applied by AFM spins. Once field rotation has gone back to original state, AFM spins expedite the rotation of FM spins due to unidirectional torque. FM hysteresis loop reveals shift as if a biasing field is applied (Fig. 1.24). This behavior could be defined as exchange bias [191, 192]

There is a certain amount of work to realize exchange bias effect experimentally by coupling different surfaces where BiFeO₃/CoFe heterostructures have achieved promising results [193, 194]. Coupled AFM and FE polarization of BiFeO₃ gives control of AFM spin rotation via an electric field. Rotation of AFM moments ends up with the switching of FM layer. In-plane and out-of-plane FE polarization switching reverse the

oxygen octahedra where canted FM moments and Dzyaloshinskii-Moriya vectors are switched and mediately 180° magnetization reversal occurs. [194]

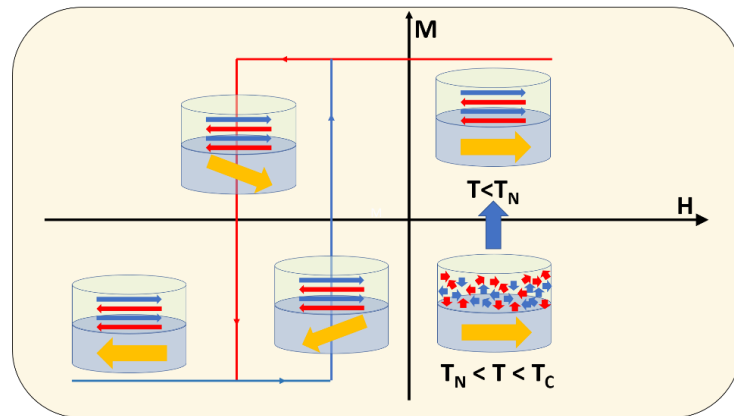


Figure 1.24 Spin configuration of FM-AFM heterostructure of an exchange biased hysteresis loop upon magnetization

1.3.1.3 Charge-Mediated Magnetolectric Coupling

The mechanism in interfacial charge mediated artificial multiferroic structures resemble field-effect-transistor (FET) composed of ferromagnetic (FM) and ferroelectric (FE) layer where polarization charges induce magnetic properties via electron/hole density and density of states of the magnetic layer. Similarly, polarization charges at the gate screened by charge carriers which results in accumulation/depletion through the layer thickness governed by Thomas-Fermi screening length.

Electrostatic control of magnetism in diluted magnetic semiconductors (DMS), complex oxide and transition metal magnets would be crucial for the technological and scientific approach to recent advances in spintronics. By applying an electric field, conductivity and charge density varies in semiconductors where ferromagnetic materials, mostly transition metals and alloys, which are good conductors with high carrier concentration, cannot be manipulated via charge accumulation/depletion at room temperature. When DMS or magnetic complex oxides with low carrier concentration is layered with FE interface, problem of control of magnetic anisotropy carrier concentration at room temperature could be achieved.

Modifying magnetic moment distribution via imperfect screening of FM layer occurs due to spin-dependent screening with respect to Coulomb and exchange interactions. Electric

field induced spin imbalance[195] and mediately change in magnetoelectric coupling coefficient was elucidated by experimental and ab-initio calculations on bcc Fe (001), Ni (001) and hcp Co (0001) [196] where planar charge density over screening characteristics of ferromagnetic metal determines surface density of states under control of exchange splitting in ferromagnetic metal, and spin-dependent charge screening become obvious (Fig. 1.25b). In addition to this, SrRuO₃/SrTiO₃/SrRuO₃ heterostructure (Fig. 1.25a), similarly, magnetic response is function of dominating spin-polarized charge according to the sign of electric field [197]. External field effect could be supplied by ferroelectric layer as previously mentioned resulting in change of surface magnetization by screening charges. Ab-initio study of SrRuO₃ (SRO)/BTO interface[198] where magnetic moment modified 0.32 μ_B per Ru atom has shown that the screening charges arises from ferroelectric switching, contributes significantly exchange splitting by filling the spin-dependent bands which is concordant with Stoner model (Fig.1.26a-b).

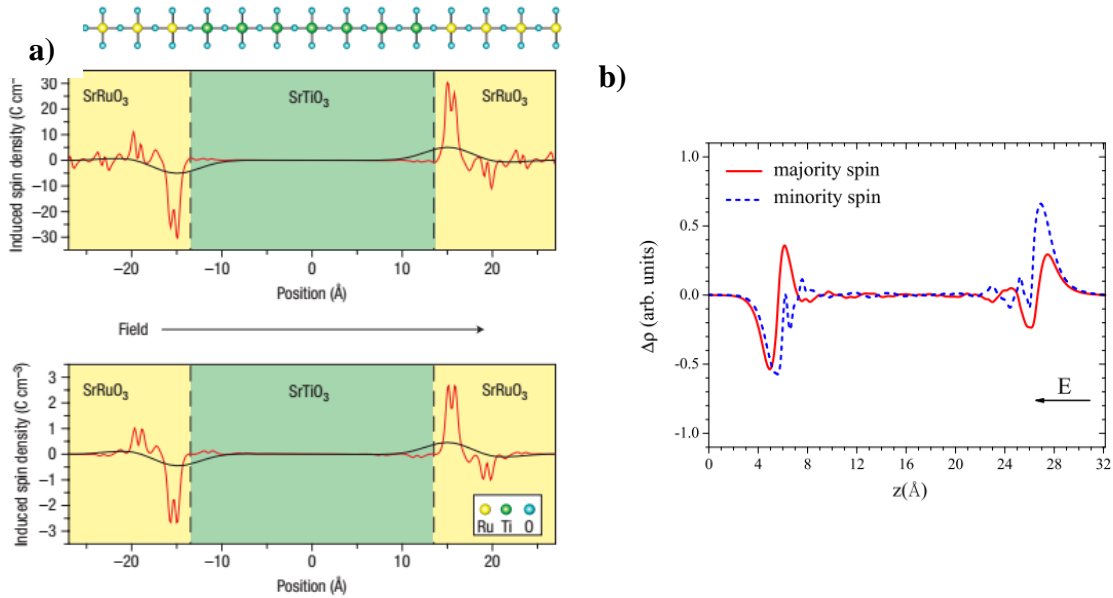


Figure 1.25 a) SrRuO₃/SrTiO₃/SrRuO₃ heterostructure under external static and high frequency electric field [197] b) Average electron density with respect to free-standing 2.1 nm-thick Fe film under external electric field ($E=0.1$ V/nm). Dashed blue line represents minority spin electrons where red solid line represents majority spins.

Obtained results confirm the effect of charge carriers or polarization switching on ferromagnetic oxide surfaces since ferromagnetic LSMO layer has 10^{21} holes cm⁻³ which its screening length is few atomic layers [199].

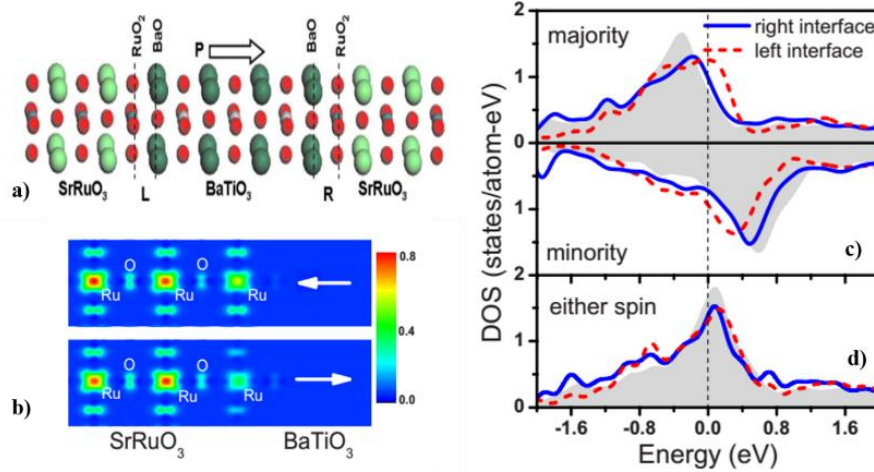


Figure 1.26 a) Sketch of SRO-BTO heterostructure[198] with respect to different polarization directions b) Change in spin density of Ru atoms according to polarization direction c) non-spin polarized and d) spin-polarized local density of states (DOS) of Ru 3d orbitals which are responsible of itinerant magnetization in SRO layer. Solid blue lines represent the condition of polarization direction towards to SRO surface where red dotted lines represent the condition of polarization away from SRO surface. Grey shaded area symbolizes the bulk DOS of Ru 3d.

Additional artificial multiferroic FE-FM heterostructure works are available ab-initio studies about $\text{La}_{0.66}\text{Sr}_{0.33}\text{MnO}_3$ (LSMO) / $\text{PbZr}_{0.2}\text{Ti}_{0.8}\text{O}_3$ [200, 201], and supporting experimental works [202-204] of Molegraaf et. al. and Vaz et. al. has shown that reversible electric field control has contribution to magnetic properties by the means of magnetization, magnetic ordering, and change in Curie temperature. Hence, electronic charge modulation of FE layer could alter magnetization of FM layer via artificial magnetoelectric coupling in this heterostructures [202, 204].

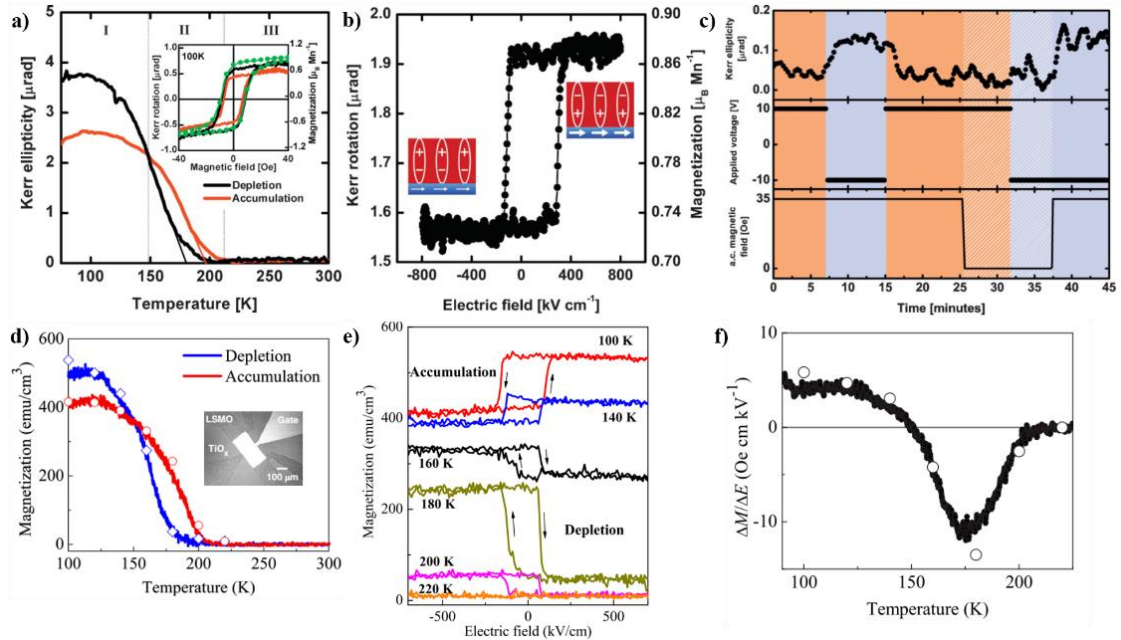


Figure 1.27 a) Magnetization of LSMO with respect to temperature under charge depletion/accumulation states induced by PZT ferroelectric layer [202]. Inset graph shows M-H loop at 100 K b) Magneto-electric hysteresis curve at 100 K, magnetic response is modulated via applied electric field through PZT. c) Magnetism control different cases where orange area symbolizes depletion and blue area symbolizes accumulation states of ferroelectric layer, and it is clearly seen that electric field modulates at zero magnetic field d) Magnetization upon depletion/accumulation states of LSMO/PZT heterostructure [204] e) and f) shows the magnetization-electric field hysteresis change magnetoelectric coupling coefficient under different temperature conditions

As previously mentioned, LSMO is sensitive to charge density either doping or attained electric field, hence; magnetic construction of the structure and mediately phase transitions could be manipulated at FM-FE interface. Ab-initio results comprise zero temperature calculation and interfacial strain effects, while all the experiments and their results are measured above 0 K, where Sr doping up to $x=0.5$ in $La_{1-x}Sr_xMnO_3$ is even proposed metallic FM at room temperature. This approach results in discrepancies in the comparison between theoretical and experimental works. Another conflict about FM-FE interface is about carrier control mechanism of magnetism in LSMO.

Research in charge screening on LSMO, hence magnetization behavior has very limited works. One of the works about magnetization control upon the electric field on LSMO has been searched by Brivio et al. [199, 205]. Gold (Au)/STO/LSMO and

LSMO/STO/Niobium doped STO heterostructures were investigated through charge induced per unit surface in the LSMO layer upon attained electric field:

$$\sigma = \frac{\varepsilon_0 \Delta V}{\delta_{STO}/\varepsilon_{STO} + \lambda_{LSMO}} \quad \text{Equation 1.96}$$

where ε_0 and ε_{STO} are the vacuum and static STO permittivities, respectively. δ_{STO} is the insulating barrier thickness, λ_{LSMO} is the LSMO screening length. According to the Thomas–Fermi theory, the induced volume charge density in LSMO decays exponentially moving away from the surface $\rho_0 \exp(-z/\lambda_{LSMO})$ where z is the distance from the surface and $\rho_0 = \sigma/\lambda_{LSMO}$ is the “surface” modification of the charge density. Electrons are then injected in LSMO, which has $6 \times 10^{21} \text{ cm}^{-3}$ hole concentration, with a concentration being $1.5 \times 10^{21} \text{ cm}^{-3}$ when it is juxtaposed with $SrTiO_3$ (STO) and $2 \times 10^{20} \text{ cm}^{-3}$ one-unit cell away from LSMO/STO interface, where the second plane of Mn atoms is placed. It is proposed that the injected electrons fill holes in Mn^{4+} ions, thus compensating the effect of chemical doping, applied potential in the order of 2.5 V, produces a decrease in the hole doping on the order of 25% and 3.3% on the first and second plane of Mn atoms, respectively. Another achieved the important result of this work is gating geometry. Modification in magnetism was only influenced by a top-gated system where the bottom-gated geometry ingenerated 2-nm magnetic dead layer at the bottom of LSMO interface.

Lu et. al. [206] showed magnetization change (10 %) upon polarization direction enhancing hole accumulation inversely proportional to thickness and electric field affected layer of LSMO extends to 3 nm.

However, contrary to popular understanding, enriched magnetization upon hole accumulation approach [53] in FE-FM interface has been collapsed by assertion several works[207, 208].

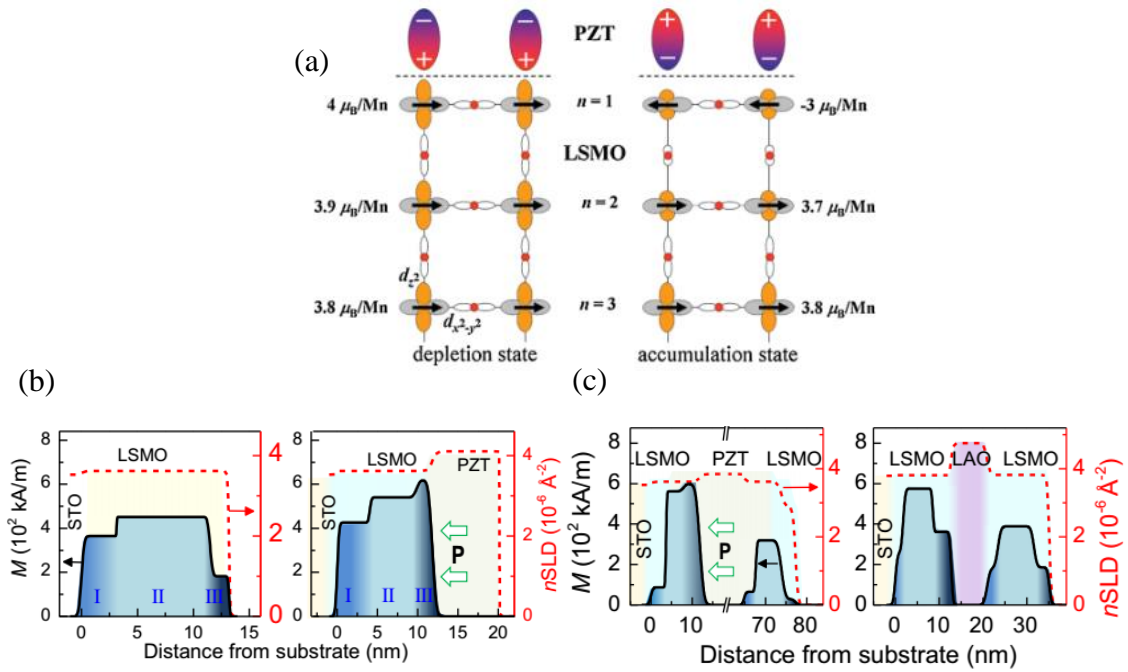


Figure 1.28 a) Schematic of the effect of depletion and accumulation states spin configurations for LSMO in polarization direction change of PZT interface, showing the changes in the Mn and O orbital states and the expected changes in the magnetic moment per layer. The Mn d orbitals are shown orange and grey, and the p orbitals are shown around the oxygen atoms (red) [207] b) Distance dependent magnetization vs. n SLD result for STO/LSMO and STO LSMO/PZT stack is shown. c) Suppressed magnetization at the STO/LSMO interface is shown for both samples, whereas the LSMO/PZT/LSMO sample shows enhanced and diminished magnetization. Comparison with the LSMO/LAO/LSMO sample, which shows lower magnetization at the LSMO/LAO interface, confirms the field effect as the primary role for enhanced magnetization in LSMO in PZT/LSMO heterostructures [208]

Theoretical and experimental results of charge-mediated coupling has guided the basis of the multiferroic tunnel junctions, such that interfacial charge compensation at the barrier/electrode interface via charge accumulation/depletion states forms spin-dependent current flow through the barrier under interplay between electrostatics and magnetostatics.

1.3.2 Multiferroic Tunnel Junctions (MFTJ)

Interplay between electrical and magnetic properties of natural or artificial multiferroics combines and reveals innovative design ideas apart from ferroelectric tunnel junctions with capability to control not only electron transport/tunneling but also spin state of the electron in tunneling process [77]. MFTJ is the concept where ferroelectric layer acts as a tunneling barrier instead of insulating layer between ferromagnetic thin films or FTJ with ferromagnetic electrodes.

The main difference from other types of tunnel junctions is that MFTJ simultaneously have TMR and TER effect [80, 119, 209]. In addition to this, the power of MFTJ originates from the control of spin-polarized charge current via polarization direction or current dependence of the barrier. Polarization bound charges are compensated or screened asymmetrically at the electrode/barrier interface upon polarization direction which resistive switching and memristor behavior survives their validity.

Table 1.4 Review of experimental results of tunneling resistance with MFTJ

Structure	TMR (%)	TER (%)	TEMR (%)	Tc TMR(K)	Year	Ref.
STO/LSMO/La _{0.1} Bi _{0.9} MnO ₃ /Au	81	20	n/a	60	2007	[210]
NDGO/LSMO/BT(1.2. nm)/Fe	-45	37	450	>4.2	2010	[49]
STO/LSMO/BFO(3 nm)/LSMO	69	40	13	>80	2010	[211]
STO/LSMO/Ba _{0.95} Sr _{0.05} TiO ₃ (2 nm)/LSMO	1.1	2	8.5	>RT	2011	[212, 213]
NDGO/LSMO/BT(1.2. nm)/Co	-20	80	82	>4	2011	[50]
STO/LSMO/PZT(3.2 nm)/Co	7.5	700	250	250	2012	[52, 214]
STO/LSMO/BT(3 nm)+LCMO(1-5 u.c.)/LSMO	180	10000	450	180	2013	[215]
LSAT/L6S4MO/BFO(10 nm)LSMO-2	6.6	15.5	18	100	2014	[216]
LSAT/LSMO/BT(2.8 nm)/Co	20	10000	100	>10	2014	[217]
STO/LSMO/PT(3.2 nm)/Co	30	350	15	140	2015	[218]
STO/LSMO/BT(5 nm)/Ni _{0.8} Fe _{0.19}	0.3	1500	300	>8	2015	[219, 220]
STO/LSMO/BT(3 nm)/LSMO	82	125	127	160	2015	[221]
STO/LSMO/BT(6 u.c.)-STO(4 u.c.)/La _{0.7} Sr _{0.3} MnO ₃ 0.2O ₃	30	128	100	>10	2015	[222]
STO/LSMO/BT(6 nm)-La _{0.84} Sr _{0.16} CuO _{3-x} (2 nm)/LSMO	125	104	n/a	n/a	2016	[223]
STO/LSMO/PZT(4 nm)/LSMO	40	100	170	>80	2016	[224]
STO/L6S4MO/PVDF(26 nm)/Co	15	75	288	120	2016	[225]
STO/L6S4MO/BT(5 u.c.)-Pr _{0.8} Ca _{0.2} MnO ₃ (9 u.c.)/LaNiO ₃	24	100	167	>10	2016	[222]
STO/LSMO/BT(4.4 nm)/LSMO	20	1000	n/a	>14	2017	[226]
Si/NMS/STO(2 nm)-PZT(3 nm)/Ni ₅₀ Mn _{36.9} In ₁₅	39	487	224	>RT	2017	[227]
Si/NMS/BFO(4nm)/NMS	13	33	17	>RT	2017	[228]

STO: SrTiO₃, BT: BaTiO₃, NDGO: NdGaO₃, LSMO: La_{2/3}Sr_{1/3}MnO₃, L6S4MO: La_{0.6}Sr_{0.4}MnO₃, BFO: BiFeO₃,
 LSAT:(LaAlO₂)_{0.7}(Sr₂TaAlO₆)_{0.7}, PZT: PbZr_{0.2}Ti_{0.8}O₂, PVDF: Polyvinylidene fluoride, NMS: Ni_{50.2}Mn_{36.0}Sh_{12.8}

1.3.2.1 Magnetolectric Coupling Due to Spin Dependent Screening

Spin-selective tunneling originates from transport inequality between up- and down- spin electrons of magnetic electrodes through an insulating barrier. Experimental realization of spin-dependent tunneling has waited until 1970s[229-232].

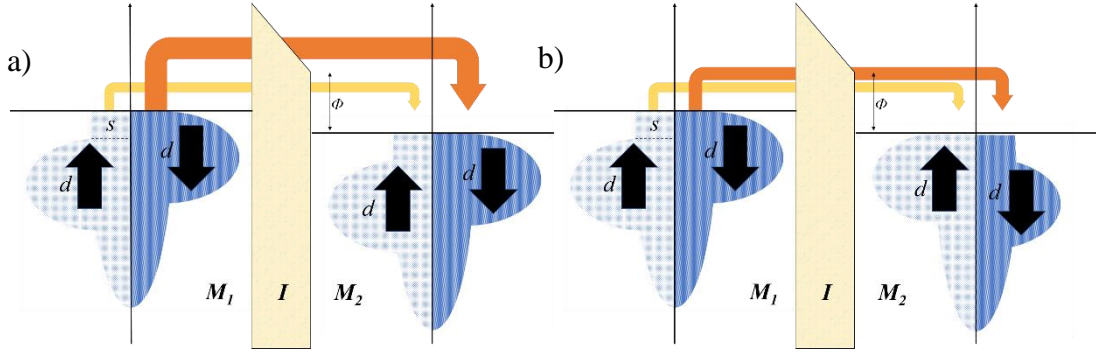


Figure 1.29 Spin-selective tunneling in FM-I-FM stack. a) Magnetization of electrodes are parallel to each other b) Magnetization of electrodes are anti-parallel to each other.

Conductance process in spin-selective surfaces is ingenerated via two conductance channels composed of up- and down- spin electrons of the material. Julierre' s assumption proposes a model that an electron arises from one spin state, is only transported to available spin state of the other layer. Fig. 1.29 illustrates the parallel and antiparallel magnetization of electrodes, where the tunneling current is strongly coupled to relative magnetization alignment of surfaces.

$$P: \frac{N_{\uparrow}(E_F) - N_{\downarrow}(E_F)}{N_{\uparrow}(E_F) + N_{\downarrow}(E_F)} \quad \text{Equation 1.97}$$

The relative resistance or tunneling magnetoresistance change upon parallel (G_P) and antiparallel (G_{AP}) alignment of magnetization is given as the following formula and the Fig 1.30:

$$G_P \propto \rho_1^{\uparrow} \rho_2^{\uparrow} + \rho_1^{\downarrow} \rho_2^{\downarrow} \quad \text{Equation 1.98}$$

$$G_{AP} \propto \rho_1^{\uparrow} \rho_2^{\downarrow} + \rho_1^{\downarrow} \rho_2^{\uparrow} \quad \text{Equation 1.99}$$

$$TMR = \frac{\Delta R}{R_P} = \frac{G_{AP} - G_P}{G_P} = \frac{R_{AP} - R_P}{R_P} = \frac{2P_1 P_2}{1 - P_1 P_2} \quad \text{Equation 1.100}$$

where P_1 and P_2 are the spin polarizations the FM electrodes, respectively.

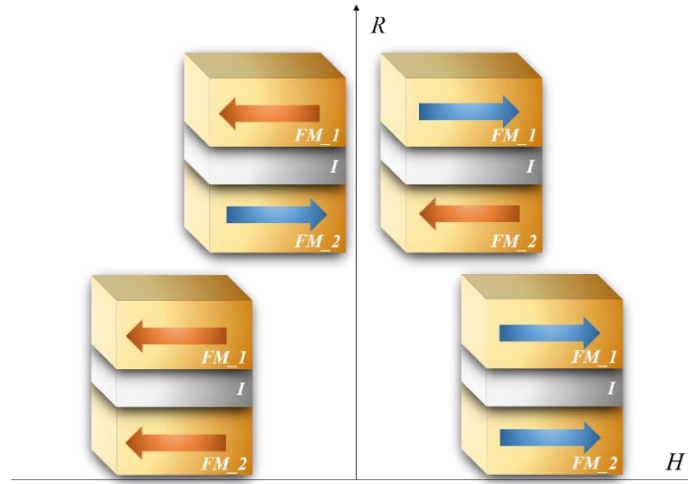


Figure 1.30 Tunneling magnetoresistance depending on up and down spin alignment (or parallel and antiparallel alignment) of the layers.

More accurate explanation for tunneling behavior in magnetic tunnel junctions proposed by Slonczewski [233] including a parabolic band structure of the FM electrodes:

$$P_{eff} = \frac{k_{\uparrow} - k_{\downarrow}}{k_{\uparrow} + k_{\downarrow}} \cdot \frac{\kappa^2 - k_{\uparrow}k_{\downarrow}}{\kappa^2 + k_{\uparrow}k_{\downarrow}} \quad \text{Equation 1.101}$$

where $\kappa = \sqrt{\frac{2m(\varphi - E_F)}{\hbar}}$ is wavevector inside the insulating layer of MTJ and φ is the barrier height and m is electron mass. k_{\uparrow} and k_{\downarrow} are the wavevectors of up- and down-spin electrons. In this model, barrier height is taken into account for the calculation. However, both models neglect the potential and temperature as a function of the mechanism where the bias originated band bending and shifts were pointed out by subsequent researches [30, 234].

Spin polarization simply propounds the measurement of majority spin carrier ratio at Fermi level. Probability of finding electron of a conducting material behind an insulating barrier is explained by overlap of the wavevector of the electron, moreover, if these conducting surfaces are ferromagnetic, exchange interaction comes into play for electronic band structure. To account for spin selective transport, one needs to know the majority spin and minority spin band DOS and the corresponding population density (determined by the Fermi-Dirac distribution) only.

We consider an ultrathin FE layer sandwiched between two FM electrodes as shown schematically in Fig. 1.32. The FM electrodes are assumed to be sufficiently thick that away from the FE interface the bulk properties are recovered. The FE layer sees the bias via assigning a desired electrical potential to the left FM electrode between $-L$ and $-d/2$ (See Fig. 1.31).

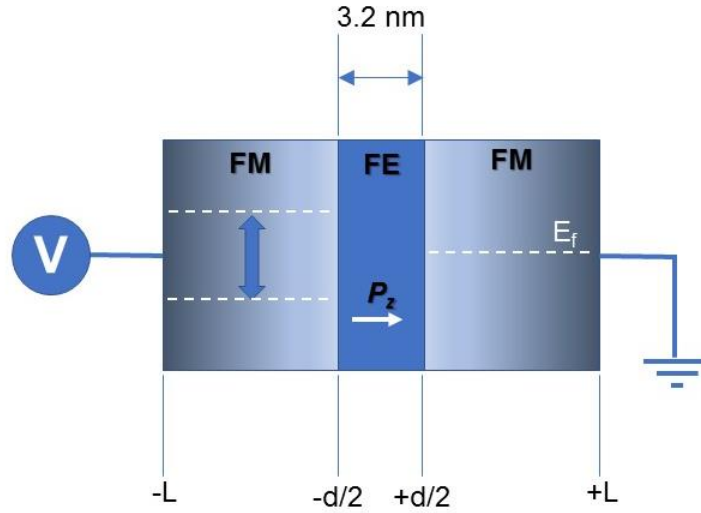


Figure 1.31 The schematic of the FM/FE/FM stack used to compute the spin dependent screening process. The single dashed line on the RHS FM electrode denotes the Fermi level of the stack. The arrow on the LHS FM electrode indicates the shift of the electrostatic potential on this electrode depending on the sign of applied bias V (upper dashed line is negative bias, lower dashed line is positive bias for electrons).

For demonstrative purposes one can also analyze a DE layer sandwiched between FM electrodes where one only has to drop the P_z term from the equations and assign a linear dielectric displacement to the TJ. We fixed the FE thickness to 3.2 nm as this fall into an approximate median of many experimental works [50, 213, 217, 235]. For the case of FE in thermodynamic equilibrium, we assign a small compressive misfit to the FE layer structure allowing us to treat the FE regime with the polarization pointing along the normal of the TJ layer. We mention this point here as we compute the spin population near the Fermi level for non-equilibrium (or “imposed”) polarization and polarization obtained from thermodynamic theory in previous section. The effect of ferromagnetism can be accounted for in the calculations of the charge distribution. We treat the FM electrode as a medium with positively ionized donors and a large density of states near

the Fermi level (10^{27} m^{-3} , similar to that of DFT results yield for Fe, [236]) with electron population that fill these available states (fig.1.32).

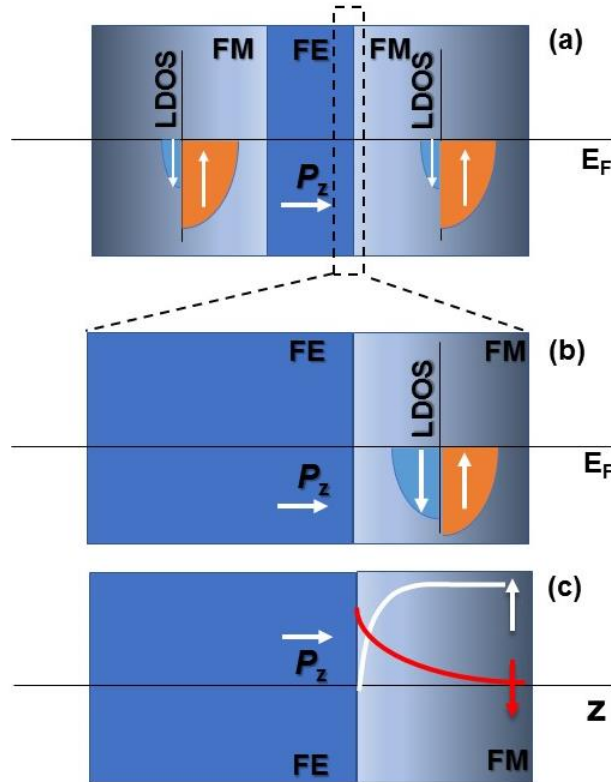


Figure 1.32 The schematic for (a) the spin subband DOS, (b) shift of spin subband DOS near the interface with respect to the bulk and (c) resulting spatial spin distribution near the interface for majority (white arrow) and minority (red arrow) spins

The effect of ferromagnetism can be accounted for in the calculations of the charge distribution. We treat the FM electrode as a medium with positively ionized donors and a large density of states near the Fermi level (10^{27} m^{-3} , similar to that of DFT results yielded for Fe, [236]) with electron population that fill these available states (See Fig. 2 for the schematic). The latter is a common phenomena in 3d transition metals and 4f lanthanides exhibiting magnetic ordering where the net spin can be maximized in accordance with the Hund's rule as the very large DOS in the 3d and 4f bands permit this. In the bulk of the FM the electric field is zero and thus $\rho = 0$. Here, the carrier distribution as well as the DOS in the bands involve the presence of the magnetic exchange giving rise to FM state that can be accounted for in a fashion similar to the Pauli paramagnetism. We follow a route identical to the approximation outlined in Ref. [25] where the DOS in a band can

be thought of as 2 subbands, namely DOS for up-spins and DOS for down-spins. The mean exchange field aligns the spins where one sign of spin is favored over the other thus generating a net non-zero magnetic dipole moment density inside the electrode. From here onwards we will call up-spins “majority spins” and down-spins “minority spins”. The pseudospins in the real lattice pointing in any crystallographic direction consists of majority and minority spins that form the basis states, thus the difference between the majority spin and minority spin concentrations caused by the mean exchange field is the origin of FM behavior. Note that we are not concerned with the crystallographic direction of magnetism as this consideration is related to what one calls “pseudo spin” orientation that can be expressed in terms of the majority spin and minority spin basis states via the Pauli matrices. To account for screening effects, one needs to know the majority spin and minority spin band DOS and the corresponding population density (determined by the Fermi-Dirac distribution) only. In this context, the number of available states per unit volume for each spin subband $g(E)$ near the Fermi level (E_f) can be approximated as

$$g(E)_\uparrow = \frac{1}{2} \int_{E_f}^{E_f+kT} (N_c + g(H_m\mu_b)) dE \quad \text{Equation 1.102}$$

for the up-spins (majority spins) and

$$g(E)_\downarrow = \frac{1}{2} \int_{E_f}^{E_f+kT} (N_c - g(H_m\mu_b)) dE \quad \text{Equation 1.103}$$

for the down (minority) spins. Here, N_c is the DOS at the Fermi level in the paramagnetic state, H_m is the mean exchange field inside the magnetic medium, μ_b is the Bohr magneton, $g(H_m\mu_b)$ represent the DOS corresponding to an energy $H_m\mu_b$ near Fermi level. The $g(H_m\mu_b)$ term is added to the majority spin DOS and is subtracted from the minority spin DOS as there is a transfer of available states corresponding to an energy of $H_m\mu_b$ for a positive H_m , i.e., the magnetochemical potential determines the shift of subbands of spins. In a FM metal such as Fe, this shift can be quite strong due to the strength of the internal exchange field (at the order of 500 T). We here approximate this shift to be occurring only near the Fermi level as $g(H_m\mu_b) \ll E_{DOS_total}$ where DOS_total is the energy range of the total density of states in the relevant band. The mean exchange field, H_m , is of quantum mechanical origin and is assumed constant inside the bulk of the FM medium where $E = 0$. Considering the dependence of the FM order on

carriers, namely the itinerant contribution, H_m is naturally sensitive to carrier, hence, spin density and can be modified approximately for charge redistribution in case of electric field penetration into the magnetic medium as

$$H_m = H_0 + w\mu_b(n_{\uparrow}^+ - n_{\downarrow}^+) \quad \text{Equation 1.104}$$

for a material such as Fe or Co, H_0 is the mean exchange field in the bulk of the FM, w is a coupling coefficient (taken as unity here, See Ref. [25]). The approach laid above is sometimes known as the Stoner-Wohlfarth model to introduce the spin dependence of DOS, i.e., the subband available states. In the FM electrode the Fermi level lies inside the conduction band. The majority spins aligned parallel to H_m will have a larger share of the band states than those that are antiparallel to H_m . One can thus write n^- (namely the population density) and N_D^+ terms in Eqs. 1.105-107 as

$$N_D^+ = N_D \left[\exp\left(\frac{q(E_D - E_F - \phi)}{kT}\right) + 1 \right]^{-1} \quad \text{Equation 1.105}$$

$$n_{\uparrow}^- = g(E)_{\uparrow} \left(\exp\left(\frac{q(E_C - E_F - \phi) - \mu_b H_m}{kT}\right) + 1 \right)^{-1} \quad \text{Equation 1.106}$$

$$n_{\downarrow}^- = g(E)_{\downarrow} \left(\exp\left(\frac{q(E_C - E_F - \phi) - \mu_b H_m}{kT}\right) + 1 \right)^{-1} \quad \text{Equation 1.107}$$

at a given coordinate inside the FM electrode. In Eqs. 1.105-107 N_D^+ (N_D) is the ionized (total) donor density in the FM electrode of the FE film. n^- is the electron density written for the majority spin and minority spin subbands, $g(E)$ have their usual meanings as denoted in Eqs. 102,103. E is the energy of an electron at the top of the valence band at a given coordinate in the FM electrode, E_F is the Fermi level, ϕ is the local electrostatic potential, $\mu_b H_m$ is the magnetochemical potential a carrier feels depending on its spin. The sign of this term is $-$ for majority spins and $+$ for minority spins. All the band parameters for FM and the FE are given in Table 1.5 The Fermi level of the stack is assumed to be equal to that of the FM electrode, which we take as that of Fe here.

Table 1.5 Band parameters for FE and FM

	$g(E_F) (m^{-3}),$	$E_f, E_c, E_v (eV)$	$H_0 (T)$	$N_D (m^{-3})$
FM	$10^{27}, 10^{27} *$	-4.5	500	10^{27}
FE	Not considered (insulator limit)	-5.0, -3.2, -5.5	-	-

Electrostatic (for the potential) and non-electrostatic boundary conditions (for the polarization) are needed to obtain solutions to the above equations. The boundary conditions for the electrostatic potential is:

$$\Phi_{FE} = \Phi_{FM} \Big|_{z=-\frac{d}{2}} \text{ and } \frac{d\Phi}{dz} = 0 \Big|_{-L,+L} \quad \text{Equation 1.108}$$

implying the continuity of the potential at the FE/FM interfaces, where Φ_{FE} and Φ_{FM} are the electrostatic potentials inside the FE and the FM electrodes respectively and second differential BC in Eq. (108) indicates the absence of electric field away from the FE/FM interfaces. Polarization BCs are given in the Sect. 1.3. The bias forming the electric field on the system is always assigned to the LHS FM electrode while the RHS electrode is kept grounded, similar to experiments. Periodic boundary conditions (BCs) are employed along the plane of the structures for both the electrostatic potential and polarization. One can approximate the volumetric magnetic dipole moment density obtained from

$$M = \mu_b(n_{\uparrow}^- - n_{\downarrow}^-) + \mu_b N_d^+ \quad \text{Equation 1.109}$$

where the first term on the rhs is the itinerant contribution and the second term is the contribution from ionic sites in the lattice. One would thus expect a competition between electrostatic screening and M through the charge distribution function noting that $H_m = \mu_b H_0 + w\mu_b(n_{\uparrow}^- - n_{\downarrow}^-)$. Throughout the work, the value of H_m has the same sign in the LHS and RHS FM electrodes corresponding to parallel magnetization as this allows us to identify FE polarization effects distinctly. Different signs of H_m would mean different relative orientation of the magnetization in the layers corresponding to different subband DOS in the FM electrodes. The effect of relative magnetic orientations on magnetoresistance is well-understood since the first papers of Fert group and Grünberg group [26, 27, 237] and is not considered here. We shall, however, show in Results and Discussion that FE polarization impacts locally the subband DOS hence the spin

population at the interfaces for positive H_m on LHS and RHS FM electrodes, changing the local magnetization amplitude of FM electrodes.

The tunneling currents for the majority spins and minority spins across the FE TJ can be calculated using the dual spin channel approximation where the current for a given sign of spin depend on the population density of that spin at the interface as well as the barrier modified by the magnetochemical potential for that spin and the relative ratio of the subband available states in the opposite electrodes. The total current J is then

$$J = J_{\uparrow} + J_{\downarrow} \quad \text{Equation 1.110}$$

where

$$J_{\uparrow} = N_{\uparrow} T_{\uparrow}(E) v \quad \text{and} \quad J_{\downarrow} = N_{\downarrow} T_{\downarrow}(E) v \quad \text{Equation 1.111}$$

In Eq.1.111 above, N_{\uparrow} and N_{\downarrow} are the population densities of majority and minority spins at the FE/FM interface on the FM side (RHS electrode in Fig. 1.32 taken as the reference), $T_{\uparrow}(E)$ and $T_{\downarrow}(E)$ are the transmission probabilities of the up- and minority spins and v is the Richardson velocity found from $v = \sqrt{2kT/m^*}$ where m^* is the effective mass of the electrons near the bottom of the conduction band of BT. $T_{\uparrow}(E)$ and $T_{\downarrow}(E)$ are obtained from the previously derived WKB approach for an arbitrary potential barrier at any coordinate r , $V(r)$ inside of the turning points of the electrostatic potential given by

$$T_{\uparrow}(E) = \frac{g(E)_{\uparrow}}{g(E)_{\uparrow} + g(E)_{\downarrow}} A \prod_{-d/2}^{d/2} \exp\left(\frac{\Delta d}{\hbar} \sqrt{2m^*(V_{\uparrow}(r) - E(V_{app}))}\right) \quad \text{Equation 1.112}$$

$$T_{\downarrow}(E) = \frac{g(E)_{\downarrow}}{g(E)_{\uparrow} + g(E)_{\downarrow}} A \prod_{-d/2}^{d/2} \exp\left(\frac{\Delta d}{\hbar} \sqrt{2m^*(V_{\downarrow}(r) - E(V_{app}))}\right) \quad \text{Equation 1.113}$$

with the only difference being the local potential $V(r)$ an electron feels at the interface which could depend on the sign of its spin, $E(V_{app})$ is the energy of an electron under an applied potential drop V_{app} , $g(E)$ are calculated from Eqs. 1.102-103, \hbar is the reduced Planck constant. The constant A is

$$A = \frac{16E}{V_0} \left(1 - \frac{E}{V_0}\right) \quad \text{Equation 1.114}$$

The prefactors concerning the subband LDOS stand for the effect of this term on transmission, i.e., if there is a great mismatch between the subband LDOS at the interfaces

between the LHS and RHS FM electrodes for a given spin sign, there is reduced tunneling current with that spin polarization. We give the WKB formula above in its discrete form to be able account for the “arbitrariness” of the electrostatic potential across the barrier as this barrier can have significant variations as a function of polarization (even when homogeneous) and applied field, unavoidable necessitating a numerical treatment to calculate the currents in the spin channels. The spin-dependent potential barriers, $V_{\uparrow}(r)$ and $V_{\downarrow}(r)$ can be expressed in terms of the band parameters modified by the electrostatic and magnetochemical energies as:

$$V_{\uparrow,\downarrow}(r) = E_C^{FE} - E_F - \phi(r) \mp \mu_b H_m \quad \text{Equation 1.115}$$

where E_C^{FE} is the energy of the bottom of the conduction band of the FE layer, $\phi(r)$ is the local electrostatic potential at a coordinate r inside the FE layer, the $\mp \mu_b H_m$ term denotes the magnetochemical potential in the majority and minority spins near the Fermi level, E_f , in the FM electrode. Majority and minority spins have, in fact, separate E - k curves and form separate “conduction subband” curves as demonstrated via first principles calculations for FM materials [238] The amount of “conduction subband” separation along easy axis such as [110] reported for Fe, Ni and Co vary from 2 eV to 0.6 eV [239] in very close proximity to the value we compute in this paper (~ 0.85 eV) considering only the spin population near the Fermi level. A separation of subband energies directly mean that the majority and minority spins “see” different barriers during tunneling. The FE TJ acts as an electrostatic barrier with the barrier height determined with respect to the energies of the majority and minority spins inside the conduction band of the FM metal under a given bias on the LHS electrode. In the calculations of the currents, $\phi(r)$ and H_m (See Eq. 105) are found numerically from the solution of Eq. 1.59 that contains the terms in Eqs. 1.80 and 1.105-107 assuming the condition that the polarization of the FE layer remains unchanged due to the great difference in the timescales of ferroelectric polarization dynamics and tunneling phenomena under pulsed bias. The charge distribution, ρ , however, will adapt rapidly to the applied bias and will be near-equilibrium as carrier relaxation times in a metallic medium is on the order of 10^{-14} seconds compared with bias durations of a few nanoseconds.

We employ a finite difference discretization in 2D and carry out a Gauss-Seidel iterative scheme to solve the coupled Eqs.1.59, 1.80, 105-107 and 82-83 simultaneously subject to

the relevant BCs provided above in the case of homogeneous and equilibrium polarization states whose results we discuss in the next sections. The computation grid consists of 200×400 points where h is the distance between the nearest nodes both along x - and z -axes with a value equal to the unitcell of BCC Fe (~ 2 angstrom), where n is the number of nodes whose sum gives the FM/FE/FM trilayer thickness (40 nm total). We terminate the solution after 10000 iterations that yield a difference of less than 10^{-4} for ϕ and P between two consecutive steps. All results here are provided for room temperature calculations.

2 Results and Discussion

The spin polarization and magnitude of currents across a TMR stack depends on the relative orientation of the magnetism in the FM electrodes and a bias simply controls the electrical barrier to spin tunneling via the polarization of the ferroelectric layer. The driving force behind such a pursuit was that the FE polarization can dramatically alter the ON/OFF ratios of spin currents depending on the direction of remnant dipoles as they can easily be switched under a few volts of bias. TMR in FE TJs has been studied but similar to the TMR effect in FM/DE/FM stacks with the DE as the TJ, loss of spin polarization in tunnelling currents at moderate to high bias values is a persisting problem[240-242] even in the case of magnetization being parallel in the FM electrodes. The origins of such an outcome has been discussed extensively by a few authors for DE TJs. [243-246] The flipping of the spins of “hot” electrons (those who have gained energy above the Fermi level of the FM electrodes) following tunnelling, magnon excitations and scattering events from defects inside the TJ that induce spin flips were discussed as major scenarios degrading the TMR effect. The changes in interface states in TJ/FM junctions has been mentioned in a few works. [199, 246] From the continuum media perspective, one would expect the electrostatic potential dominate over the magnetochemical potential an electron feels near a dielectric/FM interface under bias, keeping in mind magnetochemical potential promotes carriers to higher energies and charge distribution occurs always to minimize electrostatic energy. The finite penetration of the electric field to the surface of a metallic FM in a dielectric/FM junction under a potential drop will mostly be screened by majority spin electrons of the FM near the Fermi level. Strong electric fields could require carrier densities much greater than the population density allowed by the subband DOS of the majority spins. It can thus be expected that minority spin carriers can take effect and participate in the screening process as long as the energy difference between the spin subbands is not extreme such as in the case of half-metals. FEs can generate very strong fields near a metallic or semiconductor interface and pave a way to effectively manipulate carriers as well as their spins.

Here, we present the results of the effect of the electrostatic screening process of FE polarization charges on magnetoresistive effects. For this purpose, we study a FM/FE/FM stack using the continuity equations in continuum media and study the spin dependent screening at the FM interfaces that has important implications for obtaining

the TMR effect from such structures. The competition between the electrostatic and the magnetochemical potential of carriers at the FE/FM interfaces is demonstrated. Spin mixing, namely reduction of the majority/minority spin population ratio, occurs at the interfaces where the local density of states (LDOS) for minority spins is greater than in that of the bulk. This is driven by the need to screen polarization charges if the FE layer has a relatively strong polarization or is under a strong bias. By considering majority and minority spin channels, we try to quantify the limits of FE polarization and applied bias beyond which spin polarized currents are unlikely that would result in reduction of the TMR. We prove so by directly computing the tunnelling currents for majority and minority spin channels using the Wentzel-Brillouin-Kramers (WKB) approximation. The difference in the population densities of majority and minority spins at the interface tend to disappear (spin mixing) along with an increase in LDOS at the FM/FE interface of the other electrode to which electrons tunnel. Such a phenomena naturally leads to the disappearance of the spin polarization of the tunnelling currents. In addition, we calculate an abrupt change in barrier heights the spins feel under moderate bias (0.25-0.5V) that is also expected to degrade spin polarization in currents.

2.1 FM/FE/FM with FE having homogenous polarization

We first discuss the numerical results we obtained by imposing a homogeneous polarization to the FE layer in the FM/FE/FM stack. The direction of the P_z is fixed at all times with dipoles pointing from the LHS electrode to the RHS to induce accumulation on the RHS electrode (tunnelling is therefore expected to occur from RHS FM to the LHS FM) as we always apply the a positive bias to the LHS electrode (See Fig. 1.32). The opposite configuration (P_z pointing from RHS to LHS) will also yield exactly the same results owing to the symmetry of the stack and is not necessary to discuss. Poisson equation is solved along with the charge terms in Eq. 1.80 under fixed homogeneous P_z . FE polarization on its own would simply be expected to generate significant electric field penetration into the electrodes and therefore depolarizing fields inside the FE but our focus here is on the FM electrodes and the spin distribution.

The spin-dependent spatial carrier accumulation for various values of P_z both for zero and non-zero bias are provided in Fig. 2.1. Note in this plot that minority spin population away from the interfaces is not zero (red lines) but several orders of magnitude less than majority spin population. It is immediately visible in Fig. 2.1c that larger P_z

values lead to minority spin accumulation at the interface in a FM electrode that contains otherwise majority spin electrons. This is a consequence of the electrostatic screening process and it is this very process that also leads to spin-mixing. With increasing bias, the region in which minority spins accumulate grows. For fixed P_z , the linear field dependent part of dielectric displacement, D_z , is the only bias sensitive part. This condition can be justified based on the approximation that most tunnelling experiments are measured under rapid pulsed voltages where P_z has no time to adapt to the rapidly changing voltage drops across the system. The carriers in a metallic medium, however, have relaxation times on the order of 10^{-12} seconds or less and will quickly establish their equilibrium distribution satisfying Poisson equation(Eq.1.80) for pulsed bias durations of a few nanoseconds.

Spin mixing occurring at the FE/FM interfaces is strongly driven by the change in the subband DOS near the interfaces due to the need for electrostatic screening of the FE dipoles. The need arises because the electrostatic energy an electron would feel under the potential of unscreened polarization bound charges is several times more than the local magnetochemical potential. For electron energies limited to values around the Fermi energy, a strong local potential drop caused by the partially screened FE polarization charges could require carrier densities exceeding the subband states for the majority spins available in bulk.

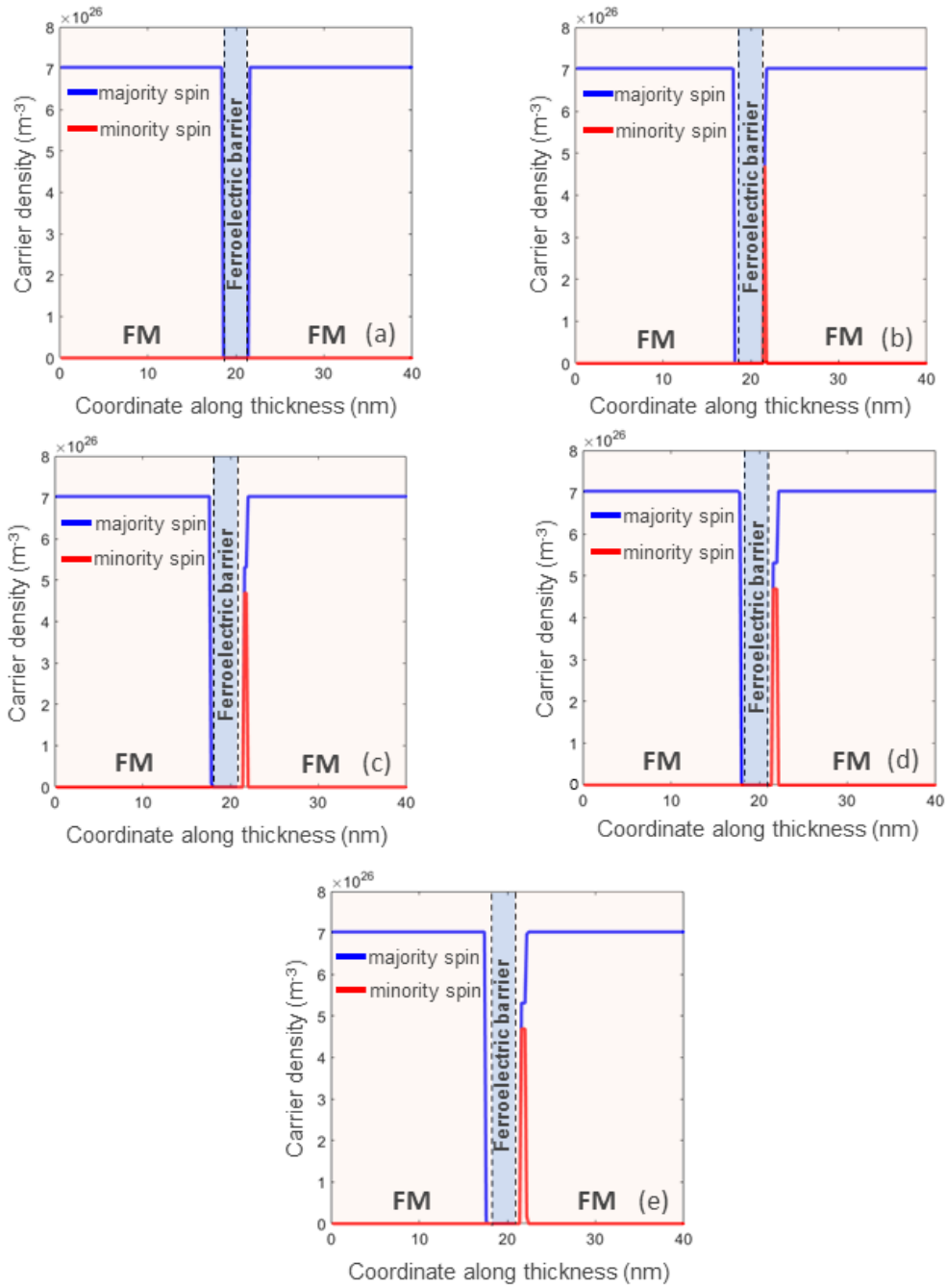


Figure 2.1 Average carrier population density at the RHS FE/FM interface induced by homogeneous P_z for (a) $P_z = 0.1 \text{ C/m}^2$, (b) $P_z = 0.2 \text{ C/m}^2$ at 0V bias, (c) $P_z = 0.2 \text{ C/m}^2$ at 0.5V bias, (d) $P_z = 0.3 \text{ C/m}^2$ at 0V bias and (e) $P_z = 0.3 \text{ C/m}^2$ at 0.5V bias. Notice the minority spin accumulation for increasing P_z as well as bias. For the case of $P_z = 0.1 \text{ C/m}^2$ no plot when under bias is given as there is no considerable change in minority spin population at the interface.

Looking at Fig. 2.2, for weak FE polarization in the TJ, we do not observe any change in the subband available states at the interfaces, which we call from here onwards local available states (LAS, given in density units of m^{-3} , see Eqs. 1.102 and 1.103) with respect to interior of the FM, hence a spin mixing will not be expected near the interface (See Fig. 2.2a for population density distribution). This is because the subband available states for the majority spins can accommodate sufficient local electron density (the population density) for screening of FE polarization and the subband LAS for all spins remain almost unchanged at zero to moderate bias ($< 0.5\text{V}$). On other hand, the subband LAS near the interfaces start to change for the case of moderate P_z amplitude (approx. 0.2 C/m^2 here) and upon applying a low-to-mid positive bias to the LHS FM electrode, the region where the minority available states is comparable to majority ones extends slightly.

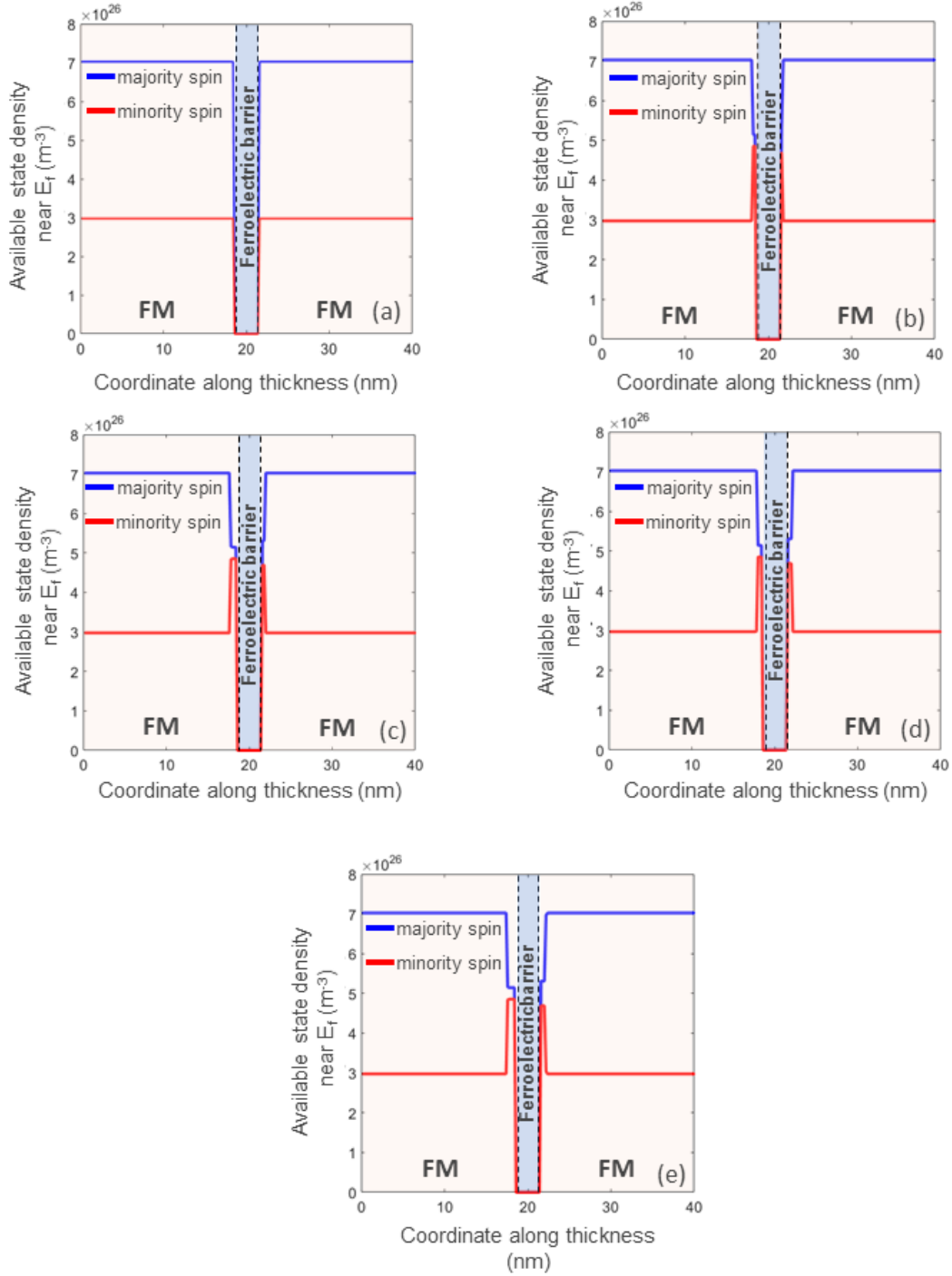


Figure 2.2 Average subband LDOS at the RHS FE/FM interface induced by homogeneous P_z for (a) $P_z = 0.1 \text{ C/m}^2$, (b) $P_z = 0.2 \text{ C/m}^2$ at 0V bias, (c) $P_z = 0.2 \text{ C/m}^2$ at 0.5V bias, (d) $P_z = 0.3 \text{ C/m}^2$ at 0V bias and (e) $P_z = 0.3 \text{ C/m}^2$ at 0.5V bias. Notice the minority subband LDOS increasing at the interfaces for increasing P_z as well as bias

Very importantly, the same conclusion was reached by first principles study in Ref. [247] wherein it was shown that the minority and majority subband LDOS near Fermi energy at the interface differ considerably from bulk for Fe 3d states in the same manner we show in this work (see Fig.2.3), i. e., the minority spin subband available states increases at the interface compared to bulk values. The increase in the minority spin population near the Fermi level should be expected at the expense of increase in magnetochemical potential of carriers as further accumulation of majority spins for screening of polarization charges would mean electrons populating higher energies and is not electrostatically favorable.

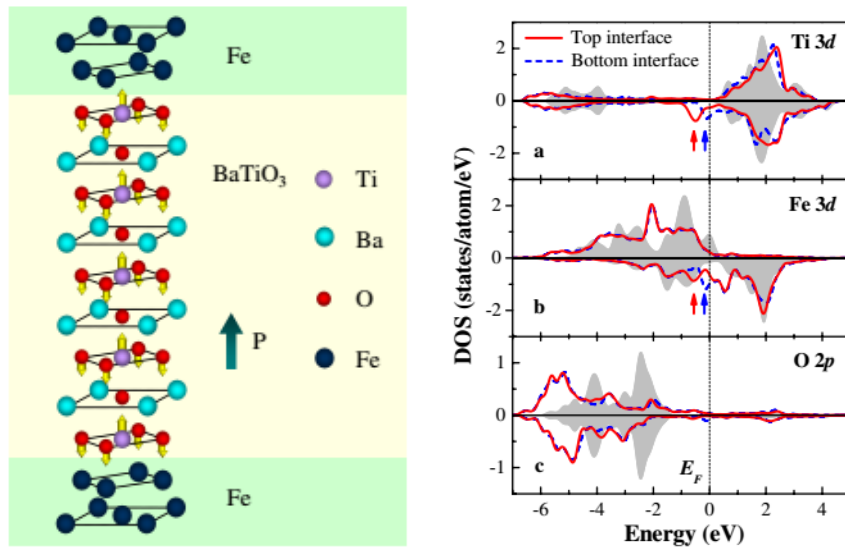


Figure 2.3 a) Atomic structure of Fe-4 layer of BaTiO₃ structure. b) Orbital-resolved DOS for interfacial atoms in a 4 layer of BaTiO₃ (a) Ti 3d, (b) Fe3d, and (c) O 2p. Majority- and minority-spin DOS are shown in the upper and lower panels, respectively. The solid and dashed curves correspond to the DOS of atoms at the top and bottom interfaces, respectively. The shaded plots are the DOS of atoms in the central monolayer of (b) Fe or (a),(c) TiO₂ which can be regarded as bulk[247]

To provide a graphical guide to identify the possible regimes of FE polarization that allow spin polarized tunnelling and when spin polarization would disappear, we give the plot in Fig. 2.4. The averages of the majority and minority spin population density at the right FE/FM interface coordinate are provided along with the spin subband LAS near the Fermi level on the left FE/FM interface coordinate as a function of P_z at zero bias. In this plot, the population density is given in the positive axis and the subband LAS near the Fermi level on the LHS FM is in the negative axis for convenience of comparison. Despite the

obvious fact that precise numerical values here might differ for real experiments, it is clear that with increasing P_z , the spin polarization of the currents is expected to disappear as population densities of majority and minority spins become identical in the RHS FM interface. In addition, note that, according to Eq. 1.115, the minority spins feel a “higher potential” that causes an approx. 0.85 eV decrease in barrier for these carriers as well (relative to the majority spins), allowing easier tunnelling for these carriers at any given bias, further diminishing the TMR. Voltage dependence of the spin polarization emanating from the different barriers the spins penetrate during tunnelling has been first explicitly analyzed in Ref. [199]. In addition to the information given in that work, we argue that this difference in barrier heights tends to disappear for increasing P_z in the case of a FE TJ in the coming paragraphs.

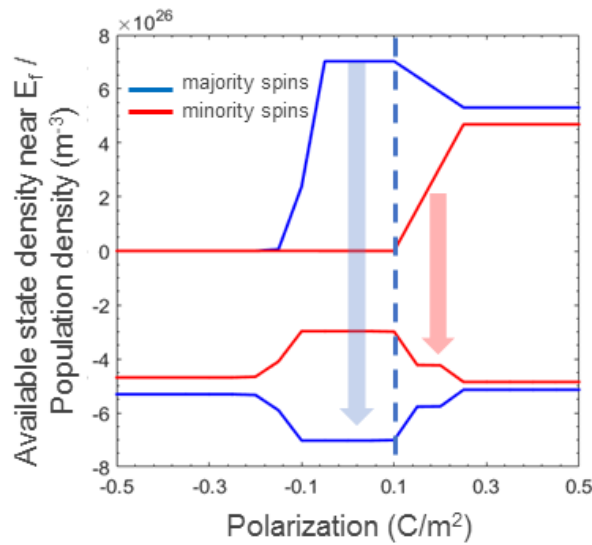


Figure 2.4 Average population density (positive vertical axis) at the RHS FE/FM interface and the subband LDOS (given in the negative vertical axis) at the LHS FM/FE interface as a function of P_z . The blue arrow denotes indicates that almost fully spin polarized tunnelling will occur from RHS FE/FM interface states to subband LDOS of the LHS FM/FE interface states. Beyond values of P_z around 0.15 C/m^2 loss of spin polarization is expected as minority spin population starts to build up on the RHS FE/FM interface along with an increase in the minority subband LDOS on the LHS FM/FE interface as indicated by the shorter red arrow.

As majority spins dominate the population density of the RHS FE/FM interface at low polarization (until around 0.15 C/m^2), there will be mostly majority spin tunneling below this regime to the available subband LAS at the RHS interface in the RHS FM electrode indicated by the thick blue arrow. The subband LAS near the Fermi level on the LHS electrode are at a maximum below 0.15 C/m^2 (See Fig. 2.4). Once P_z is higher than this value, a gradual increase in minority spin population starts along with an increase in subband LAS of the minority and majority spins on the LHS electrode to which the tunnelling would be expected to occur, indicated by the red arrow. Strong amplitudes of P_z causes further spin mixing at the RHS and the subband LAS at the interface of the LHS electrode are almost identical, indicating that the tunnelling currents will not be spin polarized in this regime. In fact, moderate-to-strong applied bias (0.5-1 V) for when P_z is less than the critical value of 0.15 C/m^2 here generates a similar effect: A bias of such magnitude can cause loss of spin polarization even if P_z is relatively weak analogous to the observations in dielectric TJs between FM electrodes. While bias can cause spin mixing at the interface causing reduction in spin polarization, current amplitudes are expected to scale exponentially with applied bias. P_z determines both the spin polarization at the FM interfaces as well as the tunnel current amplitude in a symmetric FM/FE/FM stack. A strong P_z in the FE layer generates a “deeper” penetration of the electric field into the LHS electrode, effectively increasing the barrier width. We give Fig.2.5 to display the extent of field penetration that causes the exposure of positive charges on the LHS FM electrode and carrier accumulation on the RHS FM electrode interface. Electric field exposes the positive ions in the lattice on the RHS FM deeper into the electrode with increasing P_z , thereby increasing effective barrier width. The left FM/FE interface undergoes carrier depletion as the negative pole of the FE polarization terminates at this interface thus repelling electrons away from the interface exposing the FM metal ions. Strong P_z values, apart from generating spin mixing, could thus cause reduction in the tunnelling currents in the FE TJ for a given bias. This outcome is on top of the

disappearance of the TMR effect in the tunnelling current amplitudes for majority and minority spin electrons as we discuss in the next paragraph.

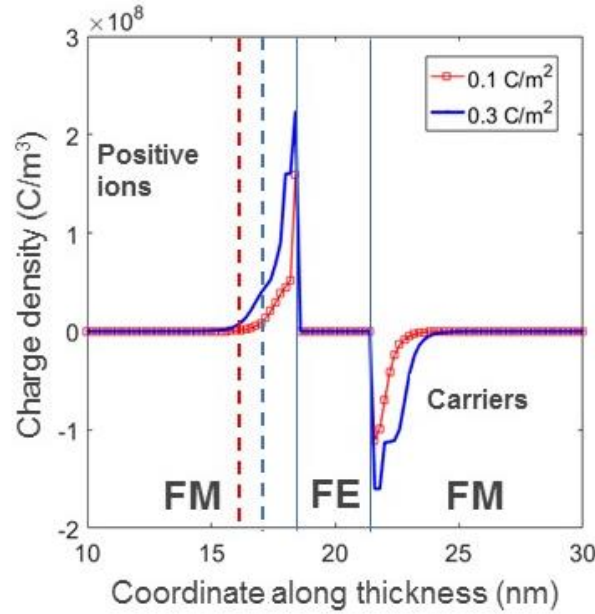


Figure 2.5 Total charge density across the trilayer indicating the exposed positive ionic sites on the LHS FM/FE interface and the carrier accumulation near the RHS FE/FM interface for 2 different P_z values. Stronger P_z causes a deeper penetration of the electric field to the RHS FM electrode increasing the effective barrier width to tunnelling for carriers on the LHS FE/FM interface.

The fundamental mechanism behind the spin mixing at the RHS FE/FM interface is therefore simply the “need for electrostatic screening”, which becomes dominant over the magnetic ordering of carriers in the FM. In other words, minimization of the electrostatic energy via screening of FE polarization charges via the carriers overwhelms the magnetochemical energy favoring magnetic order and could locally diminish magnetism on the RHS right FE/FM electrode interface. Considering, in addition, the spin sign dependence of the barrier, we calculated the average barrier heights for minority and majority spins as a function of P_z in the FE TJ from Eq. 23 and are displayed in Fig. 2.5. The different barrier heights for both spins follow a very gradual increase with increasing polarization in the TJ until around 0.15 C/m^2 .

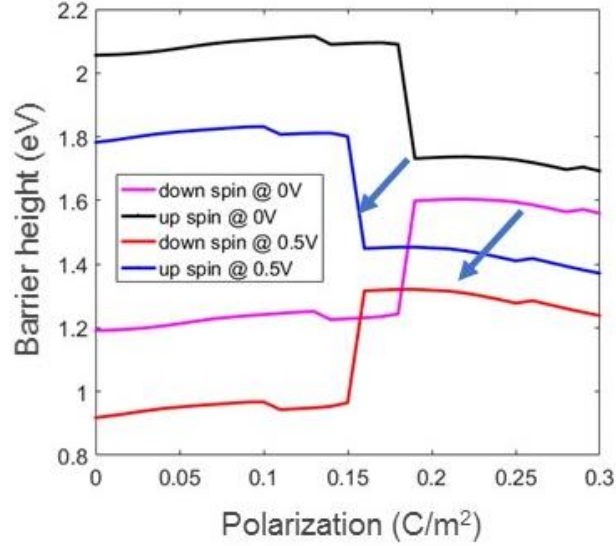


Figure 2.6 Average potential barrier height for minority (down) and majority (up) spins as a function of P_z for 0V bias and 0.5V bias. The potential barrier for both type of carriers is reduced by the application of bias as expected. The sudden change in the barrier heights correspond to the regime when minority spin carriers participate in the screening of P_z .

This is the onset of minority spin accumulation that becomes energetically feasible near the interfaces, which then suddenly changes the electrostatic barrier for both majority and minority spins after which both carrier types experience similar barriers. A positive bias on the LHS FM electrode lowers the entire barrier regime as expected that drives the tunnelling currents. Both for zero and non-zero positive bias, the sudden shift of the barriers occurring at a critical P_z value, however, is not accompanied by a sudden change in tunnelling currents (Fig. 2.7) obtained by the WKB method outlined in Sect. 1.3 As explained in the previous paragraph, increasing the polarization value widens the effective physical barrier thickness due to the carrier depletion on the LHS FM/FE interface that counteracts the lowering of the electrostatic barrier, making the results of the WKB calculation vary smoothly with bias. It can immediately be noted from Eqs. 1.112-1.113 that an increase in the barrier thickness will dominate the currents as the exponent term in $T(E)$ depends on barrier thickness linearly while it depends on square root of the potential barrier. Both channels of spin currents therefore diminish for stronger P_z as seen in Fig. 2.7.

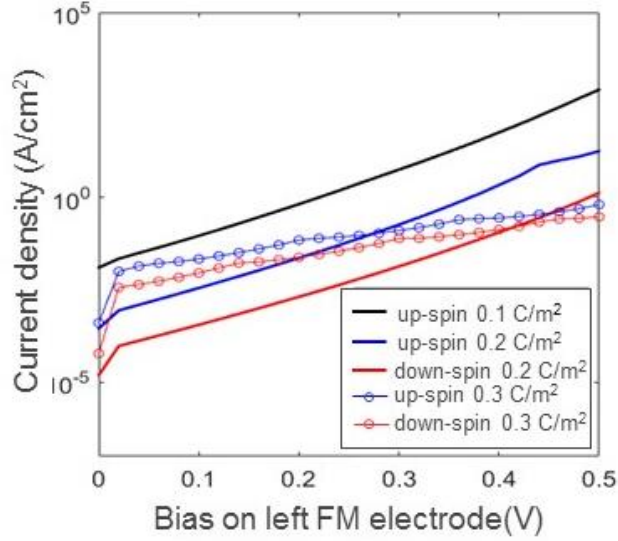


Figure 2.7 Tunnelling currents for minority and majority spins calculated using the WKB approximation for various homogeneous values of P_z (non-equilibrium, imposed P_z). As P_z gets stronger, mixed spin currents occur. For low P_z values (such as $P_z = 0.1 \text{ C/m}^2$ here) we find the current to be completely spin polarized and the down spin polarized currents are almost absent that cannot be plotted in the vertical log axis.

The relative difference in the magnetization orientation of the electrodes can generate reduction in current magnitudes but such effects are due to the subband DOS altered by an externally applied magnetic field, which is the basis for the GMR effect.

2.2 FM/FE/FM with FE having polarization obtained from equation of state

The non-equilibrium homogeneous polarization case was analyzed to provide insight into the spin dependent screening process at the FM electrode interfaces. We now give the results for P_z obtained by solving Eqs. 1.59, 1.82 and 1.83 as well as the charge distribution inside the FM electrodes at zero and finite bias. A multidomain state is highly feasible due to the finite penetration of the electric field into the FM electrodes. However, the asymmetric charge accumulation at the LHS FM/FE appears to be imposing a self-bias on the FE layer. Whether the formation of the single domain state is stable or metastable is a separate phenomena and we take as reference the single domain state yielding results identical to experimental observations with FE TJs. When under bias, identical to the non-equilibrium homogeneous case, FE polarization is assumed to be

fixed, non-responsive to the bias applied on the LHS electrode and only the linear term in Eq. 1.61 is changing in relation to Eq. 1.59. We first spontaneously solve the P_z along with the charge distributions inside the electrodes at zero bias and take this state as reference for further calculations under bias. As expected, a size effect is observed where the value of P_z strongly depends on thickness and the misfit introduced. Two different values of misfit are imposed on the FE layer as these allow us to compare the effect of two different P_z amplitudes and profiles. Although the in-plane component P_x was explicitly taken into account (See Eqs. 1.82 and 1.83), this component converged to zero implying a stable uniaxial FE for both misfit values. The misfit can vary in such structures depending on relaxation processes and defect content and the latter are kept outside the scope as they would seriously complicate the discussion. BaTiO₃ composition was used as a demonstrative case. We noted that the stability of sign of P_z is rather delicate due to the low thickness and the finite screening lengths of the electrodes. In fact, during the numerical solution of the potential, the direction of P_z and, therefore, the spin dependent carrier densities could alternate from left to right or vice versa. To remove this degeneracy condition separated by a low energy barrier in the double-well Landau potential, a small bias (0.01V) was imposed to stabilize the polarization that make it point from the LHS to the RHS electrode for which all discussions are carried out. We note that rather small polarization values are reported for FE TJs due to thickness effects [71, 78, 248], which appears to be in favor of spin polarized tunnelling in FM/FE/FM type stacks as discussed in Sect. 3a due to relatively low electric fields expected at the interfaces. Identical trends in the spin distributions near the interfaces are obtained compared to the homogeneous polarization case with the difference that the near-equilibrium polarization has a curved profile (See Fig. 2.8). The inhomogeneous profile of P_z impacts the way dipoles terminate at the interfaces and has some influence on the interface carrier densities on the FM electrodes but does not change the physics discussed in the previous section.

Overall, the qualitative behavior of the FE TJ with equilibrium inhomogeneous polarization is the same as that of the homogeneous non-equilibrium polarization, making the discussion in the previous section applicable here, too. Small polarization values in the FE allow easier tunnelling and spin mixing at the interface from which tunnelling occurs is absent at small bias. For relatively weak polarization, the distance between the turning points which we take as reference for barrier width to carry out the WKB calculations for the spin channels is also shorter as the field penetration into the LHS

electrode is small. FE polarization determines the carrier accumulation/depletion at the interfaces and a bias (applied on the LHS FM electrode) does not change the qualitative picture. Large bias that exceed the portions of the FE barrier profile in absolute value have been kept outside the scope of this work as the WKB calculations enter a different regime where $qV - E > 0$. Experimentally, however, one should expect the tunneling currents to follow the same trend as for the case $qV - E < 0$ considered here where the loss of the spin polarization is already demonstrated.

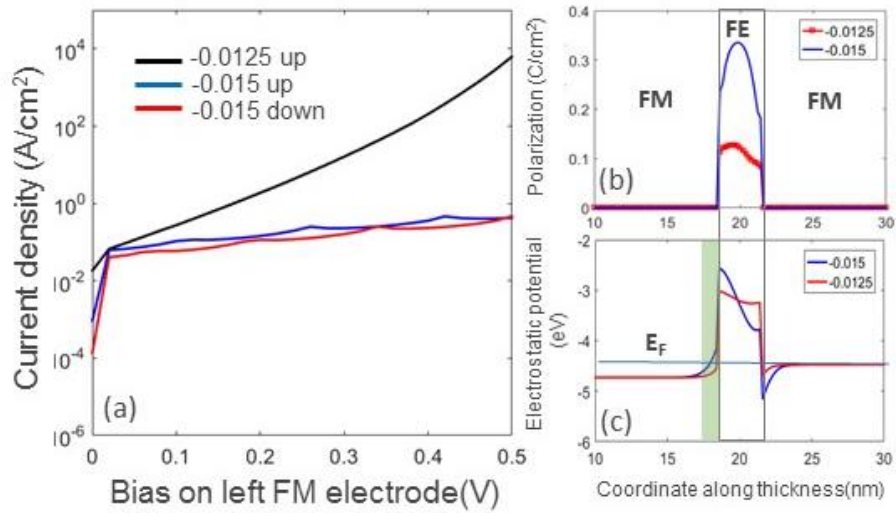


Figure 2.8 Tunneling currents for minority and majority spins calculated using the WKB approximation for values of P_z obtained from equations of state for 2 different misfit strains, (b) the P_z profiles across the thickness of the FE and (c) the profile of the barrier obtained by superimposing the solution of \emptyset on the conduction band profiles of the stack. The shaded area on the LHS of the FM/FE interface denotes the region of carrier depletion, increasing effective barrier thickness.

3 Conclusions

In this work, we numerically studied the spin dependent screening process of FE polarization in FM/FE/FM TJs that are currently of interest for TMR-type devices and spintronics. Parallel magnetization of both FM electrodes was assumed. We demonstrated that the spin population at the interfaces is a strong function of the FE polarization and the applied bias on the system. The dependence of the TMR effect on FE polarization is an intrinsic response of the FM/FE/FM system and directly influences the states between which tunnelling occurs before considering any defect mediated spin flips and magnon-driven processes. With increasing values of FE polarization either due to the inherent composition of the FE or due to external bias, conservation of majority spin density at the interfaces becomes difficult, making spin-mixing inevitable. This occurs due to the need of the system to screen the FE polarization charges and reduce electrostatic energy. To fulfill this need, the majority and minority spin subband LAS near the Fermi level at the interfaces change to allow higher carrier population to be accommodated. This outcome is in excellent qualitative agreement with previous first principles results: The subband LDOS in Fe 3d band at the interface changes in favor of minority spins and decrease slightly for majority spins (with respect to bulk) when FE polarization points towards this interface. Our work thus provides an intuitive understanding of the dramatic effect of local electrostatic effects of the FE polarization on LDOS. While it could very well be said that FE polarization allows magnetization control along the FM interface, whether a strong FE behavior is desired for TMR device design is questionable. As we write this, we keep in mind that a great variety of results have been reported in literature for FE junctions in TMR studies but a general understanding of the trends in these systems is still lacking. Various FE compositions studied as TJs in TMR stacks are probably one cause of this lack of understanding: experimental results as a function of “FE polarization strength” can vary greatly as we show here. In fact, we explicitly reveal here that any parameter inducing strong electric fields at the interfaces will lead to spin mixing at the interfaces, hence a reduction in TMR. We were also able to, therefore, demonstrate the connection between the spin dependent screening process at FE/FM interfaces and the variations of the TMR effect when under bias in such structures.

4 Future Work

Additional works will be conducted in the perspective of antiparallel alignment of ferromagnets. These results may have already published as theoretical and experimental works to the scientific community, still have shaded areas about the electrostatics point of view. In our work, we focused on tunneling in parallel alignment of ferromagnetic electrodes where the density of states of majority spin electrons favor the spin-dependent tunneling, although under increasing ferroelectric strength and bias, spin mixing is observed and spin-selective tunneling probability has decreased upon the calculations. For antiparallel state, we will also try to investigate the probability of tunneling and local density of states for minority and majority spins depending on antiparallel states of ferromagnetic electrode between ferroelectric barrier. These results also may show the tunneling magnetoresistance (TMR) of FM/FE/FM tunnel junctions. Local opposite ferroelectric and ferromagnetic states elucidate the four state multiferroic device principle.

Multiferroic FET (field effect transistor) designs which are composed of diluted magnetic semiconductor (such as GaMnAs) as conducting channels in ferroelectric-gated FET structure. In this system, Mn doped GaAs acts as both p-type semiconductor and diluted magnetic material. The control of ferromagnetism with ferroelectric gate or spin polarized gate control will also be analyzed in the light of information obtained in the context of this thesis.

A detailed study would focus on the idea that the order of magnetic spins and ferroelectric dipoles might have circular or toroidal geometry in circular capacitors. Although, this vortex domain-prediction for ferromagnets dates back to 1940s, there are limited theoretical and experimental works about vortex domains of ferroelectrics. These toroidal ferroelectric domains are sensitive to size effect and boundary conditions and magnetoelectric coupling in multiferroics. Toroidal domains of ferroelectrics are stable for microseconds and these domains has stability issues against decays under the certain conditions which are different from $\nabla \times D = 0$. Although the vortex domains have short life-time (<1 second), this time period is orders of magnitude longer than when it is compared with ferroelectric domain formation. Using Landau-Ginzburg thermodynamic theory, the relation between in-plane and out-of-plane domain structures of these ferroelectrics under the bias will be evaluated within the scope of local defects and

differing boundary conditions. Pseudo-spin characteristics of ferroelectrics also might be investigated upon the scope of this work. This work also may pave the way of analysis of natural multiferroics through the continuum equations in continuum media. Understanding the multiferroic tunnel junctions might strengthen the capability of tailoring of their properties which along with improvements on stability and reliability can lead to performing multifunctional spintronic devices.

References

1. Anderson, P.W., *More Is Different*. Science, 1972. **177**(4047): p. 393.
2. Bardeen, J. and W.H. Brattain, *The transistor, a semi-conductor triode*. Physical Review, 1948.
3. Bardeen, J. and W.H. Brattain, *Physical principles involved in transistor action*. Physical Review, 1949.
4. Noyce, R.N., *Semiconductor Device-and-Lead Structure, Reprint of U.S. Patent 2,981,877 (Issued April 25, 1961. Filed July 30, 1959)*. IEEE Solid-State Circuits Newsletter. **12**(2): p. 34-40.
5. Kilby, J.S., *Miniaturized electronic circuits*. USP3, 1964.
6. Burks, A.W., H.H. Goldstine, and J. Von Neumann, *Preliminary discussion of the logical design of an electronic computer instrument*. 1946, Inst. Adv. Study.
7. Hilbert, M. and P. López, *The World's Technological Capacity to Store, Communicate, and Compute Information*. Science, 2011. **332**(6025): p. 60-65.
8. Dragland(SINTEF), A. *Big data for better or worse*:. 2013 [cited 2017 September 4]; Report]. Available from: <https://www.sciencedaily.com/releases/2013/05/130522085217.htm>.
9. Moore, G.E., *Cramming more components onto integrated circuits, Reprinted from Electronics, volume 38, number 8, April 19, 1965, pp. 114 ff*. IEEE Solid-State Circuits Society Newsletter, 2006.
10. Moore, G.E., *Progress in digital integrated electronics*. Electron Devices Meeting, 1975.
11. Thompson, S.E. and S. Parthasarathy, *Moore's law: the future of Si microelectronics*. Materials today, 2006.
12. Lloyd, S., *Ultimate physical limits to computation*. Nature, 2000. **406**(6799): p. 1047-1054.
13. Zhirnov, V.V., et al., *Limits to Binary Logic Switch Scaling—A Gedanken Model*. Proceedings of the IEEE, 2003. **91**(11): p. 1934-1939.
14. Meindl, J.D., Q. Chen, and J.A. Davis, *Limits on Silicon Nanoelectronics for Terascale Integration*. Science, 2001. **293**(5537): p. 2044-2049.
15. Lundstrom, M., *Moore's Law Forever?* Science, 2003.
16. *Comparing Technologies:MRAM vs. FRAM*, E. Technologies, Editor. 2013.
17. Cano, A. and A. Levanyuk, *Pseudoproper ferroelectricity in thin films*. Physical Review B, 2010. **81**(17): p. 172105.

18. Arimoto, Y. and H. Ishiwara, *Current Status of Ferroelectric Random-Access Memory*. MRS Bulletin, 2004. **29**(11): p. 823-828.
19. Wang, K.L., J.G. Alzate, and K.P. Amiri, *Low-power non-volatile spintronic memory: STT-RAM and beyond*. Journal of Physics D: Applied Physics, 2013. **46**(7): p. 74003.
20. Wang, K.L., H. Lee, and P. Amiri, *Magnetolectric Random Access Memory-Based Circuit Design by Using Voltage-Controlled Magnetic Anisotropy in Magnetic Tunnel Junctions*. IEEE Transactions on Nanotechnology, 2015. **14**(6): p. 992-997.
21. Yang, J.J., D.B. Strukov, and D.R. Stewart, *Memristive devices for computing*. Nature Nanotechnology, 2012. **8**(1): p. 13-24.
22. Kent, A.D. and D.C. Worledge, *A new spin on magnetic memories*. Nature Nanotechnology, 2015. **10**: p. 187.
23. Pauli, W., *Über den Zusammenhang des Abschlusses der Elektronengruppen im Atom mit der Komplexstruktur der Spektren*. Zeitschrift für Physik A Hadrons and Nuclei, 1925.
24. Hund, F., *Linienspektren Und Periodisches System der Elemente*. 1927, Berlin: Julius Springer.
25. Chikazumi, S., *Physics of Ferromagnetism*. International Series Of Monographs On Physics, ed. S.F.E. J. Birman, R. Friend, C. H. Llewellyn Smith, M. Rees, D. Sherrington, G. Veneziano. Vol. 94. 1997, New York: Oxford University Press.
26. Baibich, M.N., et al., *Giant Magnetoresistance of (001)Fe/(001)Cr Magnetic Superlattices*. Physical Review Letters, 1988. **61**(21): p. 2472.
27. Binasch, G., et al., *Enhanced magnetoresistance in layered magnetic structures with antiferromagnetic interlayer exchange*. Physical Review B, 1989. **39**(7): p. 4828.
28. Julliere, M., *Tunneling between ferromagnetic films*. Physics Letters A, 1975. **54**(3): p. 225-226.
29. Miyazaki, T. and N. Tezuka, *Giant magnetic tunneling effect in Fe/Al₂O₃/Fe junction*. Journal of Magnetism and Magnetic Materials, 1995.
30. Moodera, J.S., et al., *Large Magnetoresistance at Room Temperature in Ferromagnetic Thin Film Tunnel Junctions*. Physical Review Letters, 1995. **74**(16): p. 3273-3276.
31. Mott, N.F., *The electrical conductivity of transition metals*. Proc. Roy. Soc. A., 1936. **47**: p. 699-718.
32. Datta, S. and B. Das, *Electronic analog of the electro-optic modulator*. Applied Physics Letters, 1990. **56**(7): p. 665-667.

33. Chappert, C., A. Fert, and F. Dau, *The emergence of spin electronics in data storage*. Nature Materials, 2007. **6**(11): p. 813-823.
34. Parkin, S.S.P., et al., *Giant tunnelling magnetoresistance at room temperature with MgO (100) tunnel barriers*. Nature Materials, 2004. **3**: p. 862.
35. Yuasa, S., et al., *High Tunnel Magnetoresistance at Room Temperature in Fully Epitaxial Fe/MgO/Fe Tunnel Junctions due to Coherent Spin-Polarized Tunneling*. Japanese Journal of Applied Physics, 2004. **43**(4B): p. L588.
36. Ikeda, S., J. Hayakawa, and Y. Ashizawa, *Tunnel magnetoresistance of %604 at 300 K by suppression of Ta diffusion in CoFeB/MgO/CoFeB pseudo-spin-valves annealed at high temperature* Applied Physics Letters, 2008. **93**.
37. Lu, Y., et al., *Large magnetotunneling effect at low magnetic fields in micrometer-scale epitaxial $\text{La}_{0.67}\text{Sr}_{0.33}\text{MnO}_3$ tunnel junctions*. Physical Review B, 1996. **54**(12): p. R8357-R8360.
38. Sun, J.Z., et al., *Observation of large low-field magnetoresistance in trilayer perpendicular transport devices made using doped manganate perovskites*. Applied Physics Letters, 1996. **69**(21): p. 3266-3268.
39. Sun, J., et al., *Temperature dependent, non-ohmic magnetoresistance in doped perovskite manganate trilayer junctions*. Applied physics letters, 1997. **70**(13): p. 1769-1771.
40. Zhu, J.-G. and C. Park, *Magnetic tunnel junctions*. Materials Today, 2006. **9**(11): p. 36-45.
41. Viret, M., et al., *Low-field colossal magnetoresistance in manganite tunnel spin valves*. EPL (Europhysics Letters), 1997. **39**(5): p. 545.
42. Sun, J.Z., et al., *Temperature and bias dependence of magnetoresistance in doped manganite thin film trilayer junctions*. Applied Physics Letters, 1998. **73**(7): p. 1008-1010.
43. Bowen, M., et al., *Nearly total spin polarization in $\text{La}_{2/3}\text{Sr}_{1/3}\text{MnO}_3$ from tunneling experiments*. Applied Physics Letters, 2003. **82**(2): p. 233-235.
44. Cuppens, R., P.K. Larsen, and G.A.C.M. Spierings, *Ferroelectrics for non-volatile memories*. Microelectronic Engineering, 1992. **19**(1): p. 245-252.
45. Valasek, J., *Piezoelectric And Allied Phenomena In Rochelle Salt*. The Physical Review, 1920. **15**: p. 537-538.
46. *Physics of Ferroelectrics : A Modern Perspective*. Topics in Applied Physics. Vol. 105. 2007, Berlin Heidelberg: Springer-Verlag
47. Esaki, L., R. Laibowitz, and P. Stiles, *Polar switch*. IBM Tech. Discl. Bull, 1971. **13**(2161): p. 114.

48. Contreras, J.R.g., et al., *Resistive switching in metal–ferroelectric–metal junctions*. Applied Physics Letters, 2003. **83**(22): p. 4595-4597.
49. Garcia, V., et al., *Ferroelectric Control of Spin Polarization*. Science, 2010. **327**(5969): p. 1106-1110.
50. Pantel, D., et al., *Reversible electrical switching of spin polarization in multiferroic tunnel junctions*. Nature Materials, 2012. **11**: p. 289.
51. Bocher, L., et al., *Atomic and Electronic Structure of the BaTiO₃/Fe Interface in Multiferroic Tunnel Junctions*. Nano Letters, 2012. **12**(1): p. 376-382.
52. Yin, Y.W., et al., *Enhanced tunnelling electroresistance effect due to a ferroelectrically induced phase transition at a magnetic complex oxide interface*. Nature Materials, 2013. **12**: p. 397.
53. Jiang, L., et al., *Tunneling Electroresistance Induced by Interfacial Phase Transitions in Ultrathin Oxide Heterostructures*. Nano Letters, 2013. **13**(12): p. 5837-5843.
54. Garcia, V., et al., *Giant tunnel electroresistance for non-destructive readout of ferroelectric states*. Nature, 2009. **460**: p. 81.
55. Maksymovych, P., et al., *Polarization Control of Electron Tunneling into Ferroelectric Surfaces*. Science, 2009. **324**(5933): p. 1421-1425.
56. Gruverman, A., et al., *Tunneling Electroresistance Effect in Ferroelectric Tunnel Junctions at the Nanoscale*. Nano Letters, 2009. **9**(10): p. 3539-3543.
57. Crassous, A., et al., *Giant tunnel electroresistance with PbTiO₃ ferroelectric tunnel barriers*. Applied Physics Letters, 2010. **96**(4): p. 042901.
58. Gao, X.S., et al., *Nanoscale ferroelectric tunnel junctions based on ultrathin BaTiO₃ film and Ag nanoelectrodes*. Applied Physics Letters, 2012. **101**(14): p. 142905.
59. Pantel, D., et al., *Room-Temperature Ferroelectric Resistive Switching in Ultrathin Pb(Zr_{0.2}Ti_{0.8})O₃ Films*. ACS Nano, 2011. **5**(7): p. 6032-6038.
60. Kim, D.J., et al., *Ferroelectric Tunnel Memristor*. Nano Letters, 2012. **12**(11): p. 5697-5702.
61. Chanthbouala, A., et al., *Solid-state memories based on ferroelectric tunnel junctions*. Nature Nanotechnology, 2011. **7**: p. 101.
62. Chanthbouala, A., et al., *A ferroelectric memristor*. Nature Materials, 2012. **11**: p. 860.
63. Pantel, D., et al., *Tunnel electroresistance in junctions with ultrathin ferroelectric Pb(Zr_{0.2}Ti_{0.8})O₃ barriers*. Applied Physics Letters, 2012. **100**(23): p. 232902.

64. Kim, D.J., et al., *Retention of resistance states in ferroelectric tunnel memristors*. Applied Physics Letters, 2013. **103**(14): p. 142908.
65. Soni, R., et al., *Giant electrode effect on tunnelling electroresistance in ferroelectric tunnel junctions*. Nature Communications, 2014. **5**: p. 5414.
66. Garcia, V. and M. Bibes, *Ferroelectric tunnel junctions for information storage and processing*. Nature Communications, 2014. **5**: p. 4289.
67. Wen, Z., et al., *Ferroelectric-field-effect-enhanced electroresistance in metal/ferroelectric/semiconductor tunnel junctions*. Nature materials, 2013. **12**(7): p. 617-621.
68. Bune, A.V., et al., *Two-dimensional ferroelectric films*. Nature, 1998. **391**: p. 874.
69. Rabe, K.M., C.H. Ahn, and J.-M. Triscone, *Physics of Ferroelectrics A Modern Perspective*. Topics In Applied Physics. Vol. 105. Berlin, Heidelberg: Springer.
70. Ahn, C.H., K.M. Rabe, and J.-M. Triscone, *Ferroelectricity at the Nanoscale: Local Polarization in Oxide Thin Films and Heterostructures*. Science, 2004. **303**(5657): p. 488-491.
71. Junquera, J. and P. Ghosez, *Critical thickness for ferroelectricity in perovskite ultrathin films*. Nature, 2003. **422**: p. 506.
72. Kim, Y.S., et al., *Critical thickness of ultrathin ferroelectric BaTiO₃ films*. Applied Physics Letters, 2005. **86**(10): p. 102907.
73. Yamada, H., et al., *Giant Electroresistance of Super-tetragonal BiFeO₃-Based Ferroelectric Tunnel Junctions*. ACS Nano, 2013. **7**(6): p. 5385-5390.
74. Boyn, S., et al., *High-performance ferroelectric memory based on fully patterned tunnel junctions*. Applied Physics Letters, 2014. **104**(5): p. 052909.
75. Wang, L., et al., *Overcoming the Fundamental Barrier Thickness Limits of Ferroelectric Tunnel Junctions through BaTiO₃/SrTiO₃ Composite Barriers*. Nano Letters, 2016. **16**(6): p. 3911-3918.
76. Bruno, F.Y., et al., *Millionfold Resistance Change in Ferroelectric Tunnel Junctions Based on Nickelate Electrodes*. Advanced Electronic Materials, 2016. **2**(3): p. 1500245-n/a.
77. Tsybal, E.Y. and H. Kohlstedt, *Tunneling across a ferroelectric*. Science, 2006. **313**(5784): p. 181-183.
78. Garcia, V., et al., *Giant tunnel electroresistance for non-destructive readout of ferroelectric states*. Nature, 2009. **460**(7251): p. 81-84.
79. Gruverman, A., et al., *Tunneling electroresistance effect in ferroelectric tunnel junctions at the nanoscale*. Nano letters, 2009. **9**(10): p. 3539-3543.

80. Zhuravlev, M.Y., et al., *Giant electroresistance in ferroelectric tunnel junctions*. Physical Review Letters, 2005. **94**(24): p. 246802.
81. Maksymovych, P., et al., *Ultrathin limit and dead-layer effects in local polarization switching of BiFeO_3* . Physical Review B, 2012. **85**(1): p. 014119.
82. Watanabe, Y., *Theoretical stability of the polarization in a thin semiconducting ferroelectric*. Physical Review B, 1998. **57**(2): p. 789-804.
83. Hideharu, M., *Calculation of band bending in ferroelectric semiconductor*. New Journal of Physics, 2000. **2**(1): p. 8.
84. Blom, P.W.M., et al., *Ferroelectric Schottky Diode*. Physical Review Letters, 1994. **73**(15): p. 2107-2110.
85. Ashcroft, N.W. and N.D. Mermin, *Solid State Physics*. USA: Thomson Learning Inc.
86. Bratkovsky, A.M. and A.P. Levanyuk, *Abrupt Appearance of the Domain Pattern and Fatigue of Thin Ferroelectric Films*. Physical Review Letters, 2000. **84**(14): p. 3177-3180.
87. Levanyuk, A.P. and I.B. Misirlioglu, *Phase transitions in ferroelectric-paraelectric superlattices: Stability of single domain state*. Applied Physics Letters, 2013. **103**(19): p. 192906.
88. Chenskii, E.V. and V.V. Tarasenko, *Theory of phase transitions into inhomogeneous states in organic ferroelectrics in an external electric field* Sov. Phys. JETP, 1982. **56**(3): p. 618-623.
89. Stephanovich, V.A., I.A. Luk'yanchuk, and M.G. Karkut, *Domain-Enhanced Interlayer Coupling in Ferroelectric/Paraelectric Superlattices*. Physical Review Letters, 2005. **94**(4): p. 047601.
90. Levanyuk, A.P. and I.B. Misirlioglu, *Phase transitions in ferroelectric-paraelectric superlattices*. Journal of Applied Physics, 2011. **110**(11): p. 114109.
91. Levanyuk, A. and I. Misirlioglu, *Phase transitions in ferroelectric-paraelectric superlattices: Stability of single domain state*. Applied Physics Letters, 2013. **103**(19): p. 192906.
92. Kretschmer, R. and K. Binder, *Surface effects on phase transitions in ferroelectrics and dipolar magnets*. Physical Review B, 1979. **20**(3): p. 1065-1076.
93. Scott, J.F., et al., *Properties of ceramic KNO_3 thin-film memories*. Physica B+C, 1988. **150**(1): p. 160-167.
94. Tilley, D.R. and B. Zeks, *TfC23. Phase transitions in ferroelectric films*. Ferroelectrics, 1992. **134**(1): p. 313-318.

95. Zhong, W.L., et al., *Thickness dependence of the dielectric susceptibility of ferroelectric thin films*. Physical Review B, 1994. **50**(17): p. 12375-12380.
96. Baudry, L. and J. Tournier, *Lattice model for ferroelectric thin film materials including surface effects: Investigation on the “depolarizing” field properties*. Journal of Applied Physics, 2001. **90**(3): p. 1442-1454.
97. Shaoping, L., et al., *Dimension and Size Effects in Ferroelectrics*. Japanese Journal of Applied Physics, 1997. **36**(8R): p. 5169.
98. Sai, N., A.M. Kolpak, and A.M. Rappe, *Ferroelectricity in ultrathin perovskite films*. Physical Review B, 2005. **72**(2): p. 020101.
99. Tagantsev, A.K., G. Gerra, and N. Setter, *Short-range and long-range contributions to the size effect in metal-ferroelectric-metal heterostructures*. Physical Review B, 2008. **77**(17): p. 174111.
100. Lichtensteiger, C., et al., *Ferroelectricity in Ultrathin-Film Capacitors*, in *Oxide Ultrathin Films: Science and Technology*, G. Pacchioni and S. Valeri, Editors. 2012, Wiley-VCH Verlag GmbH & Co. KGaA: Weinheim, Germany.
101. Kohlstedt, H., N.A. Pertsev, and R. Waser, *Size Effects on Polarization in Epitaxial Ferroelectric Films and the Concept of Ferroelectric Tunnel Junctions Including First Results*. MRS Proceedings, 2011. **688**.
102. Pertsev, N.A., A.G. Zembilgotov, and A.K. Tagantsev, *Effect of Mechanical Boundary Conditions on Phase Diagrams of Epitaxial Ferroelectric Thin Films*. Physical Review Letters, 1998. **80**(9): p. 1988-1991.
103. Pertsev, N.A., A.G. Zembilgotov, and A.K. Tagantsev, *Equilibrium states and phase transitions in epitaxial ferroelectric thin films*. Ferroelectrics, 1999. **223**(1): p. 79-90.
104. Meyer, E., H.J. Hug, and R. Bennewitz, *Introduction to Scanning Tunneling Microscopy*. Advanced Texts in Physics. 2004, Berlin, Heidelberg: Springer-Verlag.
105. Simmons, J.G., *Electric Tunnel Effect between Dissimilar Electrodes Separated by a Thin Insulating Film*. Journal of Applied Physics, 1963. **34**(9): p. 2581-2590.
106. Simmons, J.G., *Generalized Formula for the Electric Tunnel Effect between Similar Electrodes Separated by a Thin Insulating Film*. Journal of Applied Physics, 1963. **34**(6): p. 1793-1803.
107. Brinkman, W.F., R.C. Dynes, and J.M. Rowell, *Tunneling Conductance of Asymmetrical Barriers*. Journal of Applied Physics, 1970. **41**(5): p. 1915-1921.
108. Hlinka, J. and P. Marton, *Phenomenological model of a 90 degrees domain wall in BaTiO₃-type ferroelectrics*. Physical Review B, 2006. **74**(10).

109. Tagantsev, A.K., *Landau Expansion for Ferroelectrics: Which Variable to Use?* Ferroelectrics, 2008. **375**: p. 19-27.
110. Jackson, J.D., *Classical Electrodynamics*. 3 ed. 1999, USA: John Wiley and Sons Inc.
111. Misirlioglu, I.B., M.T. Kesim, and S.P. Alpay, *Strong dependence of dielectric properties on electrical boundary conditions and interfaces in ferroelectric superlattices*. Applied Physics Letters, 2014. **104**(2): p. 022906.
112. Misirlioglu, I.B. and M. Yildiz, *Carrier accumulation near electrodes in ferroelectric films due to polarization boundary conditions*. Journal of Applied Physics, 2014. **116**(2).
113. Glinchuk, M.D., E.A. Eliseev, and V.A. Stephanovich, *The depolarization field effect on the thin ferroelectric films properties*. Physica B-Condensed Matter, 2002. **322**(3-4): p. 356-370.
114. Jia, C.L., et al., *Unit-cell scale mapping of ferroelectricity and tetragonality in epitaxial ultrathin ferroelectric films*. Nature Materials, 2007. **6**(1): p. 64-69.
115. Waser, R., et al., *Redox-based resistive switching memories—nanoionic mechanisms, prospects, and challenges*. Advanced materials, 2009. **21**(25-26): p. 2632-2663.
116. Wong, H.-S.P., et al., *Metal–oxide RRAM*. Proceedings of the IEEE, 2012. **100**(6): p. 1951-1970.
117. Lee, J.S., S. Lee, and T.W. Noh, *Resistive switching phenomena: A review of statistical physics approaches*. Applied Physics Reviews, 2015. **2**(3): p. 031303.
118. Mohammadmoradi, O., et al., *Strong composition dependence of resistive switching in Ba_{1-x}Sr_xTiO₃ thin films on semiconducting substrates and its thermodynamic analysis*. Acta Materialia, 2018. **148**: p. 419-431.
119. Zhuravlev, M.Y., et al., *Ferroelectric switch for spin injection*. Applied Physics Letters, 2005. **87**(22): p. 222114.
120. Velez, J.P., et al., *Magnetic tunnel junctions with ferroelectric barriers: prediction of four resistance states from first principles*. Nano Letters, 2008. **9**(1): p. 427-432.
121. Zenkevich, A., et al., *Electronic band alignment and electron transport in Cr/BaTiO₃/Pt ferroelectric tunnel junctions*. Applied Physics Letters, 2013. **102**(6): p. 062907.
122. Lu, H., et al., *Ferroelectric tunnel junctions with graphene electrodes*. Nature Communications, 2014. **5**: p. 5518.
123. Singh, A.V., et al., *Junction size dependence of ferroelectric properties in e-beam patterned BaTiO₃ ferroelectric tunnel junctions*. Applied Physics Letters, 2015. **107**(12): p. 122903.

124. Radaelli, G., et al., *Large Room-Temperature Electroresistance in Dual-Modulated Ferroelectric Tunnel Barriers*. *Advanced Materials*, 2015. **27**(16): p. 2602-2607.
125. Chernikova, A., et al., *Ultrathin Hf_{0.5}Zr_{0.5}O₂ Ferroelectric Films on Si*. *ACS Applied Materials & Interfaces*, 2016. **8**(11): p. 7232-7237.
126. Tsymbal, E.Y. and J.P. Velev, *Crossing the wall*. *Nature Nanotechnology*, 2017. **12**: p. 614.
127. Ambriz-Vargas, F., et al., *A Complementary Metal Oxide Semiconductor Process-Compatible Ferroelectric Tunnel Junction*. *ACS Applied Materials & Interfaces*, 2017. **9**(15): p. 13262-13268.
128. Röntgen, W.C., *Ueber die durch Bewegung eines im homogenen elektrischen Felde befindlichen Dielectricums hervorgerufene electrodynamische Kraft*. *Annalen der Physik*, 1888. **271**(10): p. 264-270.
129. Debye, P., *Bemerkung zu einigen neunten Versuchen über einen magneto-elektrischen Richteffekt*. *Zeitschrift für Physik*, 1926. **36**(4): p. 300-301.
130. Landau, L.D., *Collected Papers of L.D. Landau*, ed. D.T. Haar. 1965: Pergamon.
131. Landau, L.D. and E.M. Lifshitz, *Statistical Physics*. 1969: Addison-Wesley/Pergamon
132. Dzyaloshinskii, I.E., *On The Magneto-Electrical Effect In AntiFerromagnets*. *Journal of Experimental and Theoretical Physics*, 1959. **37**(3): p. 881-882.
133. Astrov, D.N., *The Magnetolectric Effect In Antiferromagnetics*. *Soviet Physics Journal of Experimental and Theoretical Physics*, 1960. **11**(3): p. 708-709.
134. Astrov, D.N., *Magnetolectric Effect In Chromium Oxide*. *Soviet Physics Journal of Experimental and Theoretical Physics*, 1960. **13**(4): p. 729-733.
135. Aizu, K., *Determination of the State Parameters and Formulation of Spontaneous Strain for Ferroelastics*. *Journal of the Physical Society of Japan*, 1970. **28**(3): p. 706-728.
136. Aizu, K., *Possible Species of "Ferroelastic" Crystals and of Simultaneously Ferroelectric and Ferroelastic Crystals*. *Journal of the Physical Society of Japan*, 1969. **27**: p. 387-396.
137. Khomskii, D.I., *Multiferroics: Different ways to combine magnetism and ferroelectricity*. *Journal of Magnetism and Magnetic Materials*, 2000. **306**(29): p. 8.
138. Hill, N.A., *Why Are There so Few Magnetic Ferroelectrics?* *J. Phys. Chem. B*, 2000. **104**: p. 16.
139. Fox, D.L. and J.F. Scott, *Ferroelectrically Induced Ferromagnetism*. *Journal of Physics C: Solid State Physics*, 1977. **10**: p. L329-L331.

140. Schmid, H., *Multi-Ferroic Magnetolectrics*. *Ferroelectrics*, 1994. **162**: p. 317-338.
141. Loidl, A., H. Loehneysen, and M. Kalvius, *PREFACE-Multiferroics*. *Journal Of Physics: Condensed Matter*, 2008. **20**: p. 1-2.
142. Ascher, E., et al., *Some Properties of Ferromagnetolectric Nickel-Iodine Boracite, Ni₃B₇O₁₃I*. *Journal of Applied Physics*, 1966. **37**: p. 1404-1405.
143. Hur, N., et al., *Electric polarization reversal and memory in a multiferroic material induced by magnetic fields*. *Nature*, 2004. **429**(6990): p. 392-395.
144. Kimura, T., et al., *Magnetic control of ferroelectric polarization*. *Nature*, 2003. **426**(6962): p. 55-58.
145. Van Aken, B.B., et al., *The origin of ferroelectricity in magnetolectric YMnO₃*. 2004. **3**: p. 164.
146. Lawes, G., et al., *Magnetically Driven Ferroelectric Order in Ni₃V₂O₈*. *Physical Review Letters*, 2005. **95**(8): p. 087205.
147. Spaldin, N.A. and M. Fiebig, *The Renaissance of Magnetolectric Multiferroics*. *Science*, 2005. **309**(5733): p. 391-392.
148. Wang, J., et al., *Epitaxial BiFeO₃ Multiferroic Thin Film Heterostructures*. *Science*, 2003. **299**: p. 5.
149. Eerenstein, E., et al., *Comment on "Epitaxial BiFeO₃ Multiferroic Thin Film Heterostructures"*. *Science*. **307**(5713): p. 1203-1204.
150. Khodabakhsh, M., et al., *Strong smearing and disappearance of phase transitions into polar phases due to inhomogeneous lattice strains induced by A-site doping in Bi_{1-x}A_xFeO₃ (A: La, Sm, Gd)*. *Journal of Alloys and Compounds*, 2014. **604**: p. 117-130.
151. Fischer, P., et al., *Temperature dependence of the crystal and magnetic structures of BiFeO₃*. *J. Phys. C: Solid State Phys.* . **13**: p. 1931-1940.
152. Selbach, S.M., et al., *The Ferroic Phase Transitions of BiFeO₃*. *Advanced Materials*, 2008. **20**(19): p. 3692–3696.
153. Pantel, D., et al., *Switching kinetics in epitaxial BiFeO₃ thin films*. *Journal of Applied Physics*, 2010. **107**(8): p. 084111.
154. Li, J., et al., *Dramatically enhanced polarization in (001), (101), and (111) BiFeO₃ thin films due to epitaxial-induced transitions*. *Applied Physics Letters*, 2004. **84**(25): p. 5261-5263.
155. Zhao, T., et al., *Electrical control of antiferromagnetic domains in multiferroic BiFeO₃ films at room temperature*. *Nat Mater*, 2006. **5**(10): p. 823-829.

156. Selbach, S.M., et al., *Phase transitions, electrical conductivity and chemical stability of BiFeO₃ at high temperatures*. Journal of Solid State Chemistry, 2010. **183**(5): p. 1205-1208.
157. Arnold, D.C., et al., *Ferroelectric-Paraelectric Transition in BiFeO₃: Crystal Structure of the Orthorhombic Phase*. Physical Review Letters 2009. **102**: p. 027602-1-4.
158. Catalan, G. and J.F. Scott, *Physics and Applications of Bismuth Ferrite*. Advanced Materials, 2009. **21**: p. 2463-2485.
159. Sosnowska, I., T.P. Neumaier, and E. Steichele, *Spiral magnetic ordering in bismuth ferrite*. Journal of Physics C: Solid State Physics, 1982. **15**: p. 4835-4846.
160. Yang, J.C., et al., *Orthorhombic BiFeO₃*. Physical Review Letters, 2012. **109**: p. 5.
161. Lebeugle, D., et al., *Electric Field Switching of the Magnetic Anisotropy of a Ferromagnetic Layer Exchange Coupled to the Multiferroic Compound BiFeO₃*. Physical Review Letters, 2009. **103**(25): p. 257601.
162. Troyanchuk, I.O., et al., *Phase Transitions, Magnetic and Piezoelectric Properties of Rare-Earth-Substituted BiFeO₃ Ceramics*. Journal of the American Ceramic Society, 2011. **94**(12): p. 4502-4506.
163. H. Béa, M.G., M. Bibes, and A. Barthélémy, *Spintronics with multiferroics*. Journal of Physics: Condensed Matter, 2008. **20**(43): p. 11.
164. L W Martin, S.P.C., Y-H Chu, M B Holcomb, M Gajek, M Huijben, C-H Yang, N Balke and R Ramesh, *Multiferroics and magnetoelectrics: thin films and nanostructures*. Journal Of Physics: Condensed Matter, 2008. **20**: p. 13.
165. Khomskii, D., *Classifying multiferroics: Mechanisms and effects*. Physics, 2009. **2**(20).
166. Cheong, S.-W. and M. Mostovoy, *Multiferroics: a magnetic twist for ferroelectricity*. Nat Mater, 2007. **6**(1): p. 13-20.
167. Rao, C.N.R., et al., *Charge ordering in the rare earth manganates: the experimental situation*. Journal of Physics: Condensed Matter, 2000. **12**(7): p. R83.
168. Zhang, T. and M. Dressel, *Grain-size effects on the charge ordering and exchange bias in Pr_{0.5}Ca_{0.5}MnO₃: The role of spin configuration*. Physical Review B, 2009. **80**(1): p. 014435.
169. Mizokawa, T., D.I. Khomskii, and S.G. A., *Spin and charge ordering in self-doped Mott insulators*. Physical Review B, 2008. **61**: p. 11263-11266.

170. García-Muñoz, J.L., et al., *Neutron-diffraction study of $RNiO_3$ ($R=La, Pr, Nd, Sm$): Electronically induced structural changes across the metal-insulator transition*. Physical Review B, 1992. **46**(8): p. 4414-4425.
171. Sergienko, I.A., C. Sen, and E. Dagotto, *Ferroelectricity in the Magnetic E-Phase of Orthorhombic Perovskites*. Physical Review Letters 2006. **97**: p. 227204-1-4.
172. Choi, Y.J., et al., *Ferroelectricity in an Ising Chain Magnet*. Physical Review Letters, 2008. **100**: p. 047601-1-4.
173. Brown, W.F., R.M. Hornreich, and S. Shtrikman, *Upper Bound on the Magnetoelectric Susceptibility*. Physical Review, 1968. **168**(2): p. 574-577.
174. Tabares-Munoz, C., et al., *Measurement of the Quadratic Magnetoelectric Effect on Single Crystalline $BiFeO_3$* . Japanese Journal of Applied Physics, 1985. **24**: p. 1051-053.
175. Fiebig, M., et al., *Observation of coupled magnetic and electric domains*. Nature, 2002. **419**(6909): p. 818-820.
176. Nan, C.-W., *Magnetoelectric effect in composites of piezoelectric and piezomagnetic phases*. Physical Review B, 1994. **50**(9): p. 6082-6088.
177. Lou, J., et al., *Giant Electric Field Tuning of Magnetism in Novel Multiferroic $FeGaB/Lead$ Zinc Niobate–Lead Titanate (PZN-PT) Heterostructures*. Advanced Materials, 2009. **21**(46): p. 4711-4715.
178. Bur, A., et al., *Giant electric-field-induced reversible and permanent magnetization reorientation on magnetoelectric $Ni/(011) [Pb(Mg_{1/3}Nb_{2/3})O_3](1-x)-[PbTiO_3]x$ heterostructure*. Applied Physics Letters, 2011. **98**(1): p. 012504.
179. Jungho, R., et al., *Magnetoelectric Properties in Piezoelectric and Magnetostrictive Laminate Composites*. Japanese Journal of Applied Physics, 2001. **40**(8R): p. 4948.
180. Liu, M., et al., *Giant Electric Field Tuning of Magnetic Properties in Multiferroic Ferrite/Ferroelectric Heterostructures*. Advanced Functional Materials, 2009. **19**(11): p. 1826-1831.
181. Zheng, H., et al., *Multiferroic $BaTiO_3-CoFe_2O_4$ Nanostructures*. Science, 2004. **303**(5658): p. 661-663.
182. Eerenstein, W., et al., *Giant sharp and persistent converse magnetoelectric effects in multiferroic epitaxial heterostructures*. Nat Mater, 2007. **6**(5): p. 348-351.
183. Venkataiah, G., et al., *Manipulation of magnetic coercivity of Fe film in $Fe/BaTiO_3$ heterostructure by electric field*. Applied Physics Letters, 2011. **99**: p. 102506-1-102506-4.

184. Zakharov, A.I., et al., *Magnetic And Magnetoelastic Properties Of A Metamagnetic Iron-Rhodium Alloy* Soviet Physics Journal of Experimental and Theoretical Physics, 1964. **19**(6): p. 1348-1353.
185. Yuasa, S., H. Miyajima, and Y. Otani, *Magneto-Volume and Tetragonal Elongation Effects on Magnetic Phase Transitions of Body-Centered Tetragonal FeRh_{1-x}Ptx*. Journal of the Physical Society of Japan, 1994. **63**(8): p. 3129-3144.
186. Suzuki, I., M. Itoh, and T. Taniyama, *Elastically controlled magnetic phase transition in Ga-FeRh/BaTiO₃(001) heterostructure*. Applied Physics Letters, 2014. **104**(2): p. 022401.
187. Phillips, L.C., et al., *Local electrical control of magnetic order and orientation by ferroelastic domain arrangements just above room temperature*. 2015. **5**: p. 10026.
188. Cherifi, R.O., et al., *Electric-field control of magnetic order above room temperature*. Nat Mater, 2014. **13**(4): p. 345-351.
189. Meiklejohn, W.H. and C.P. Bean, *New Magnetic Anisotropy*. Physical Review, 1957. **105**(3): p. 904-913.
190. Malozemoff, A.P., *Random-field model of exchange anisotropy at rough ferromagnetic-antiferromagnetic interfaces*. Physical Review B, 1987. **35**(7): p. 3679-3682.
191. Nogués, J. and I.K. Schuller, *Exchange bias*. Journal of Magnetism and Magnetic Materials, 1999. **192**(2): p. 203-232.
192. Stamps, R.L., *Mechanisms for exchange bias*. Journal of Physics D: Applied Physics, 2001. **33**(23): p. R247-268.
193. Chu, Y.-H., et al., *Electric-field control of local ferromagnetism using a magnetoelectric multiferroic*. Nat Mater, 2008. **7**(6): p. 478-482.
194. Heron, J.T., et al., *Deterministic switching of ferromagnetism at room temperature using an electric field*. Nature, 2014. **516**(7531): p. 370-373.
195. Duan, C.-G., et al., *Universality of the surface magnetoelectric effect in half-metals*. Physical Review B, 2009. **79**(14): p. 140403.
196. Duan, C.-G., et al., *Surface Magnetoelectric Effect in Ferromagnetic Metal Films*. Physical Review Letters, 2008. **101**(13): p. 137201.
197. Rondinelli, J.M., M. Stengel, and N.A. Spaldin, *Carrier-mediated magnetoelectricity in complex oxide heterostructures*. Nat Nano, 2008. **3**(1): p. 46-50.
198. Niranjana, M.K., et al., *Magnetoelectric effect at the SrRuO₃/BaTiO₃ (001) interface: An ab initio study*. Applied Physics Letters, 2009. **95**(5): p. 052501.

199. Zhang, S., *Spin-Dependent Surface Screening in Ferromagnets and Magnetic Tunnel Junctions*. Physical Review Letters, 1999. **83**(3): p. 640-643.
200. Hammouri, M., E. Fohtung, and I. Vasiliev, *Ab initio study of magnetoelectric coupling in $\text{La}_{0.66}\text{Sr}_{0.33}\text{MnO}_3 / \text{PbZr}_{0.2}\text{Ti}_{0.8}\text{O}_3$ multiferroic heterostructures*. Journal of Physics : Condensed Matter, 2016. **28**: p. 1-8.
201. Burton, J.D. and E.Y. Tsymbal, *Prediction of electrically induced magnetic reconstruction at the manganite/ferroelectric interface*. Physical Review B, 2009. **80**(17): p. 174406.
202. Molegraaf, H.J.A., et al., *Magnetoelectric Effects in Complex Oxides with Competing Ground States*. Advanced Materials, 2009. **21**(34): p. 3470-3474.
203. Vaz, C.A.F., et al., *Control of magnetism in $\text{Pb}(\text{Zr}_{0.2}\text{Ti}_{0.8})\text{O}_3/\text{La}_{0.8}\text{Sr}_{0.2}\text{MnO}_3$ multiferroic heterostructures* Journal of Applied Physics, 2011. **109**(7): p. 07D905.
204. Vaz, C.A.F., et al., *Temperature dependence of the magnetoelectric effect in $\text{Pb}(\text{Zr}_{0.2}\text{Ti}_{0.8})\text{O}_3/\text{La}_{0.8}\text{Sr}_{0.2}\text{MnO}_3$ multiferroic heterostructures*. Applied Physics Letters, 2010. **97**(4): p. 042506.
205. Brivio, S., et al., *Near-room-temperature control of magnetization in field effect devices based on $\text{La}_{0.67}\text{Sr}_{0.33}\text{MnO}_3$ thin films*. Journal of Applied Physics, 2010. **108**(11): p. 113906.
206. Lu, H., et al., *Electric modulation of magnetization at the $\text{BaTiO}_3/\text{La}_{0.67}\text{Sr}_{0.33}\text{MnO}_3$ interfaces*. Applied Physics Letters, 2012. **100**(23): p. 232904.
207. Vaz, C.A.F., et al., *Origin of the Magnetoelectric Coupling Effect in $\text{PbZr}_{0.2}\text{Ti}_{0.8}\text{O}_3/\text{La}_{0.8}\text{Sr}_{0.2}\text{MnO}_3$ Multiferroic Heterostructures*. Physical Review Letters, 2010. **104**(12): p. 127202.
208. Meyer, T.L., et al., *Enhancing interfacial magnetization with a ferroelectric*. Physical Review B, 2016. **94**(17): p. 174432.
209. Zhuravlev, M.Y., S. Maekawa, and E.Y. Tsymbal, *Effect of spin-dependent screening on tunneling electroresistance and tunneling magnetoresistance in multiferroic tunnel junctions*. Physical Review B, 2010. **81**(10): p. 104419.
210. Gajek, M., et al., *Tunnel junctions with multiferroic barriers*. Nature Materials, 2007. **6**: p. 296.
211. Hambe, M., et al., *Crossing an Interface: Ferroelectric Control of Tunnel Currents in Magnetic Complex Oxide Heterostructures*. Advanced Functional Materials, 2010. **20**(15): p. 2436-2441.
212. Yin, Y.-W., et al., *Multiferroic tunnel junctions*. Frontiers of Physics, 2012. **7**(4): p. 380-385.

213. Yin, Y.W., et al., *Coexistence of tunneling magnetoresistance and electroresistance at room temperature in La_{0.7}Sr_{0.3}MnO₃/(Ba, Sr)TiO₃/La_{0.7}Sr_{0.3}MnO₃ multiferroic tunnel junctions*. Journal of Applied Physics, 2011. **109**(7): p. 07D915.
214. Yin, Y.W., et al., *Multiferroic tunnel junctions and ferroelectric control of magnetic state at interface (invited)*. Journal of Applied Physics, 2015. **117**(17): p. 172601.
215. Liu, Y.K., et al., *Coexistence of four resistance states and exchange bias in La_{0.6}Sr_{0.4}MnO₃/BiFeO₃/La_{0.6}Sr_{0.4}MnO₃ multiferroic tunnel junction*. Applied Physics Letters, 2014. **104**(4): p. 043507.
216. Mao, H.J., et al., *Interface-modification-enhanced tunnel electroresistance in multiferroic tunnel junctions*. Journal of Applied Physics, 2014. **116**(5): p. 053703.
217. Quindeau, A., et al., *Four-state ferroelectric spin-valve*. Scientific Reports, 2015. **5**: p. 9749.
218. Yau, H.M., et al., *Low-field Switching Four-state Nonvolatile Memory Based on Multiferroic Tunnel Junctions*. Scientific Reports, 2015. **5**: p. 12826.
219. Huang, W., et al., *Interfacial Ion Intermixing Effect on Four-Resistance States in La_{0.7}Sr_{0.3}MnO₃/BaTiO₃/La_{0.7}Sr_{0.3}MnO₃ Multiferroic Tunnel Junctions*. ACS Applied Materials & Interfaces, 2016. **8**(16): p. 10422-10429.
220. Yin, Y.-W., et al., *Octonary Resistance States in La_{0.7}Sr_{0.3}MnO₃/BaTiO₃/La_{0.7}Sr_{0.3}MnO₃ Multiferroic Tunnel Junctions*. Advanced Electronic Materials, 2015. **1**(11): p. 1500183-n/a.
221. Ruan, J., et al., *Improved memory functions in multiferroic tunnel junctions with a dielectric/ferroelectric composite barrier*. Applied Physics Letters, 2015. **107**(23): p. 232902.
222. Ruan, J., et al., *Four-state non-volatile memory in a multiferroic spin filter tunnel junction*. Applied Physics Letters, 2016. **109**(25): p. 252903.
223. Cabero, M., et al., *Atomic resolution studies of La_{0.7}Sr_{0.3}MnO₃/BaTiO₃ multiferroic tunnel junctions*, in *European Microscopy Congress 2016: Proceedings*. 2016, Wiley-VCH Verlag GmbH & Co. KGaA.
224. Soni, R., et al., *Polarity-tunable spin transport in all-oxide multiferroic tunnel junctions*. Nanoscale, 2016. **8**(20): p. 10799-10805.
225. Liang, S., et al., *Ferroelectric Control of Organic/Ferromagnetic Spinterface*. Advanced Materials, 2016. **28**(46): p. 10204-10210.
226. Sanchez-Santolino, G., et al., *Resonant electron tunnelling assisted by charged domain walls in multiferroic tunnel junctions*. Nature Nanotechnology, 2017. **12**: p. 655.

227. Singh, K. and D. Kaur, *Four logic states of tunneling magnetoelectroresistance in ferromagnetic shape memory alloy based multiferroic tunnel junctions*. Applied Physics Letters, 2017. **111**(2): p. 022902.
228. Barman, R. and D. Kaur, *Influence of barrier thickness on Ni_{50.3}Mn_{36.9}Sb_{12.8}/BiFeO₃/Ni_{50.3}Mn_{36.9}Sb_{12.8} multiferroic tunnel junctions*. Ceramics International, 2017. **43**(17): p. 15654-15658.
229. Meservey, R. and P.M. Tedrow, *Spin Polarized Electron Tunneling*. 1994: North-Holland.
230. Tedrow, P.M. and R. Meservey, *Spin Polarization of Electrons Tunneling from Films of Fe, Co, Ni, and Gd*. Physical Review B, 1973. **7**(1): p. 318-326.
231. Meservey, R., P.M. Tedrow, and P. Fulde, *Magnetic Field Splitting of the Quasiparticle States in Superconducting Aluminum Films*. Physical Review Letters, 1970. **25**(18): p. 1270-1272.
232. Tedrow, P.M. and R. Meservey, *Spin-Dependent Tunneling into Ferromagnetic Nickel*. Physical Review Letters, 1971. **26**(4): p. 192-195.
233. Slonczewski, J.C., *Conductance and exchange coupling of two ferromagnets separated by a tunneling barrier*. Physical Review B, 1989. **39**(10): p. 6995-7002.
234. MacLaren, J.M., X.G. Zhang, and W.H. Butler, *Validity of the Julliere model of spin-dependent tunneling*. Physical Review B, 1997. **56**(18): p. 11827-11832.
235. Yin, Y. and Q. Li, *A review on all-perovskite multiferroic tunnel junctions*. Journal of Materiomics, 2017. **3**(4): p. 245-254.
236. Butler, W.H., et al., *Spin-dependent tunneling conductance of Fe/MgO/Fe sandwiches*. Physical Review B, 2001. **63**(5): p. 054416.
237. Fert, A. and I.A. Campbell, *Two-Current Conduction in Nickel*. Physical Review Letters, 1968. **21**(16): p. 1190-1192.
238. Graz, T. *Electron density of states for bcc iron*. 2016 [cited 2018 5 Mar]; Available from: <http://lampx.tugraz.at/~hadley/ss1/materials/dos/iron.html>.
239. Himpsel, F.J., et al., *Magnetic nanostructures*. Advances in Physics, 1998. **47**(4): p. 511-597.
240. Zhang, S., et al., *Quenching of magnetoresistance by hot electrons in magnetic tunnel junctions*. Physical Review Letters, 1997. **79**(19): p. 3744.
241. Davis, A.H. and J.M. MacLaren, *Spin dependent tunneling at finite bias*. Journal of Applied Physics, 2000. **87**(9): p. 5224-5226.
242. De Teresa, J.M., et al., *Role of Metal-Oxide Interface in Determining the Spin Polarization of Magnetic Tunnel Junctions*. Science, 1999. **286**(5439): p. 507-509.

243. Bratkovsky, A., *Spin Tunneling in Conducting Oxides in MRS Fall Meeting*. 1997: Boston.
244. Yuasa, S., et al., *Giant room-temperature magnetoresistance in single-crystal Fe/MgO/Fe magnetic tunnel junctions*. Nature Materials, 2004. **3**: p. 868.
245. Zhang, J. and R.M. White, *Voltage dependence of magnetoresistance in spin dependent tunneling junctions*. Journal of Applied Physics, 1998. **83**(11): p. 6512-6514.
246. Valenzuela, S.O., et al., *Spin polarized tunneling at finite bias*. Physical review letters, 2005. **94**(19): p. 196601.
247. Duan, C.-G., S.S. Jaswal, and E.Y. Tsymbal, *Predicted magnetoelectric effect in Fe/BaTiO₃ multilayers: ferroelectric control of magnetism*. Physical Review Letters, 2006. **97**(4): p. 047201.
248. Petraru, A., et al., *Wedgelike ultrathin epitaxial BaTiO₃ films for studies of scaling effects in ferroelectrics*. Applied Physics Letters, 2008. **93**(7): p. 072902.